UNIVERSITAT POLITÈCNICA DE VALÈNCIA

INSTITUTO DE TECNOLOGÍA QUÍMICA

(UPV-CSIC)

Characterization of metallic species on porous materials by *in situ* XAS

DOCTORAL THESIS

Presented by

Christian Wittee Lopes

Supervised by:

Prof. Fernando Rey García

Dr. Giovanni Agostini

Valencia, July 2018

“Não podemo se entregá pros home, de jeito nenhum…”

(Leopoldo Rassier)

Abstract

The aim of this thesis is to study the clustering and growth of metallic species either confined or supported in porous materials by *in situ* X-ray absorption spectroscopy. To accomplish this task, palladium and silver species were introduced into porous materials (γ-alumina, activated carbon and zeolites) by wetness impregnation and ion-exchange methods, respectively. Then, the clustering of these metallic species was controlled by activation treatments in different atmospheres (inert, oxidative and reductive) and followed by XAS in a comprehensive way.

The principal goal of current work is to demonstrate that both XANES and EXAFS can provide valuable and, at certain point, innovative information during tuning of metallic species (in terms of type and size). Taking advantage of unusual analysis procedures, such as cumulant approach, fitting of imaginary part of Fourier transform and others, it is possible to obtain refined information about the investigated systems.

In the introduction section, a compilation of studies in which XAS was used as important technique to characterize metallic species in porous materials is provided. Conscious that people can use such introduction as a basis for more complex studies in the future, the discussion has been tentatively directed toward this goal.

The chapter 4 is focused on the study of the influence of palladium precursors and the nature of support on the resultant nanoparticles. The whole activation process, i.e. the transformation precursor → nanoparticle, was followed *in situ* by XAS. The analysis pathway was composed by the starting point (as-impregnated), calcination in O_2 flow and posterior reduction with H_2. The consequence of using distinct metal precursors and supports were discussed in terms of average coordination number obtained from EXAFS data analysis, which was co-supported by laboratory characterization techniques.

The chapter 5 is dedicated to the study of silver clustering during and after activation treatments using Ag-containing small-pore zeolites as precursors and nanocontainers. The influence of framework structure and chemical composition of Ag-based materials on formed Ag species at different clustering and metal redispersion conditions (calcination using distinct atmospheres, reduction in H_2, redispersion in O_2) were studied using either *in situ* or *ex situ* characterization methods. After, the catalytic consequences of tuned Ag-containing zeolites in SCO-NH_3 are discussed. In this section, the combination of *in situ* XAS with several laboratory techniques proved to be pivotal to have a full picture of the investigated system.

Finally, a list of projects developed in parallel to this thesis is provided at the end of this document.

Resumen

El objetivo de esta tesis es estudiar la agrupación y el crecimiento de especies metálicas confinadas o soportadas en materiales porosos mediante espectroscopia de absorción de rayos X *in situ*. Para lograrlo, las especies de paladio y plata se han introducido en materiales porosos (γ-alúmina, carbón activo y zeolitas) mediante impregnación vía húmeda y métodos de intercambio iónico, respectivamente. Luego, el agrupamiento de estas especies metálicas se ha controlado mediante tratamientos de activación en diferentes atmósferas (inerte, oxidativa y reductiva) y seguido por XAS de manera detallada.

El objetivo principal del trabajo actual es demostrar que tanto XANES como EXAFS pueden proporcionar información valiosa y, en cierto punto, innovadora durante el control de especies metálicas (en términos de tipo y tamaño de las especies). Aprovechando los procedimientos de análisis inusuales, como el análisis de los cumulantes, el ajuste de la parte imaginaria de la transformada de Fourier y otros, es posible obtener información refinada sobre los sistemas investigados.

En la sección de introducción, se proporciona una compilación de estudios en los que se ha utilizado XAS como técnica importante para caracterizar especies metálicas en materiales porosos. Conscientes de que las personas pueden usar dicha introducción como base para estudios más complejos en el

futuro, la discusión se ha dirigido tentativamente hacia este objetivo.

El capítulo 4 se centra en el estudio de la influencia de los precursores de paladio y la naturaleza del soporte en las nanopartículas resultantes. El proceso de activación completo, es decir, la transformación precursor → nanopartícula, ha sido seguido por XAS *in situ*. El análisis estuvo compuesto por el punto de partida (material impregnado), calcinación en flujo de O_2 y reducción posterior con H_2. La consecuencia del uso de diferentes precursores metálicos y soportes se ha discutido en términos del número de coordinación promedio obtenido a partir del análisis de datos de EXAFS, que fue respaldado por técnicas de caracterización de laboratorio.

El capítulo 5 está dedicado al estudio de la agrupación de plata durante y después de los tratamientos de activación utilizando zeolitas de poro pequeño intercambiadas con plata como precursores y nanocontenedores. Se ha estudiado la influencia de la estructura y la composición química de los materiales basados en plata sobre las especies metálicas formadas en diferentes condiciones de agrupamiento y redispersión del metal (calcinación usando atmósferas distintas, reducción en H_2, redispersión en O_2) utilizando métodos de caracterización *in situ* o *ex situ*. Después, se discuten las consecuencias catalíticas de las zeolitas que contienen Ag en la reacción de SCO-NH_3. En esta sección, la combinación de XAS

in situ con varias técnicas de laboratorio ha demostrado ser fundamental para un completo entendimiento del trabajo.

Finalmente, una lista de proyectos desarrollados en paralelo a esta tesis se proporciona al final de este documento.

Resum

L'objectiu d'aquesta tesi és estudiar l'agrupació i el creixement d'espècies metàl·liques confinades o suportades en materials porosos mitjançant espectroscòpia d'absorció de raigs X *in situ*. Per a això, les espècies de pal·ladi i plata s'han introduït en materials porosos (γ-alúmina, carbó activat i zeolites) per mitjà de la impregnació via humida i mètodes d'intercanvi iònic, respectivament. Una vegada preparats els materials, l'agrupament de les espècies metàl·liques s'ha controlat fent ús de tractaments d'activació en diferents atmosferes (inert, oxidant i reductora) s'ha estudiat exhaustivament per XAS.

L'objectiu principal del treball és demostrar que tant el XANES com l'EXAFS proporcionen informació rellevant i, en certa manera, innovadora per al control d'espècies metàl·liques (en termes de tipus i grandària d'aquestes espècies). Fent ús de procediments de tractament de dades no molt habituals com l'anàlisi de *cumulants*, l'ajust de la part imaginària de la transformada de Fourier i altres, és possible obtenir informació detallada sobre els sistemes estudiats.

En l'apartat de la introducció, es proporciona una recopilació d'estudis en els quals s'ha utilitzat XAS com a tècnica principal per a caracteritzar les anomenades espècies metàl·liques en materials porosos. Aquesta introducció ha estat redactada per a que puga servir com a punt de partida per a

futurs estudis que requereixen la utilització de XAS per a la caracterització de les espècies metàl·liques presents en els catalitzadors.

El capítol 4 es centra en l'estudi de la influència dels precursors de pal·ladi i la naturalesa del suport front a les nanopartícules resultants. El procés d'activació, és a dir, la transformació precursor → nanopartícula, ha sigut estudiat per XAS *in situ*. L'anàlisi per XAS va comprendre els següents passos: punt de partida (material impregnat), calcinació en flux d'O_2 i reducció posterior amb H_2. La utilització de diferents precursors i suports metàl·lics ha permès dur a terme una discussió, referent al nombre de coordinació mitjà obtingut a partir de l'anàlisi de dades de la zona EXAFS, que ha estat recolzat per altres tècniques de caracterització.

El capítol 5 s'ha dedicat a l'estudi de l'agrupació de plata intercanviada en els catalitzadors durant i després dels tractaments d'activació. S'han utilitzat zeolites de porus xicotet, com la CHA i RHO, intercanviades amb plata. L'estudi de la influència de l'estructura zeolítica i la composició química dels materials enfront dels diferents tractaments d'activació (calcinació utilitzant diferents atmosferes, reducció en presència d'H_2, re-dispersió en atmosfera d'O_2) es va realitzar fent ús de mètodes de caracterització *in situ* o *ex situ*. A continuació, es discuteix la influència d'aquestes espècies metàl·liques formades, utilitzant els diferents mètodes d'activació, per a la reacció d'SCO-NH_3. En aquest sentit, s'ha demostrat que la

combinació de XAS *in situ* amb diverses tècniques habituals de laboratori és fonamental per al desenvolupament d'aquest treball. Finalment, es presenta una llista de projectes, en els quals també s'ha treballat paral·lelament, on s'ha utilitzat XAS com a tècnica de caracterització.

Acronyms

4MR – Four Member Rings

BET – Brunauer-Emmett-Teller

CN – Coordination Number

D6R – Double Six Rings

D8R – Double Eight Rings

DFT – Density Functional Theory

DR – Diffuse Reflectance

DRIFTS – Diffuse Reflectance Infrared Fourier Transform Spectroscopy

EDS – Energy Dispersive X-Ray Spectroscopy

EXAFS – Extended X-ray Absorption Fine Structure

fcc – Face Centered Cubic crystal structure

FEFF – effective curved wave scattering amplitude in the modern EXAFS equation

FESEM – Field Emission Scanning Electron Microscopy

FTS – Fischer-Tropsch Synthesis

GAC – Granular Activated Carbon

GHSV – Gas Hourly Space Velocity

hcp – Hexagonal Close Packed crystal structure

HOMO – Highest Occupied Molecular Orbital

ICP-OES – Inductively Coupled Plasma Atomic Emission Spectroscopy

Imm – Imaginary part of Fourier transform

IZA – International Zeolite Association

LDH – Layered Double Hydroxides

LUMO – Lowest Unoccupied Molecular Orbital

MAS NMR – Magic Angle Spinning Nuclear Magnetic Resonance

MDA – Methane Dehydroaromatization

MOF – Metal Organic Frameworks

mpg – Mesoporous Graphitic carbon nitride

MSR – Methanol Steam Reforming

MTO – Methanol to Olefins

NP – Nanoparticle

OSDA – Organic Structure-Directing Agent

PDF – Pair Distribution Function

PEM – Proton-exchange Membrane fuel cell

SBU – Secondary Building Unit

SCO – Selective Catalytic Oxidation

SCR – Selective Catalytic Reduction

STEM – Scanning Transmission Electron Microscopy

TEM – Transmission Electron Microscopy

TGA – Thermogravimetric Analysis

TMA – Tetramethylammonium

TPA – Tetrapropylammonium

TPV – Total Pore Volume

UV–Vis – Ultraviolet–Visible

WoS – Web of Science

XANES – X-ray Absorption Near Edge Structure

XAS – X-ray Absorption Spectroscopy

XPS – X-ray Photoemission Spectroscopy

XRD – X-ray Diffraction

ΔE_0 – correction to the energy origin or threshold energy shift

σ^2 – Debye-Waller factor or mean square relative displacement (MSRD or DWF)

|FT| – Modulus of Fourier Transform

Acknowledgements

I would like to start saying that it is not fair enough to me to write this part only in English since it is not my mother language so I am afraid that my feelings would not be well expressed. For this reason, I am going to write it in the three languages that have brought me here (in chronological order).

Primeiramente eu preciso agradecer a minha família, mãe, vó e meus dois irmãos, porque sem vocês e todo o incentivo que me deram desde o começo disso tudo, esse trabalho e os outros que o antecederam não seriam possíveis. Em segundo lugar eu quero agradecer a pessoa que tem sido a mais importante na minha vida desde alguns anos atrás, a qual compartilha o mesmo sonho, as mesmas dificuldades e tudo que envolve estar longe de "casa". Fran, obrigado por tudo, por ser meu porto seguro e me tornar uma pessoa melhor a cada dia que passa.

Também preciso agradecer as duas pessoas que acreditaram em mim profissionalmente desde o começo, me lapidaram e fizeram minha vinda pra Espanha possível: Fábio e Sibele. Só me resta agradecer o tempo que vocês dedicaram para que eu crescesse como pessoa e como profissional.

Aos meus amigos de infância e de profissão, especialmente aqueles que estiveram (ou que conheci) na Espanha, os quais fizeram com que a saudade de casa fosse atenuada pelos momentos compartilhados.

Pasando al próximo idioma, me gustaría agradecer a mi director de tesis, Prof. Fernando Rey por haberme aceptado, por enseñarme que calidad es mejor que cantidad y haberme dado la oportunidad de hacer la tesis en un tema tan singular. Muchas gracias por las horas de conversación (que han sido muchas), en las cuales hablamos no solo de ciencia pero también de cosas cotidianas. A todos los investigadores que han colaborado en el desarrollo de este trabajo pero especialmente a la Dra. Teresa Blasco, el Prof. Eduardo Palomares y el Prof. Agustín Martínez por haber sido siempre muy cercanos y por la colaboración en mi formación como investigador. A mis compañeros Ximo, Edi, Nuria y José Luis por la amistad y principalmente por aguantar conmigo las horas de sincrotrón. Los momentos de risa que hemos tenido han transformado dichas horas en recuerdos que nunca olvidaré. Finalmente, me gustaría agradecer a la persona que tuvo un papel clave en mi formación y consecuente desarrollo de esta tesis. Cris Alonso, muchas gracias por haber sido mi tutora, consejera, colega y ahora una amiga muy especial. En general, quiero agradecer a todas las personas del ITQ (desde técnicos a personal de administración) que pueda haber contribuido un poquito en el desarrollo de esta tesis doctoral.

Finally, I would like to acknowledge my co-director, Dr. Giovanni Agostini. Sei molto grande. Thanks for being such a kind person every time I needed your help and for being always available to answer my questions and solve my problems. You

not only taught me how to analyze XAS data, but taught me how to do research in a consistent and transparent way. Thanks to you I have met Giorgia, who made my time in Germany much less difficult and also turned me into Italian for a short period of my life.

I also need to thank Whisky, my faithful (sometimes not too much) friend during my time in (cold) Rostock at the end of this thesis. At this moment, I am reconsidering my opinion about cats.

Last but not least, I would like to thank the person who made this thesis possible to be written in the current language, my former English teacher and now friend, Andrew Hewitt.

ALBA and ESRF synchrotrons are acknowledged for beamline allocation and staff assistance during XAS experiments.

CAPES (Program Science without Borders) is acknowledged for the doctoral scholarship.

Index

Chapter 1

Introduction

1.1 Metallic species in porous materials probed by XAS

From the 70's to the present years, the availability of well-developed instrumentation on synchrotron light sources allowed the characterization of diverse types of samples by different advanced techniques in experiments requiring high X-ray flux in continuous energy interval. Among the employed characterization methods, X-ray absorption spectroscopy (XAS) has become a powerful technique in all the fields of materials science and, particularly, in catalysis.[1] The reason relies on its atomic selectivity which enables the characterization of a specific element within complex matrices composed by several chemical elements (e.g. perovskites and clays). XAS is highly sensible to low element concentration as well, being able to measure the absorption edge of elements containing considerable small amounts (hundreds of ppm) respect to the total mass of sample. Moreover, it is also important to underline that XAS does not require local ordering around probed element, which is a tremendous advantage respect to other techniques. All these advantages coupled with the possibility to control the sample environment attracted the attention of research groups in the area of catalysis.

The catalytic community has gained space within the synchrotrons over time which is mainly related to the improvement or development of new and sophisticated experimental setup for *in situ* or *operando* experiments.[2] In the last years great improvements have been made regarding

coupling XAS with other techniques within beamlines all over the world. Some examples that may be cited are the combination of XAS with XRD/Raman[3-4] and with DRIFTS.[5] A small example among several possibilities is following the modifications on the support by XRD while XAS evaluates the changes in the metallic species upon catalytic reaction or activation processes.

Notwithstanding, the increasing of beamlines displaying time-resolved XAS[6] (from Energy dispersive or Quick-EXAFS experiments) enabled the designing of complex experiments focusing on unrevealing reaction mechanisms in time-dependent reactions. It has also forced the researchers to develop more sophisticated methods for data analysis and also those for treating large amounts of data.[7-8]

In order to underline the importance of XAS to catalysis and to demonstrate the strong relationship between them, **Figure 1.1** shows the huge number of papers available in literature searching the following keywords on search engines like Scopus or ISI Web of Science (WoS): "*in situ* XAS" and "EXAFS and Catalyst".

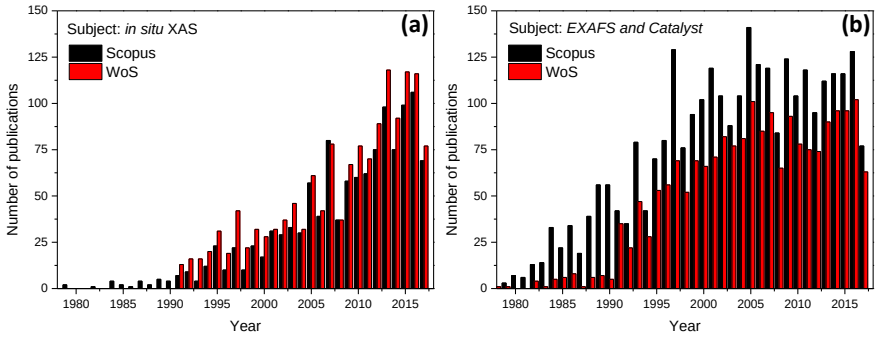

Figure 1.1 Number of publications related to *in situ* XAS (a) and EXAFS and Catalyst (b) over the years.

The main focus of this doctoral thesis is the application of XAS for the characterization of metallic systems, especially focused on the area of catalysis. A compilation of interesting works was done with the aim of highlighting the distinct information that can be extracted in several systems (i.e. metal nanoparticles, metal-substituted zeolites, metal-exchanged zeolites) by different approaches without intention to be complete. The topics can be divided into two groups: (i) relevant topics in the context of this doctoral thesis and (ii) topics related to the relevance of XAS to these subjects. In the first group (i) we can include the *methods for nanoparticle size estimation from EXAFS*, the *reversible interconversion from nanoparticles to single atoms* and also *metal-exchanged zeolites*, with some of them interconnected during the thesis. The second group (ii) includes examples where XAS is really required nowadays due to its element-sensitive character (*bimetallic nanoparticles*) or due to its ability to handle data from non-

ordered systems in which characterization by other techniques is more complex (*single atoms*). A briefly description about each system is also tentatively included along the text.

1.1.1 Supported metal nanoparticles

With the advent of nanotechnology age, the increasing in manipulation and better understanding of matter at nanoscale range is essential to guarantee prosper technological progress.[9] Nanoparticles are the core of nanotechnology and are generally described as particles with at least one dimension (length, width or thickness) comprised in the nanoscale range (1 to 100 nm).[9] By manipulating the size of matter (active sites, pore and particle sizes) distinct properties can be achieved, which may be different for single atoms and subnanometric clusters in comparison with metal nanoparticles, which in turn are expected to be unlike in those bulk counterparts. For example, constant physical properties are expected in the bulk, regardless of its size, while for nanoparticles, size-dependent properties are often observed.

The dependence of dispersion and total number of atoms in metal nanoparticles as a function of particle size is reported in **Figure 1.2**. The plot shows only the range of sizes relevant to XAS (up to 100 Å) and takes into account a cuboctahedral shape for Pd nanoparticles with *fcc* structure. With increasing the nanoparticle size, the number of surface atoms (in terraces, edges and/or corners - depicted in right side of **Figure 1.2**)

respect to the total atoms in a nanoparticle is decreased, which is translated into lower values of metallic dispersion. Moreover, dispersion values drops abruptly from 10 to 60 Å whereas above that value the dispersion is not significantly affected, varying only 7% for particle size between 60 to 100 Å (for further details on the dispersion relationships the reader is referred to reference literature[10]).

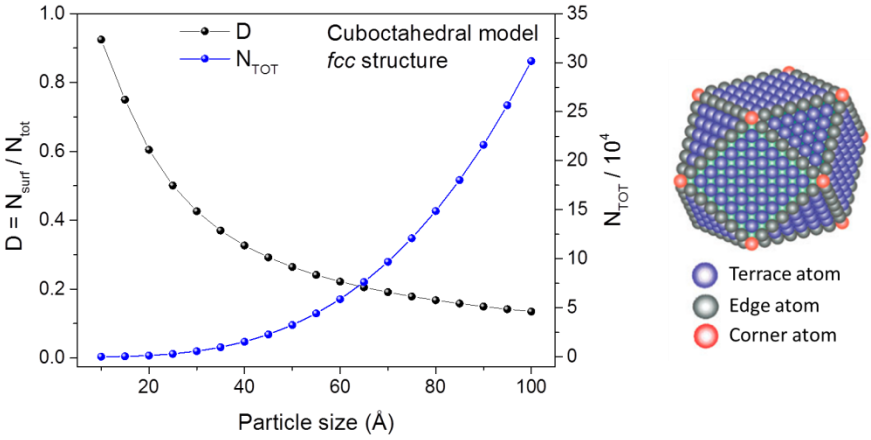

Figure 1.2. Total number of atoms (N_{tot}) and dispersion (D = N_{surf}/N_{tot}) as a function of the particle size from the cuboctahedral geometrical model Pd nanoparticles[10-11] (left) and examples of different types of surface atoms in metal nanoparticles (right). (Adapted from reference[12])

Notwithstanding, when the particle size is too small, where all atoms or most of them are on the surface, the energy contribution due to facets (terraces), edges and corners (right side of **Figure 1.2**) is not negligible[13] and consequently the particle is not at a thermodynamic stable state. In order to

minimize this problem, much effort have been done using organic ligands, capping agents or metal salts in order to avoid particle growth. The problem of using this approach is that sometimes nanoparticles may suffer from poisoning, instability of organic phases at high temperatures, resulting in deactivation and/or loss of catalytic activity. In addition, the recovery from the reaction media to successive uses and regeneration is a quite difficult task. To overcome this issue, the combination of nanoparticle and porous materials is very attractive and can be of interest not only in catalysis but also from a multidisciplinary point of view.[9] Finally, it is important to underline that the relative ratio of atoms in facets (terraces), edges and vertices change with cluster size, which tune their properties.

Metal nanoparticles can be supported on different types of materials, such as metallic oxides (mainly SiO_2,[14-15] Al_2O_3,[16-18] CeO_2[19] and TiO_2[20-21]), LDH-derived oxides,[22] carbons,[23-26] polymers,[27-28] zeolites,[29-30] MOFs,[31-32] ordered mesoporous materials,[33-34] clays,[35] among others. Apart from nanoparticle stabilization, the support can help in the tuning of nanoparticles properties. For example, nanoparticle growing can be avoided by restriction of support pore size,[33] distinct metal reduction pathways and blockage of determined surface atoms can be observed due to strong metal-support interactions,[20-21, 36] including other effects. Moreover, using the same support but just changing the metal impregnation approach (by choosing different metal precursors or methods)[37-38] or activation

parameters (calcination and/or reduction processes)[37, 39] could result in a metal-support system completely distinct.

Among the variety of techniques employed to characterize metal nanoparticles (spectroscopic,[1] surface-sensitive,[40] imaging), the X-ray absorption spectroscopy is certainly one of the most powerful tools due to its element-selective character, short-range and chemical sensitivities. The information obtainable from XAS (both XANES and EXAFS regions) is broad but in the case of nanoparticles the most important and targeted parameter in literature is the coordination number[41] (specially for drawing conclusions about nanoparticle structure), along with metal-metal distance and Debye-Waller factor (not necessarily in that order) which is directly related to thermal and static disorder of the metallic system (further information can be obtained in reference[41]). However, in some cases, the three parameters (CN, distance and disorder) can separately provide information about nanoparticle size because they are completely related due to quantum size effects already known for nanosystems (which will be observed in some cases along this work – see **Chapter 4**). In principle, with decreasing the size of NP (and consequently the coordination number), the metal bond length is contracted and more disordered system is expected.[42] In addition, XAS is able to distinguish different neighbors/ligands bonded to the absorber atom, which is very important when phase transition between one component to

another takes place, like decomposition of complexes into oxides (see **Chapter 4**).

In comparison with other techniques, such as TEM and XRD, XAS provide unique and valuable information. In general characterization of nanosystems comprising particles sizes ≤5 nm is quite challenging either because the peaks are too broad (or even absent) in XRD due to lack of long range order or also due to the weak contrast between the metallic species and the support (e.g. Cu/CeO_2, Co/TiO_2), which makes their distinction by TEM very difficult. These factors make XAS a very important technique, since the support does not interfere due to the element-sensitive character of the analysis; no issues about statistic, and the spectra can be acquired in harsh conditions (*in situ*/*operando*) what is currently impossible to be performed through standard TEM instrument.

The process of obtaining particle sizes begins with a hypothesis about particle morphology (e.g. cuboctahedral, icosahedral or truncated cuboctahedral) and first shell average coordination number value from EXAFS fitting. Then, the average particle size and other parameters (e.g. dispersion and total metallic atoms in the nanoparticle) can be estimated by applying some equations[10] considering determined crystalline topology. However, some considerations should be addressed, such as the presence of significantly larger nanoparticles which can affect the EXAFS signal through constructive scattering effects. This can mask the real average coordination number,

which would result in erroneous analysis of the data, leading to wrong conclusions about the system. In literature some authors have modeled nanoparticles with different shapes and sizes and represented *particle size vs average coordination number* of nanoparticles, highlighting the size regime feasible to be obtained by EXAFS (between 2-4 nm), like those represented by Nashner[43] (**Figure 1.3a**) and de Graaf[44] (**Figure 1.3b**). In both cases, *fcc* structure and spherical shapes were considered in advance. It can be noticed that as coordination number increases, the particle size is higher, with curved profiles. Similar plots based on modelling and calculations considering other particles shape, structure and particle size distribution can be found elsewhere.[11, 45]

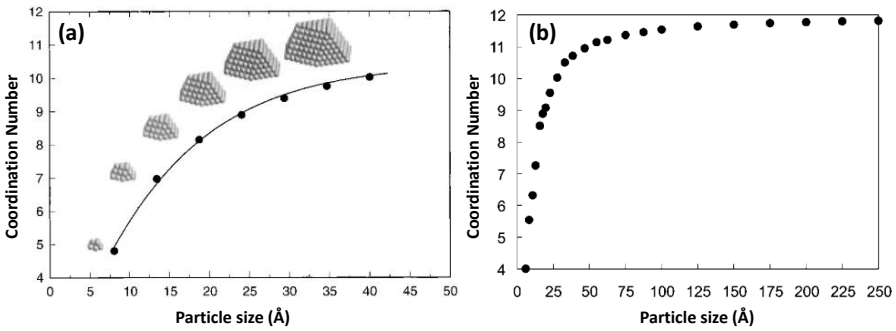

Figure 1.3. Correlation between average first shell coordination number and diameter of nanoparticle considering (a) hemispherical and (b) spherical *fcc* metal nanoparticles (Adapted from references[43-44]).

Another example for metallic particle size estimation is based on metal-metal distances rather than average coordination

number. Taking advantage of palladium hydrides formation during exposure of Pd nanoparticles to H_2 atmosphere at low temperatures (<80 ºC), Wang et al.[46] developed a method for the determination of nanoparticle size by measuring the Pd metal-metal bond length. By measuring the EXAFS spectra of a 2 nm Pd-based sample at different steps of thermal treatments in H_2 and He (in conditions of stability and instability of PdH_x) the authors were able to determine the size of nanoparticles. To do that, a correlation between H/Pd ratio obtained from the Pd-Pd distance and the cluster model size was made.

The process of nanoparticle size estimation from EXAFS has been extensively used through literature but in many cases the lack of information about real particle morphology can lead to wrong conclusions, as already commented. One fact that must be taken into account when using this method is the average metallic size. At determined size regimes (subnanometric range), it is difficult to attribute the cluster shape and at the same time most equations are based on crystalline phases, so the determination of metallic average size is not straightforward and should be carefully handled. One should pay attention also to the higher shells of |FT| which were identified as extremely important in terms of nanoparticle shape.[47]

Let's now focus on the group where the particle size regimen is really small (less than or around 1 nm). In last years an effort has been made regarding the preparation and characterization of supported subnanometric metallic clusters

(either mono or bimetallic) and single atom-claimed systems due to their outstanding performance in catalytic reactions and noble metal expend minimization.[48] Despite the extensive characterization by powerful techniques, the XAS investigation is relatively poor and a consistent or comprehensive approach to study subnanometric systems is missing until now. Several contributions reporting metal single atoms on porous materials are available.[49-60] The general trend reported is that no metal-metal contributions are found in most systems, only the presence of metal-support interactions or metal-ligands are stated. Also, usually the metal single atoms are electronic rich and the white line in XANES is more intense respect to those bulk counterparts and the oscillations beyond the edge are damped due to quantum size effects.

One of most interesting examples comes from Perez-Ramirez's group who used EXAFS to characterize Pd single-sites anchored into the cavities of mesoporous polymeric graphitic carbon nitride.[26] The catalyst named [Pd]mpg-C_3N_4 displayed 100 % of metal dispersion which was further supported by other techniques (CO chemisorption, TEM, XPS). From the XAS point of view, despite the lack of explanation about XANES and $\chi(k)$, the authors claimed that neither Pd-Pd contribution was observed nor peaks at a distance greater than 2 Å, contrasting with conventional nanoparticle-based systems. This approach was further performed for Pt single atoms supported on g-C_3N_4[61] and similar results were obtained, where

no Pt-Pt contributions were observed. However, in this case, the discussion was less extensive than the first example.[26] Simulating phase and amplitude of Pt-C/N by FEFF code the authors revealed that platinum atoms were dispersed on the top of five-membered rings of C_3N_4 network.

Yang et al.[62] studied Pt/TiN for selective electrochemical reactions and XAS was used for Pt electronic and structural characterization. Despite the lack of comparison with standards and inconsistencies on Pt-Pt distances for samples with variable Pt loading on EXAFS data analysis, the obtained coordination number for single atom sample was 0.58. However, since the catalysts were mildly reduced (100 ºC in H_2 flow), rests of Cl-based precursor with N_{Pt-Cl} = 3.03 were also observed, which could be the explanation for such low N_{Pt-Pt}.

Atomically dispersed ionic platinum (Pt^{2+}) on ceria (CeO_2) catalyst for CO oxidation[63] was characterized by XAS before and after steam-treatment. In brief, the impregnated sample was submitted to thermal treatment at 800 ºC in air for 12 h and further steam-treated at 750 ºC for 9 h. The authors claimed that even after harsh conditions the Pt is present as Pt^{2+} atomically dispersed (by XANES interpretation) within CeO_2 and only Pt-O contributions are visible in |FT|, without presence of further Pt-Pt shells. Despite this, only qualitative evaluation of EXAFS is given and no extra information was provided by the authors.

Yin and co-workers[64] developed a new method to achieve highly loaded (4 wt.%) stable Co single atoms on nitrogen-doped carbons. By using a bimetallic Zn/Co metal-organic framework as precursor, Co is reduced by carbonization of organic part and Zn is evaporated away due to the high temperature (800 ºC), as demonstrated in **Figure 1.4**. The XANES indicated that Co valence state was between 0 and +1, according to white line intensity in comparison with standards of well-known structure and oxidation state. Moreover, Co-N coordination peak positioned at 1.41 Å was observed in the |FT| after MOF pyrolysis and no Co-Co bonds was identified, which pointed out to the formation of atomically dispersed system. The authors also postulated the Co coordination from obtained N_{Co-N}, being composed by Co-N_4 and Co-N_2, depending on pyrolysis temperature.

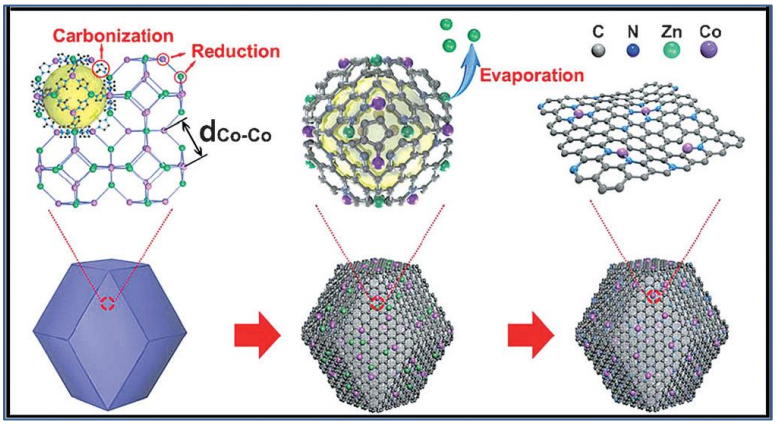

Figure 1.4. Formation of Co single atoms from MOF carbonization. (Adapted from reference[64])

The reversible transformation of nanoparticles into single atoms (especially within zeolites) has been also a hot topic.[65] By this approach, cycles of metal regeneration (oxidation and reduction treatments) can be performed to improve catalyst lifetime. However, it is important to highlight that in most cases redispersion of high metal amounts is challenging (for further information the reader is referred to **Chapter 5**). This behavior was already described for Ag-containing zeolites and titanosilicates, but with significant low metal amounts.[30, 66-68]

Recently, some interesting contributions came out such as the work of Moliner et al.[69] In brief, the authors performed XAS to follow reduction-reoxidation treatments on one-pot Pt-encapsulated high-silica CHA zeolite. Firstly, the initial state of Pt was investigated, being characterized to possess Pt-S paths (~4 S atoms) coming from thiol compound used for Pt stabilization during zeolite synthesis. This contribution was eliminated after calcination, giving rise to Pt-O distances from PtO_3 units (possibly oxygen atoms from CHA framework). After that, a reduction treatment in H_2 flow to form Pt nanoparticles was performed resulting into N_{Pt-Pt} of ~7 (Pt nanoparticles of ca. 1-1.5 nm) with subsequently reoxidation treatment in O_2 to redisperse the metal into single atoms (N_{Pt-O} = 3) within chabazite structure. The whole process can be easily visualized by both XANES and EXAFS since two clearly different species were shown (oxidized and reduced Pt), as observed in the moduli of Fourier-transform in **Figure 1.5a**.

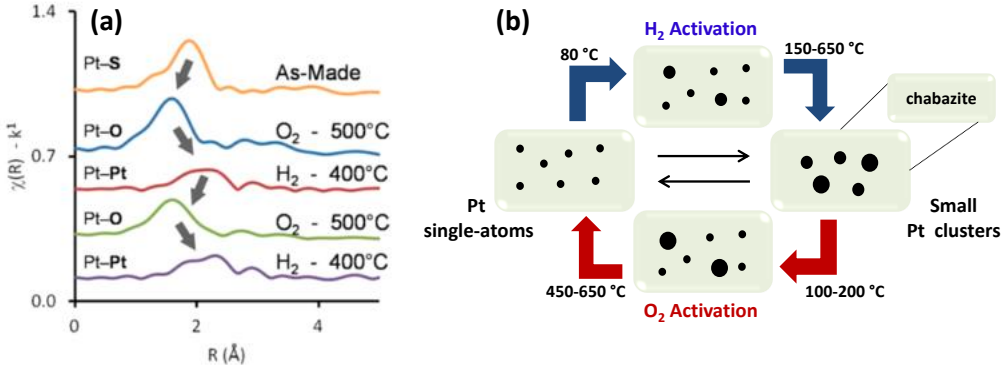

Figure 1.5. |FT| of Pt-containing CHA zeolite under different treatments (a) and general view of reversible transformation of Pt species inside zeolite (b). (Adapted from reference[69])

The authors claimed that it is possible to interconvert reversibly the Pt species several times at high temperatures probably due to the stabilization of metal species by zeolite framework. Also, the internal zeolitic voids can help in avoiding metal sintering. The XAS results were also supported by environmental STEM under reduction-reoxidation conditions. A picture exemplifying the reversible interconversion of metallic species can be seen in **Figure 1.5b**.

The last subject on characterization of nanoparticles by XAS is maybe the system which fully demonstrates the power of the technique and its element-sensitivity strength. Bimetallic nanoparticles are known for really impacting catalyst activity, selectivity and stability.[41] They can be synthesized in distinct shapes,[70-73] morphologies,[70] compositions and types of atomic and compositional ordering.[41, 72-76]

Coordination number in bimetallic nanoparticles measured by EXAFS can provide substantial information about structure. Considering nanoparticles composed of atoms A and atoms B, partial coordination numbers of N_{A-B}, N_{B-A}, N_{A-A} and N_{B-B} can be obtained by corefinement fit of both edges at the same time.[77] In turn, these parameters can be used to obtain intrinsic information about the system. Basically, three different ordering of bimetallic atoms can be expected in these systems: the so-called alloys (e.g. PtRu, PdAu), core-shell arrangement (typically expressed as core@shell) and segregated phases (separate metals not interacting with each other).

The recognition of each system can be done by according to the following findings:

- Segregated phases: when $N_{A-A} \neq N_{B-B}$ and the N_{A-B} is absent, the system is characterized to possesses two separated metallic nanoparticles, A and B.
- Core-shell: if $N_{A-M} < N_{B-M}$ the A-type atoms will segregate to the surface whilst B-type atoms to the core, since surface atoms are less coordinated than in the core. "M" is used when bimetallic nanoparticles with composing atoms of very similar atomic number are studied.
- Alloy: when $N_{A-A} = N_{B-B} = N_{A-B}$ is fulfilled, homogeneous alloying can be expected.

The three conditions are summarized in **Figure 1.6**.

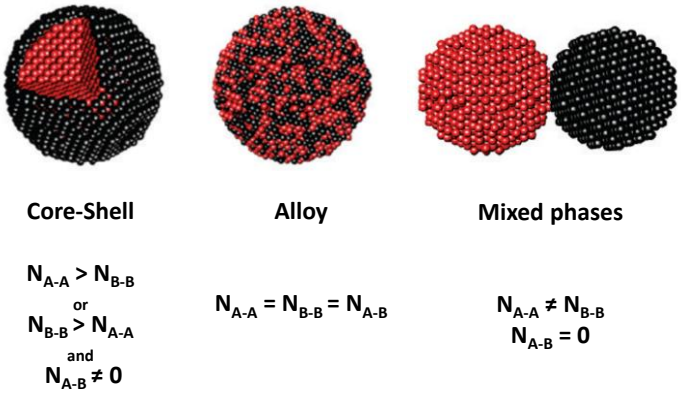

Figure 1.6. Different atomic ordering of bimetallic nanoparticles and consequences in terms of coordination numbers. (Adapted from references[78])

Once the partial coordination numbers are known, the total coordination number (N_{M-M}) can be calculated[79] and used to determine the size and shape of nanoparticles, as for monometallic systems.[41]

Hwang et al.[80] and Frenkel[79] developed methods for quantitatively determinate atomic distributions like the tendency to clustering preferentially to one or another atom type, i.e., the preference of A atoms to be close to other A atoms. For more detailed information the reader is referred to Frenkel's[41] review on bimetallic nanoparticles characterization by EXAFS.

The following examples are just a selection of many excellent works demonstrating the capability of XAS to handle bimetallic analysis and solving structures. Nashner et al.[43] studied Pt/Ru bimetallic nanoparticles by *in situ* XAS and were

able to follow the transformation of the starting structure of molecular bimetallic cluster $PtRu_5C(CO)_{16}$ toward Pt segregation to the core of the supported bimetallic nanoparticle $[PtRu_5]/C$. The authors used the extracted coordination number from multi-edge data fitting and a combination of STEM-EDX and electron microdiffraction for drawing the conclusions about bimetallic structure. XAS demonstrated that, from one side, the obtained N_{Pt-Pt} in first shell was 2.5 and N_{Pt-Ru} was 4.0. On the other hand, the N_{Ru-Pt} was three times smaller (0.7) and N_{Ru-Ru} was 5.4, which pointed out to a Ru-rich core nanoparticle. Interestingly, in the case of bulk Ru nanoparticles, *hcp* structure is normally expected. However, electron microdiffraction analysis showed *fcc* structure for bimetallic nanoparticles. These results demonstrate a high sensitivity of nanoscale effects in the formation of nanoparticles. Also, considering a nanoparticle with cuboctahedron *fcc* structure, significantly smaller average values of nanoparticle size were obtained, contradicting STEM analysis. However, when considering truncated (by a 111 plane) cuboctahedron hemispheric *fcc* nanoparticle, the value of 1.5 nm was in good agreement with the characterization performed by other techniques.

Another contribution from the same group[81] describes the core-shell inversion during *in situ* activation of the same bimetallic PtRu nanoparticles reported above. Initially the nanoparticles were characterized by a disordered structure containing Pt preferentially at the core (200 ºC). After heat

treatment at higher temperature (400 ºC), the nanoparticles adopted an inverted structure where Pt segregates to the surface.

Alayoglu et al.[78] also investigated PtRu system, with nanoparticles of ca. 4 nm synthesized either as alloy or core-shell by a multi-technique approach. The results demonstrated that in the core-shell system, as for the above case, Pt segregated to the shell and Ru to the core, but at this time Ru crystallized as highly distorted (typical) *hcp* structure. The EXAFS oscillations in this case were in phase with bulk phase at Ru edge (**Figure 1.7a**) and slightly phase-shifted at Pt edge (**Figure 1.7b**), confirming Ru segregation at the core of the nanoparticle and Pt distortion at the surface. On the other hand, the alloyed phase displayed significant shifts at different k-space oscillations respect to those of bulk counterparts, which indicates random distribution of Pt and Ru atoms in this system.

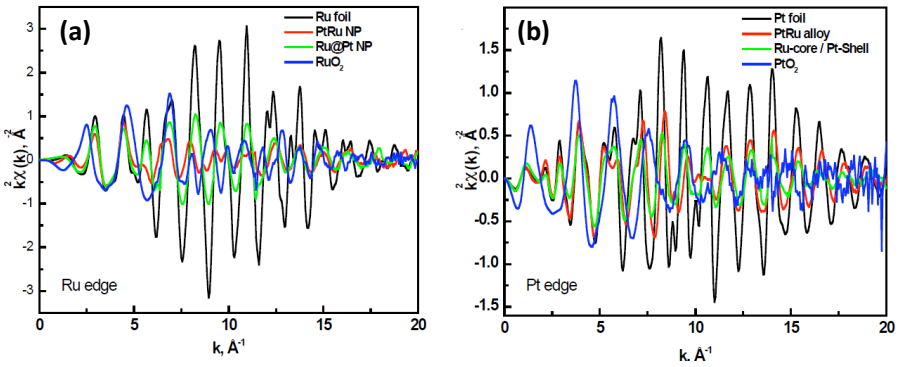

Figure 1.7. k^2-weighted $\chi(k)$ functions of Ru K-edge (a) and Pt L_{III}-edge (b) of different configured PtRu bimetallic nanoparticles and respective oxides and foil references. (Adapted from reference[78])

One approach that is worth mentioning comes from Iglesia's group and it is interesting in the context of this thesis. The authors encapsulated metal nanoparticles (Pd, Pt, Ru, Rh, Au) within zeolites (mainly small-pore ones which serve as "containers" for stabilization of metallic species). In one of few publications[82-85] they studied bimetallic AuPd, AuPt and PdPt clusters encapsulated within LTA zeolite.[86] Despite the extensive characterization on the bimetallic-zeolite system, only indirect information about bimetallic species was obtained by the other techniques, which led them to use XAS for a complete understanding about the system.

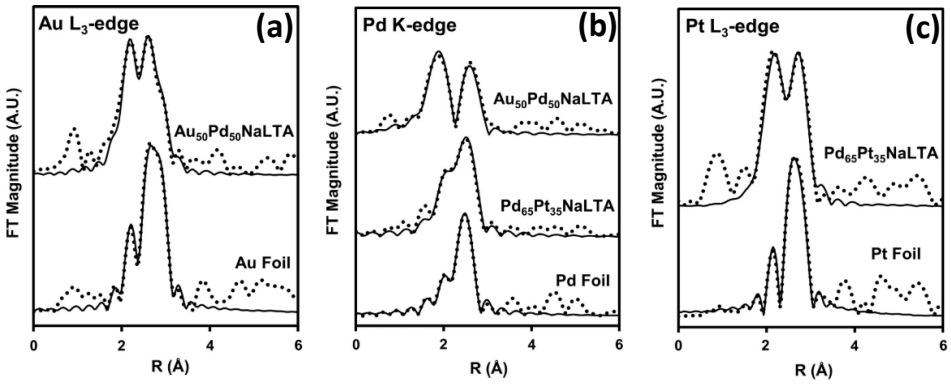

Figure 1.8. |FT| of k^3-weighted $\chi(k)$ of bimetallic samples and respective standards at Au L_{III}-edge (a), Pd K-edge (b) and Pt L_{III}-edge (c). (Adapted from reference[86])

The authors studied the three samples at Pd K-edge and L_{III}-edges of Au and Pt. As shown in **Figure 1.8**, by comparing the |FT| of metal foils with those of the samples, in almost all cases a split first shell contribution is visible, which is a good

indication of the presence of truly bimetallic system. Both metal edges fitting were performed to ensure data reliability (metal distances and Debye-Waller factors). In the case of AuPd nanoparticles (**Figure 1.8a**) the fit at gold edge resulted in Au-Au and Au-Pd coordination numbers of 6.0 ± 1.0 and 3.2 ± 0.8 at distances of 2.73 ± 0.02 Å and 2.73 ± 0.01 Å, respectively, so that the first shell mean coordination number was composed by ca. 9.0 metallic neighbors. The fitting of same sample at Pd K-edge (**Figure 1.8b -** top) resulted in Pd-Pd coordination number of 3.1 ± 0.7 at a distance of 2.69 ± 0.01 Å and a Pd-Au coordination number of 5.0 ± 1.0 at a distance of 2.73 ± 0.01 Å (first shell average coordination number of ca. 8.0), which demonstrated a good similarity of first shell coordination number for both metal edges and indicated that Au and Pd are in intimate contact and homogeneously dispersed within the nanoparticle. The results for PdPt-based system (**Figure 1.8c**) were very similar to those for AuPd nanoparticles. Particle sizes were extracted from total average coordination number (N_{A-B} + N_{B-A}) using similar approaches to those commented for monometallic at the beginning of this section and were in agreement with TEM observations (between 1-2 nm). Moreover, all distances were consistent with nanoparticulated systems, i.e. shorter than those observed for bulk bimetallic lattices.

In this thesis, we have extensively used zeolitic materials for hosting metallic nanoparticles. Then, this family of materials

deserves a brief explanation about their structures and properties.

1.1.2 Metal-exchanged zeolites and isomorphous substitution

The origin of the term zeolite born in 1756 when Alex F. Cronsted, a Swedish mineralogist, noticed that when heating a mineral (stilbite) vapors were released. Cronsted named this family of minerals as zeolites, from the Greek, boiling stone (where *zeo* means "boiling" and *lithos* means "stone").[87-88] The most appropriate definition of zeolite is matter of discussion, therefore, the IZA (International Zeolite Association), the most important organization in the zeolite area, says that any three-dimensional network structure composed of tetrahedrally coordinated atoms, bonded together by oxygen atoms and with a structural density of less than 21 tetrahedrally coordinated atoms (T atoms) per 1000$Å^3$ can be considered as zeolite or zeolite-like materials (aluminum phosphates, silicoaluminophosphates and metal-containing aluminum phosphates).[89]

From the point of view of their structure, the zeolites are made of TO_4 tetrahedra (T = Si, Al, Ti, Sn, among others), linked to TO_4 neighbors by sharing oxygen atoms. In a structure composed only by silicon tetrahedra, the combination of the TO_4 units (T = Si) leads to the formation of an uncharged silica (SiO_2), similar to quartz. However, the isomorphous substitution of Si^{4+} atoms of the silica structure by Al^{3+} atoms creates an electronic unbalance, resulting in a negatively charged material.

To preserve the electronic neutrality, the presence of charge-compensating cations is required. For each substituted Al atom, one negative charge is created that is neutralized by the positive charge of a compensation cation (Na^+, Ca^{2+}, K^+, TMA^+, etc), which remains electrostatically attached to the zeolite structure, as summarized in **Figure 1.9**. It is thanks to this electronic unbalance in the zeolite framework that the zeolites have cation exchange properties.

Notoriously, when the structural negative charge is compensated by protons, the resulting materials possess strong Brönsted acid properties that have boosted the zeolite applications in industry.

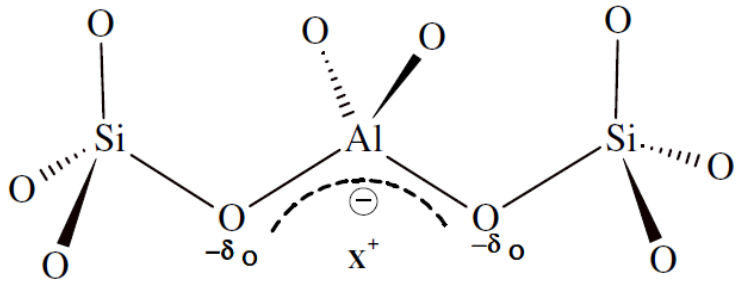

Figure 1.9. Structural scheme of a zeolite, where X represents the compensation cation.

Generally, the chemical composition of the zeolites is expressed as follows:

$$M\ x/n\ [(AlO_2)_x(SiO_2)_y] \bullet mH_2O$$

Where:

M = cation with *n* valence

n = valence of M cation

m = number of water molecules

x + y = total number of tetrahedral per unit cell

y/x = Si/Al atomic ratio, which can vary from 1 to infinite (according to Loewenstein rule)

According to the Loewenstein rule there are no Al-O-Al linkages in the crystal lattice, so only 50% of the Si in the crystal structure can be replaced by Al atoms.[90] This is due to the instability of these hypothetical compositions which are not stable because of the repulsion between the very close negative charges generated. However, there are some exceptions, such as zeolites obtained by high temperature methods and also the *bicchulite* mineral, with sodalite type structure, which contains more Al than Si.[91] The smallest structural unit of a zeolite is the TO_4 tetrahedron (primary building unit), which can be linked in a different way to generates the secondary building units (SBU's), exemplified in **Figure 1.10**.[92]

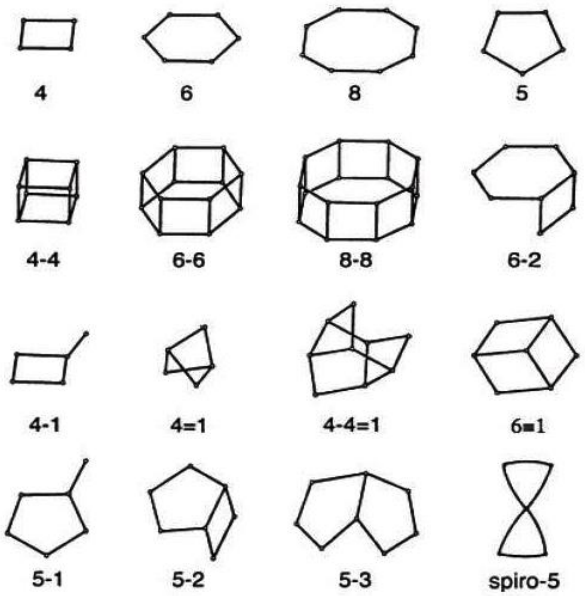

Figure 1.10. Secondary building units (SBU).

The linkage of these secondary building units between them generates more complex polyhedral units. A good example of polyhedron is the sodalite cage, which is an important building block in the construction of zeolites sodalite (SOD), A (LTA), ZSM-20 (EMT) and Y (FAU), when combined with others SBU's in a repetitive manner.

Some other examples of zeolite construction from secondary building units and polyhedra are illustrated in **Figure 1.11**, where the pore system formed is also observed.

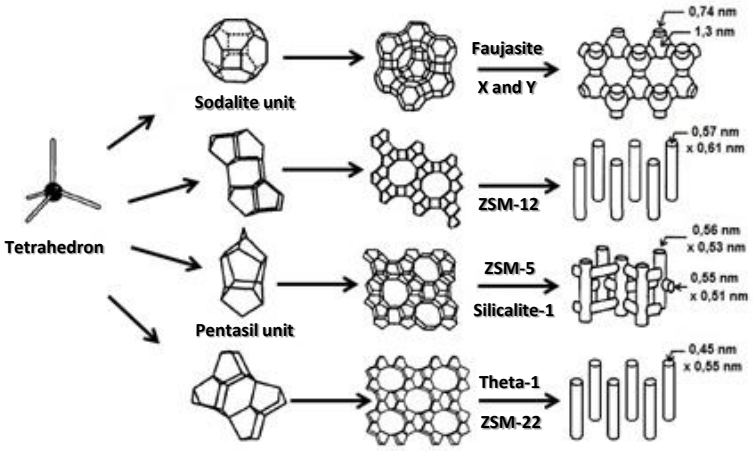

Figure 1.11. Formation of zeolitic materials from the simplest unit and growing until final products.[93]

In the classification of zeolitic materials the work of the Structure Commission of the International Zeolite Association (IZA) has been extremely useful. This commission is composed by experienced crystallographers, who regularly examine the proposals for new zeolite structures. Once the structure has been recognized by the commission, the structure is assigned with a three-letter code (FAU of Faujasite for zeolites X and Y, MTW for zeolite ZSM-12, MFI for zeolite ZSM-5 and silicalite-1; TON for zeolites Theta-1 and ZSM-22). Up to now, the Structure Commission of the IZA has accepted 234 different codes, that are of public access at IZA's website.[94]

The zeolites contain cavities and pores of different dimensions, which are classified by the number of T atoms at the pore aperture. According to the pore size, the zeolites can be

divided into chlatrasils, small, medium, large and extra-large pore zeolites, as summarized in **Table 1.1**.

Table 1.1. Summary of porous materials containing different pore characteristics.

Definition – pore size range (Å)	Material	Code	Atoms in pore aperture[a]	Pore diameter (Å)[a]
Macroporous (>500)	Pumice stone	-	-	-
Mesoporous (20-500)	MCM-41	M41S	-	15-100
Microporous (<20)	Zeolites			
Extra-large pore	Cloverite	-CLO	20	13.2 x 3.5
	VPI-5	VFI	18	12.7 x 12.7
	AlPO-8	AET	14	7.9 x 8.7
Large-pore	X and Y	FAU	12	7.4 x 7.4
	AlPO-5	AFI	12	7.3 x 7.3
	Beta	*BEA	12	6.6 x 6.7
Small-pore	ZSM-5	MFI	10	5.3 x 5.6
	MCM-22	MWW	10	5.5 x 4.0
Small-pore	A	LTA	8	4.1 x 4.1
	RHO	RHO	8	3.6 x 3.6
Chlatrasil	DDR	DDR	8	3.6 x 4.4

[a] main pore

As mentioned above, typical zeolites are composed basically by SiO_2 and Al_2O_3. However, other heteroelements different than Si and Al can be incorporated into the framework, such as Ti, Sn, Ga, Ge, Fe, among others. The isomorphous substitution of heteroatoms became important mainly after the discovery of Ti-Silicalite-1.[95] The so-called TS-1 is a titanosilicate zeolite with MFI topology, composed by Si and Ti, which was found to be an outstanding catalyst for oxidation reactions.[96-97] After this breakthrough, the interest in this area increased significantly due to the new opportunities that these novel materials created, either in the discovery of new zeolite structures (as for Ge-substituted zeolites)[98] or in their

application in reactions catalyzed by Lewis acid-containing zeolites (Ti, Sn, Hf, Nb, etc)[99-100].

Considering the variety of materials that could be prepared by isomorphous substitution and taking into account that each metal has its own chemistry, a different metallic speciation (either in the framework or not) might be expected depending on the synthesis conditions used to prepare zeolites. The different pH normally used for the synthesis (either basic or neutral media) can give rise to the formation of insoluble species which precipitate as extraframework material (in the form of metal oxides/hydroxides). It is known that the presence of extraframework species can hindrance the catalytic activity and in some cases is difficult to track by usual laboratory techniques. Despite the complexity, the X-ray absorption spectroscopy is of great importance in the characterization of metal-substituted zeolites due to its element-sensitivity character and has been successfully used for this purpose through literature.[1]

Due to the high number of publications related to TS-1 characterization, it is far to start discussing the isomorphous substitution in zeolites from it. It was a question of interest to assess the exact nature of Ti incorporated in TS-1 (and other Ti-containing zeolites) and several hypothesis were discussed from the 80's to the beginning of 90's.[1] Bordiga et al.[101-102] proposed that Ti active sites in TS-1 were the isolated Ti(IV) atoms incorporated within MFI framework, but many other environments for the active titanium species were proposed

before, such as titanyl groups, extraframework defect sites, monomeric or dimeric metal species and others.[103-107] Also, diverse local geometries were taking into account, ranging from tetrahedral, square pyramidal up to octahedral.[1] Unfortunately, TS-1 syntheses were not identical among the different characterization groups and therefore, it was not clear if the different claimed Ti species were a result of the different interpretation of the characterization techniques or the discrepancies came from the differences between TS-1 samples. In addition, the relatively small amount of titanium (ca. 3 wt.% of TiO_2) feasible to be incorporated in the zeolitic structure makes difficult the characterization once the experimental data are dominated by features of SiO_2 matrix.[1]

Titanium atoms present in Ti-containing materials were found to occupy a 6-fold octahedral environment (TiO_2 anatase and rutile) while in a zeolite the atoms were forced to be in a tetrahedral coordination (4-fold).[1] By this way, there was an important repercussion on XANES spectra of Ti-zeolites in comparison with titanium-based standards: the XANES spectra of calcined TS-1 showed a narrow and intense pre-edge peak at 4967 eV characteristic of 1s → 3p electronic transition related to Ti(IV) in tetrahedral coordination.[101-102] Conversely, in anatase, rutile and ETS-10 titanosilicate, where the Ti(IV) atoms were present in octahedral coordination, the pre-edge was characterized to be much less intense due to the small p-d hybridization which takes place in octahedral local

environment.[108-110] On the other hand, when the sample was not submitted to calcination (with organic cations occluded within pores), the pre-edge peak intensity was strongly diminished due to the presence of additional atoms coming from the TPA^+ template into titanium coordination shell, increasing the symmetry and favoring the p-d hybridization.[111] Similar behavior was observed when TS-1 interacted with reactants such as ammonia and water.[101-102] The EXAFS fits for the template unburnt sample was only possible introducing an additional C/N/O atom as first shell contribution, validating the XANES observations.[111] It is important to highlight that the insertion of a N atom from the template in the fit, as stated by the authors, seems odd from structural point of view and it must be discussed carefully.

Taking into account that a coordination number of 4 was expected for the metal in isomorphous substituted zeolites, for TS-1 higher values were observed.[101-102, 111-112] However, the obtaining of such value was strongly related to the presence of "closed" $Ti(OSi)_4$ sites (**Figure 1.12a**), i.e. a defect-free zeolite. Conversely, an average coordination number of 5 was expected for samples with a considerable fraction of "open" sites $Ti(OSi)_3OH$ (**Figure 1.12b**). In practical terms, both environments have 4 chemically bonded oxygens but for the latter, despite of three Ti-O-Si and one Ti-OH, fifth oxygen from an adjacent Si was observed, resultant of Ti-O-Si broken.[1] The final average coordination number obtained was dictated by

the amount of Ti incorporated. This has been demonstrated by a systematic study on ten TS-1 samples with different TiO_2 content (ranging from 0.97 to 3.59 wt.%).[113] N_{Ti-O} values higher than 4 were obtained in most cases, evidencing the presence of both closed and open sites regardless the metal amount. Also, samples with high loadings exhibited values closer to 4, while low loadings produce the opposite (values close to 5). All coordination number assumptions were confirmed by pre-edge peak intensities, supporting the EXAFS fittings.

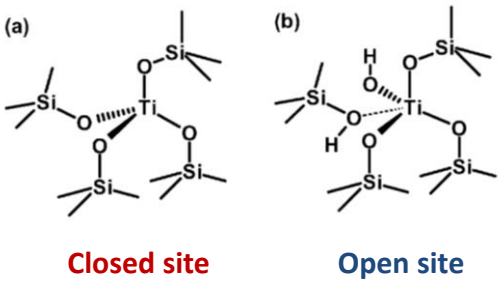

Figure 1.12. Two possible Ti local environments in TS-1: closed site (a) and open site (b). (Adapted from reference[113])

Upon calcination, the metal in titanosilicates and aluminosilicates remains tetrahedrally coordinated without any modification in terms of speciation (unless it is treated under harsh conditions). On the contrary, Fe and Ga-containing zeolites behave differently and metal migration to extraframework was observed,[111] however without compromising the catalytic activity.[1] The phenomenon of migration from framework to extraframework positions was

characterized by a damping of the χ(k) functions which was related to the reduction of first shell intensity (Fe/Ga-O contribution) attributed to the decrease in the coordination number N (**Table 1.2**). The damping can be correlated to the high heterogeneity of extraframework (in terms of coordination number and distances) species, causing higher Debye-Waller factor values (σ^2) (**Table 1.2**). This behavior was characterized to be the opposite of the well-ordered Ga-O or Fe-O first shells with N = 4 and well-defined distances found in zeolites.

Table 1.2. Metal-substituted MFI zeolites and their activation treatment (Template = No Treatment), and results of the EXAFS data analysis for the catalysts measured in different conditions.[a] (Adapted from reference[114-115])

M-zeolite	Calcination (ºC)	N_{M-O}	R_{M-O} (Å)	DWF (Å)
Ga	Template	4.2 ± 0.3	1.82 ± 0.01	$(5 \pm 1) \times 10^{-2}$
	500	3.4 ± 0.3	1.80 ± 0.01	$(6 \pm 1) \times 10^{-2}$
	700	2.5 ± 0.4	1.78 ± 0.02	$(5 \pm 2) \times 10^{-2}$
Fe	Template	3.8 ± 0.4	1.86 ± 0.01	$(4 \pm 1) \times 10^{-2}$
	500	1.7 ± 0.3	1.82 ± 0.02	$(6 \pm 1) \times 10^{-2}$
	700	1.2 ± 0.3	1.81 ± 0.03	$(6 \pm 2) \times 10^{-2}$

[a]EXAFS equation not valid for too disordered systems so the cumulant approach is indicated for that. For further details the original publication[114-115] is suggested.

Some other examples can be found in the literature for heteroatom-substituted in zeolites. One of them is the case of Sn-β, an important catalyst for biomass conversion, firstly synthesized by Corma's group.[116] The use of EXAFS for Sn-β characterization was fundamental since this zeolite is composed by a highly faulted intergrowth of two polymorphs, A and B, making the Rietveld refinement of X-ray diffraction data almost impossible.[117] The same authors observed a different Sn-O distance of metal-substituted zeolite (1.91 Å) respect to the

SnO_2 (2.05 Å), which indicated the change from octahedral to tetrahedral coordination of Sn when inserted in Sn-β structure. However, a small amount of SnO_2 was detected by the presence of the second shell contribution of SnO_2 (positioned between 2.5 and 4 Å). Further, using modelling and a multishell fitting approach, the authors suggested a preferential location (T5 site) of Sn in the β zeolite crystal structure.[117]

Diverse synthesis approaches have been used for improving the activity and selectivity of stannosilicates in biomass conversion reactions, some of them related to top-down synthesis. Dijkmans et al.[118] synthesized Sn-β via Sn-grafting after creation of silanol nests by previous dealumination of Al-containing beta zeolite, which resulted in a distinct local order when compared with traditionally hydrothermal synthesis, especially in terms of tin coordination (N_{Si-O} = 4 for hydrothermal synthesis vs N_{Si-O} = 3 for Sn-grafted material). As for the first example, the authors also used modeling to fit the data and construct their hypothesis, which points out the importance of modelling methods in this kind of system.[118] Other examples can be found with quite similar EXAFS results for Sn speciation.[119-120]

Different metal-substituted zeolite systems have also been investigated by EXAFS as the Nb and Ta-containing beta zeolites studied by Corma's group.[121] Both elements were applied as catalysts in Lewis acid-catalyzed reactions. Once Nb and Ta formal oxidation states are 5+, M=O bonds were

observed in both cases, apart from three siloxane bridges. For Nb, the fitting using two different Nb-O paths were mandatory while for Ta only one Ta-O contribution was necessary. Moreover, no extraframework or M-O-M contributions were observed, which indicated that both heteroelements were present as isolated species within the microporous matrix.[121]

Although the study of the local environment of aluminum in zeolites by ^{27}Al NMR is a consensus and well-established in the zeolitic community,[122] there are also some studies of Al speciation by XAS.[123-124] However, aluminum is a light element and its study by X-ray absorption spectroscopy requires soft X-rays, complicating *in situ* and *operando* studies due to the high absorption of soft X-rays by matter in general.[1]

The other way to introduce metals in zeolites, apart from encapsulation[82-86, 125-126] and impregnation[127] methods, is by the inclusion of cations in the ion-exchange positions generated by the presence of M^{3+} (M = Al, B, Ga, Fe) in the zeolitic framework.[37] These cations can serve as nanoparticle/clusters precursors[30, 128-130] or as catalytic sites themselves.[131-132] Several ion-exchanged cations within zeolites have been studied by XAS but here Cu and Ag-containing zeolites will be emphasized due to the high attention that these materials have received recently.

Copper-exchanged zeolites are relevant both industrial and academic point of views. These materials are active catalysts for selective catalytic reduction of NO_x, which is

responsible for converting it into nitrogen and water.[133] Diesel engines on ships, trains and automobiles contain this type of catalyst, which in the past was based on metal oxides (tungsten, vanadium, molybdenum), precious metal or, more recently, transition metal ions (Co,[134] Fe[135-137] and Cu[131, 133, 138-141]) in zeolites. Another reaction in which Cu-exchanged zeolites are used as catalysts is the conversion of methane to methanol. Direct conversion of methane (abundantly available) to a liquid would enable the transportation and a subsequent conversion into fuels or chemicals, making methanol quite interesting.[138]

Due to its outstanding performance in SCR process in terms of activity and stability, Cu-SSZ-13 catalyst with CHA framework (one of the structures used as carrier for silver-based systems of **Chapter 5**) was extensively studied by XAS in order to understand the behavior of copper local environment and valence state during activation of catalyst and also under reactions conditions. The location of copper ions was first addressed using XRD by Fickel and Lobo.[142] They demonstrated that Cu ions tend to be positioned at the center of 6-rings of CHA structure, since each 6-ring unit is likely to have one negatively charged tetrahedral with Al replacing Si, the copper atoms were expected to be shifted near to the charge. This hypothesis was supported by a later work[143] by studying both as-prepared and calcined Cu-CHA, pointing out to the copper atoms positioned off-axis of the 6-rings (Also observed by Deka et al.[144]) in a much better agreement respect to the

model of Cu in the plane of the ring. In addition, the coordination numbers found for hydrated and calcined samples were 4.0 and 3.2, respectively.

An interesting point concerning the hydration of copper ions inside the zeolitic structure was addressed by Ribeiro's group,[145] which found that Cu K-edge XANES spectrum of hydrated Cu-CHA (as-prepared) was closely related to Cu^{2+} ions in aqueous solution. In a comprehensive XAS study related to Cu-SSZ-13 activation, Borfecchia et al.[146] confirmed this observation. This highly cited paper discussed the influence of the atmosphere (either under O_2/He or He flow) during thermal activation on copper species within CHA framework. Upon activation (RT → 400 ºC) under oxidant atmosphere, copper atoms maintained the oxidation state (Cu^{2+}) but experienced a dehydration process, which was observed by a progressive decrease of the white line intensity in the XANES spectra. Moreover, the pre-edge peak (~8977.5 eV) typical from Cu^{2+} in low symmetry (related to 1s → 3d transition) was always observed during thermal treatment under O_2. In addition, the intensity of the first shell peak in |FT| was decreased due to the loss of water ligands.

On the contrary, upon activation under inert gas flow, the copper ions experienced autothermal reduction to Cu^{+} (as already observed for other Cu-zeolite systems[147]), with loss of typical pre-peak feature for Cu^{2+} and a shift of the absorption edge to lower energies. Comparing the EXAFS data from both

activation treatments, the authors found that He-treated samples was less coordinated respect to O_2-treated at the end of the treatment. However, the dehydration pathway was similar for both activation procedures up to 250 ºC. After that, the evolution in the spectrum of O_2-treated stopped while the He-treated still changed up to 400 ºC, which was an indicative of the presence of an extra-ligand coordinated to copper after oxidizing treatment. To confirm this hypothesis, the authors fitted the EXAFS data for the distinct activated samples using a number of DFT calculated model clusters with Cu (I and II) located at different sites of the zeolite (either close to one or two aluminum atoms of the framework) as shown in **Figure 1.13**.

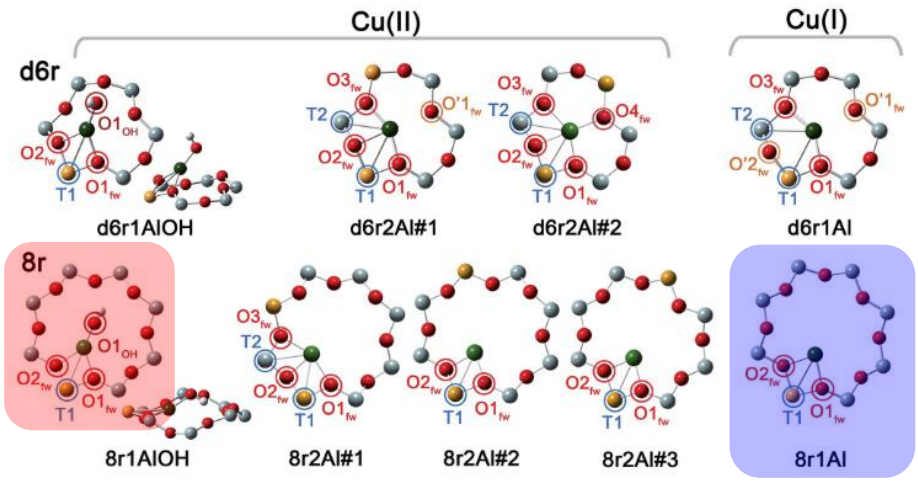

Figure 1.13. DFT-optimized structures highlighting the principal local coordination environment of Cu^{2+} and Cu^{+} sites in the CHA framework. (Adapted from reference[146])

The best models for activated Cu-CHA were those with Cu^{2+} in the 8-ring, as a $[Cu^{2+}(OH)^{-}]^{+}$ complex (red transparent marker in **Figure 1.13**) for O_2-treated sample, while for He-activated a bare Cu^{+} cation hosted mainly in the 8-ring (blue transparent marker in **Figure 1.13**) with a minority occupancy at d6r was found. The presence of $[Cu^{2+}(OH)^{-}]^{+}$ species was confirmed by IR, showing the ν(OH) stretching mode at 3657 cm^{-1} attributed to this site in a previous work.[148]

Still in the context of copper species on Cu-CHA system, XAS has been pivotal for uncovering reaction mechanisms, especially for SCR-NH_3, and several groups put a great effort to advance in the understanding of structure and reactivity of Cu active sites.

Two kinds of experiments have been proposed to dissect the mechanism of SCR-NH_3: one based on the evaluation of distinct copper species formed during *operando* conditions, while the other type of experiment aimed to analyze the copper species during contact with different gases that are present in the reaction feed (NO + O_2, NH_3 alone, NO + NH_3, etc). For more information about the several species formed in both approaches and proposed mechanism, contributions from van Bokhoven and Lamberti,[138] Janssens et al.[149] and Paolucci et al.[150] are suggested.

Unlike copper-containing zeolites, silver counterpart is much more complex due to the ability of silver to aggregate into clusters of different nuclearity (with consequent unlike sizes and

electronic properties) upon mild thermal treatments. Of course, this aggregation depends on the type of zeolite used for allocate the silver cations. Until now, the assignation of size and type of silver species in zeolites is quite vast and remains unclear. Also, a much less amount of studies regarding XAS studies on Ag-zeolites system have been published.

The group of Baba was one of the main contributors to the study of silver clusters formation in zeolites by XAS and also in the application of these materials as catalysts in the conversion of methane in presence of ethylene.[126, 128, 151-156] This group studied the clustering of silver upon mild treatments under H_2 atmosphere in zeolites A and Y with different silver exchange degrees. For the oxygen thermal activated (400 ºC) Ag-exchanged samples the authors proposed a three-shell model to fit the data of initial state of silver. This model was based on Ag-O, Ag-T (T = Si, Al) and Ag-Ag contributions for two split peaks at |FT|. From one side, the presence of Ag_2O after activation was excluded by the absence of typical XANES features from this compound. On the other side, the calculated Ag-O distance by EXAFS was longer than in the oxide compound, which was in agreement with other R_{Ag-O} found in literature for this kind of system.[30, 157] Moreover, R_{Ag-Ag} was significantly shorter than in the Ag foil, but similar to that of $Ag_4^{\delta+}$ cluster in ZSM-5.[158] Other models for data fitting were excluded due to inconsistencies between observed distances such as the Ag-Ag pair in linear Ag_3^+ (2.95-3.17 Å),[159] Ag_6^{3+}

cluster (2.92-2.94 Å),[160] and another three-shell model[161] with distances between (2.81-2.88 Å). When submitted to H_2 at 120 and 200 ºC, the Ag-Ag path became prominent instantaneously respect to other Ag-O and Ag-T contributions in both AgLTA zeolites, while for AgY the three scatterers were seen even after treatment in H_2 at 200 ºC, demonstrating the ability of zeolite framework to control the clustering of silver.

Other groups have also been active in the study of Ag clusters in zeolites applying XAS as fundamental characterization technique.[67, 162-164] Suzuki et al.[164] studied the cluster formation of silver within X zeolite after evacuation from RT up to 300 ºC. Initially, the sample showed two peaks (A and B) in the |FT| (**Figure 1.14**).

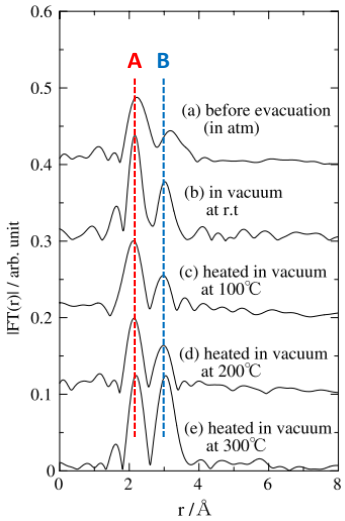

Figure 1.14. |FT| of χ(k) functions of evacuated AgX zeolite at different temperatures. (Adapted from reference[164])

The authors attributed the first one (A) to Ag-O_1 paths (H_2O molecules and framework oxygens), while the second one (B) was attributed to longer Ag-O_2 and Ag-Ag paths present at the same time. These paths were also named as three-shell model, but with an Ag-O longer distance path instead of Ag-T proposed by Baba's group (above-mentioned). By heating the sample up, the relative intensities between these two peaks changed, this indicated that a clustering process was taking place. When the sample measured at RT and atmospheric pressure was submitted to vacuum, all coordination numbers for the three proposed paths changed, which indicated that some water molecules coordinated to silver were removed and the silver atoms were sit near to the zeolite walls. With increasing temperature from RT up to 300 ºC under evacuation, Ag-$O_{1,2}$ paths remained almost unaltered or slightly modified. According to the authors, this pointed out to a mobility of silver within different sites of the structure. On the other hand, the N_{Ag-Ag} increased from 0.5 (100-200 ºC) to 2.9 at the end of the process (300 ºC). These values led the authors to conclude that Ag^+-based cluster inside the zeolite framework was formed.

Despite the interesting conclusions on silver clustering, it was not explained how the paths were selected for data analysis and a lack of discussion from XANES and other powerful tools of XAS was also noticed.

Lamberti et al.[157] have used an alternative approach to fit the data in AgFAU system in comparison with two above-cited

groups. By using Rietveld analysis from synchrotron-derived XRD data, the authors were able to localize the different crystallographic positions of ion-exchanged silver within FAU framework and used this information as output to build the models for EXAFS fitting. By this way, it was possible (even knowing it could be really complex) to know the crystallographic positions that were being modified during a clustering process. However, it is also completely understandable the fact that high quality XRD data and Rietveld analysis are necessary to following this approach.

Chapter 2

Objectives

The fundamental objective of this thesis is to study metallic-based catalysts during their thermal activation conditions using *in situ* X-ray absorption spectroscopy (XAS) as flagship technique for tracking the modifications in the local environment of metal centers at different steps (calcination, reduction, reoxidation). Two families of catalysts are studied by XAS, which are divided into two distinct topics along the work:

i) The first one is related to the influence of metal precursor on the formation and evolution of Pd nanoparticles supported on alumina and activated carbon during activation procedures.

ii) The other subject deals with the use of Ag-containing small-pore zeolites as precursor and nanocontainer for silver clusters and nanoparticles which are applied as catalysts in the selective catalytic oxidation of ammonia.

Moreover, another objective lies on the enhancement of human resources dedicated to X-ray absorption spectroscopy at the Instituto de Tecnología Química. As can be seen at the end of this document, several other systems are investigated in parallel (which are not included as complete content in this thesis).

Chapter 3

Experimental section

3.1 Preparation of Pd-based catalysts

The Pd-based catalysts (7 wt.%) have been prepared by impregnation and drying method using different Pd precursors, $Pd(OAc)_2$, $PdCl_2$ and $Pd(NO_3)_2$. To prepare them, γ-Al_2O_3 (Merck) or granular activated carbon (Norit GAC 1240W) were dispersed in an aqueous solution of the Pd precursor (containing the intended amount of Pd), to achieve a liquid to solid ratio of 5. The mixture was put into the rotary evaporator until all liquid phase was removed, resulting in a sample containing the carrier and the studied precursor (as-prepared). In case of $PdCl_2$, some drops of HCl were introduced in the solution to increase the solubility of precursor in water. Afterwards, the catalyst was dried at 100 ºC for 1 h and stored before calcination/reduction treatments.

The prepared catalysts were labeled as PdX-Y, where X stands for Al_2O_3 (Al) or activated carbon (C) and Y refers to the Pd precursor: palladium nitrate (N), palladium chloride (C) or palladium acetate (A), as shown in **Table 3.1**.

Table 3.1. Summary of prepared Pd-based catalysts.

Sample	Support	Precursor
PdAl-Ac	Al_2O_3	$Pd(OAc)_2$
PdAl-Cl		$PdCl_2$
PdAl-NO_3		$Pd(NO_3)_2$
PdC-Ac	Activated carbon	$Pd(OAc)_2$
PdC-Cl		$PdCl_2$
PdC-NO_3		$Pd(NO_3)_2$

3.2 Preparation of Ag-zeolites

In this work, two different silver-containing small-pore zeolites (CHA and RHO) with different chemical compositions were studied. Parameters such as Si/Al ratio, presence of co-cations and degree of silver exchange were evaluated. Thus, a summary description of the materials preparation (e.g. zeolite synthesis, ion-exchange processes and activation conditions) will be presented in the following sections.

3.2.1 Synthesis of zeolites

The framework structure of zeolite RHO (**Figure 3.1**) consists of large α cages linked via double eight-rings (D8Rs) to six other α cages, giving rise to a body-centered arrangement of two interpenetrating, but not interconnected pore systems. The zeolite possesses small-pores (3.6 x 3.6 Å in the pore aperture) and can be prepared with narrow chemical composition range (Si/Al around 4.5). This material showed excellent adsorptive properties, mainly due to the famous "trapdoor"-type behavior during CO_2 adsorption.[165]

The zeolite NaCs-RHO (Si/Al = 4.5) employed in this work was synthesized following a similar procedure reported by Chatelain.[166] The exact synthesis procedure was as follows: 0.94 g of crown ether 18-C-6, 0.705 g of CsOH and 0.34 g of NaOH were dissolved in 6.04 g of distilled water. Then, 1.32 g of sodium aluminate (54 wt.% Al_2O_3, 39 wt.% Na_2O) were added to the above solution and the resulting mixture was stirred until

a clear solution was formed. Subsequently, 10.5 g of colloidal silica (Ludox AS-40) were added and the resulting reaction mixture was stirred at room temperature for 24 h. The final gel composition was: 1.8 Na_2O: 0.3 Cs_2O: Al_2O_3: 10 SiO_2: 0.5 R: 100 H_2O where R is the crown ether 18-C-6. All chemicals were purchased from Sigma-Aldrich except sodium aluminate that was supplied by Carlo Erba. Zeolite crystallization was carried out in Teflon-lined stainless steel autoclaves at 125 ºC under rotation for 3 days. The zeolite RHO recovered after filtration, washed with distilled water and dried at 100 ºC, was calcined at 500 ºC for 3 h in order to remove the occluded organic material.

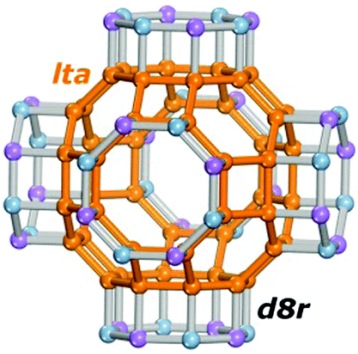

Figure 3.1. Schematic diagram of the RHO structure. (Adapted from reference[167])

Chabazite is also a very important small-pore zeolite (3.8 x 3.8 Å in the pore aperture) with three-dimensional structure (**Figure 3.2**) that consists of double six-rings (D6Rs) arranged in layers linked by tilted four-membered rings (4MRs).[168] Contrary to RHO, the chemical composition range that chabazite can be

synthesized is very broad (Si/Al from 2 to infinite). It has also been described its use in adsorption with "trapdoor"-type behavior due to the tunable pore entrance by the presence of extraframework charge compensating cations.[169] Also, this zeolite is widely used as catalyst in Methanol to Olefins process (MTO)[170-171] and more recently Cu-loaded chabazite (either the SSZ-13 zeolite or SAPO-34 zeotype) have received great attention in the selective catalytic reduction (SCR) of NO_x with ammonia.[133, 138-140, 146, 149]

In this work, zeolite K-CHA (Si/Al = 2) was synthesized from the gel composition: 2.65 K_2O: 1.0 Al_2O_3: 4.8 SiO_2: 183 H_2O, according to a published procedure.[172] Zeolite Y (CBV500), used as Si and Al source, was suspended in distilled water (64 mL) and an aqueous solution of potassium hydroxide (KOH; 9g; 98.5%; Fisher Chemicals) was added. The mixture was stirred for 1 h, and then was transferred into a polypropylene bottle. The gel was heated in the oven at 95 ºC for 4 days and the solid product was recovered by filtration, washed with distilled water, and dried at 100 ºC. The synthesis of CHA (Si/Al = 4.5) was carried out according to Zones.[173]

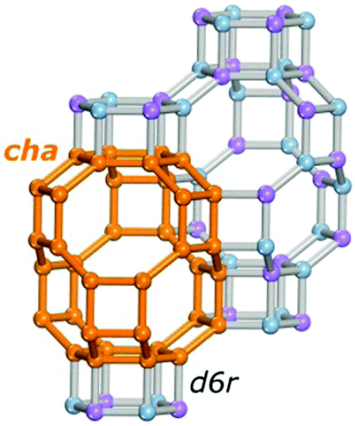

Figure 3.2. Schematic diagram of the CHA structure. (Adapted from reference[167])

3.2.2 Ion-exchange process (Ag incorporation)

The parent zeolites were ion-exchanged using $AgNO_3$ (ACS Reagent 99.9%) in order to obtain a 100% degree of Ag exchange (Ag/Al = 1), except for some cases that will be mentioned throughout the text. The ion-exchange procedure was performed in a Ag^+ solution using a solid/liquid ratio of 1/100 at 25 °C for 16 h, under mechanical stirring and in absence of light to avoid reduction of Ag^+ to Ag^0. Then, solids were filtered in darkness and washed with distilled water to remove excess of silver solution. Afterwards, the zeolite was dried at 100 °C for 24 h and stored in darkness. For the discussion of results obtained after ion-exchange process, the former NaCs-RHO and K-CHA will be named as AgCHA and AgRHO for simplification. The other samples were treated in such a way the nomenclature indicates the composition of the sample.

3.2.3 Ion-exchange process (Cs removal)

A repetitive ion-exchange procedure was performed in order to remove the Cs cations from NaCs-RHO zeolite for further treatments (e.g. preparation of AgNa-RHO). For that, 3M NH_4Cl solution was used as NH_4^+ source and successive ion-exchanges were performed. The processes were carried out at 60 °C (using a reflux) under mechanical stirring for 3 h, keeping the solid/liquid ratio of 1/10 and without a washing step between consecutive ion-exchange treatments (the liquid phase was separated by centrifugation). The experiments were repeated until Cs was not detected by EDS. Once the complete removal was achieved, the solids were filtered out and washed with 3 L of distilled water and dried at 100 ºC for 24 h.

3.2.4 Metal reduction and reoxidation

In order to study the influence of reduction temperature on the particle size of Ag species, the Ag-zeolites were thermally reduced under H_2 (100 mL/min – 10% H_2/He) at different temperatures (400, 200 and 100 °C) for 40 min at a heating rate of 10 °C/min. Nanoparticles redispersion within zeolite was carried out treating the reduced samples in O_2 flow (100 mL/min – 10% O_2/He) at 400 °C for 40 min at a heating rate of 10 °C/min. For comparison purposes, the samples were also submitted to treatments in pure O_2 and He at 400 °C for 40 min at a heating rate of 10 °C/min. Thermally reduced Ag-zeolites were labeled as $AgZEO_{RED\mathbf{X}}$, where "**X**" stands for the

reduction temperature (**X** = 400, 200 and 100 °C, respectively). Furthermore, the samples after redispersion (reoxidation after reduction) process were denoted as AgZEO-R**X**O, where "**X**" stands for the reduction temperature (**X** = 400, 200 and 100 °C, respectively) while "O" refers to the oxidative treatment at 400 °C after reduction. The samples treated under He and O_2 were labeled as "O_2 (or He) – **AT**", where "**AT**" stands for after thermal treatment. The term AgZEO is related to silver exchanged on a specific zeolite structure and ZEO is exchanged by the three letter code specific for each framework (e.g. CHA or RHO).

3.2.5 SCO-NH_3 catalytic experiments

SCO-NH_3 activity measurements over the Ag-zeolites catalysts were carried out in a fixed-bed quartz tubular reactor of 1.2 cm of diameter and 20 cm of length, using a gas mixture of 500 ppm of NH_3, 7 vol% O_2 and N_2 as a balance. Total flow rate and amount of catalyst were 800 mL/min and 0.25 g, respectively; resulting in 53.3 mL $NH_3 \cdot s^{-1} \cdot g^{-1}$ of GHSV for the catalytic experiments. The outlet gases were analyzed by three on-line detectors: UV-based detector for monitoring the NH_3 (EMX400 Tethys Instruments), an analyzer with infrared principles for N_2O analysis (4900 Servomex) and a chemiluminescence analyzer which allows the quantification of NO_x concentration (42C Thermo). In order to study the influence of the thermal decomposition of NH_3 and the effect of

the parent zeolite, the activity measurements in these conditions were performed.

3.3 Characterization by laboratory techniques

3.3.1 Chemical analysis by Inductively Coupled Plasma-Optical Emission Spectrometry (ICP-OES)

The chemical analysis of the studied materials was carried out by ICP-OES in a Varian 715-ES. The powder samples (approx. 20-30 mg) were dissolved in an acid mixture of 20%HNO_3:20%HF:60%HCl (% volume). In all cases, the calibration curve was fitted to the predicted approximate concentration of analyte and determined using standard solutions (Aldrich).

3.3.2 Thermogravimetric analysis

The thermogravimetric analysis (TGA) studies changes in physicochemical properties (e.g. mass) of a determined sample as a function of increasing temperature (with constant heating hate) or as a function of time (with constant temperature). In this work, TGA analysis was carried out to following the decomposition process of palladium precursors. The analyses were performed in an alumina pan with a Mettler Toledo TGA/SDTA 851e by increasing temperature under flowing air from ambient to 700 ºC at a heating rate of 10 ºC/min.

3.3.3 X-ray powder diffraction (XRD)

The phenomenon of X-ray diffraction takes place when a solid interacts with a monochromatic beam of X-rays of wavelength similar to the interplanar spaces of crystalline structures (~1 Å). The diffraction is the combination of two physical phenomena: coherent scattering and constructive interference. Diffraction peaks (diffraction maxima) will result when coherently scattered X-ray photons of the same λ constructively interfere. The technique is described by the Bragg law, which relates the incident angle of the radiation to the interplanar space for each diffraction peak, according to the following **Equation 3.1**:

$$n\lambda = 2d_{hkl} \cdot sen\theta \qquad \textbf{Equation 3.1}$$

Where:

d: interplanar space of crystalline planes with Miller indices (*hkl*)

λ: wavelength of incident X-ray beam

θ: incident angle of X-rays

This technique allows the identification of crystalline phases and their modifications, since crystalline solids possess characteristic diffractograms allowing qualitative and also quantitative analysis.

In this thesis, the structural parameters of materials were evaluated by XRD using a Philips X'Pert diffractometer

operating at 45 kV and 40 mA and equipped with a graphite monochromator and using Cu Kα radiation (λ = 1.542 Å). For Pd-based catalysts, XRD patterns were compared with crystallographic JCPDS standards of PdO (00-006-0515), γ-Al_2O_3 (00-010-0425) and $AlCl_3.6H_2O$ (00-008-0453). In case of treated Ag-containing zeolites, the XRD patterns were compared to Ag^0 (00-004-0783) and Ag_2O (00-012-0793) JCPDS crystallographic files, apart from that of zeolites CHA (00-034-0137) and RHO (00-027-0015) zeolites.

3.3.4 Textural properties

Textural properties were determined from N_2 adsorption isotherms measured at −196 ºC in an ASAP-2420 equipment (Micromeritics). Prior to the adsorption measurements, the samples were degassed at 400 ºC (for γ-Al_2O_3) and 200 ºC (for activated carbon) overnight. Specific surface areas (S_{BET}) were obtained using BET (Brunauer-Emmett-Teller) method[174] at relative pressures (p/p^0) ranging from 0.05 to 0.1 and 0.02 to 0.09 for catalysts based on alumina and carbon, respectively. Micropore volume for Pd/C catalysts was derived from t-plot method[175] at relative pressures (p/p^0) ranging from 0.39 to 0.64. The total pore volumes were determined using the Gurvich rule at p/p^0 of 0.97.[176]

3.3.5 Field Emission Scanning Electron Microscopy (FESEM)

The morphology of the samples was studied by FESEM using a ZEISS Ultra-55 microscope. The sample powder was deposited in double-sided tape and analyzed without metal covering by means of collecting either secondary or backscattered electrons (in separate measurements).

3.3.6 Transmission Electron Microscopy (TEM)

Metallic particle sizes were studied by electron microscopy in a JEOL-JEM-2100F microscope operating at 200 kV in transmission mode (TEM). The samples were previously reduced under H_2 flow (10 % H_2/He or pure H_2) at variable temperatures (depending on the study). Prior to microscopy analysis, the samples were suspended in dichloromethane and submitted to ultrasonication for approximately one minute. Afterwards, the suspension was let to slowly decant and a drop was extracted from the top side and placed on a carbon-coated nickel grid. Metal particle size histograms were generated upon measurement of more than 200 particles from several micrographs taken at different positions on the TEM grid.

3.3.7 CO chemisorption

The gas chemisorption technique employs simple molecules (e.g. H_2, CO) to quantify the metallic surface in reduced catalysts through a chemisorption process. Metallic

surface area and metal dispersion can be obtained using determined stoichiometric and geometric approximations.[177]

In this work, the active metal surface area (and consequently metal dispersion) and average crystallite size of Pd nanoparticles in Pd-based catalysts were studied by CO chemisorption. The analyses were done using a Quantachrome Autosorb-1C. The samples (ca. 0.3 g) were allocated inside U shaped glass tube and reduced *in situ* under H_2 at 200 ºC for 2.3 h. After reduction, the samples were degassed and cooled to 35 ºC to register the adsorption isotherm. Dispersion and nanoparticle sizes were calculated assuming CO/Pd = 1 and spherical shape of nanoparticles.

3.3.8 ^{29}Si, ^{27}Al and ^{109}Ag MAS NMR

Magic Angle Spinning Nuclear Magnetic Resonance (MAS NMR) is a suitable technique to characterize solid catalysts and useful to understand the environment present around the studied nucleus. Solid-state NMR spectra were recorded at room temperature with a Bruker AV 400 spectrometer. ^{29}Si MAS NMR spectra were recorded with a spinning rate of 5 kHz at 79.459 MHz with a 55° pulse length of 3.5 μs and repetition time of 180 s. ^{27}Al MAS NMR spectra were recorded with a spinning rate of 10 kHz and a 9° pulse length of 0.5 μs with a 1 s repetition time. ^{29}Si and ^{27}Al chemical shifts were referenced to tetramethylsilane and $Al^{3+}(H_2O)_6$, respectively. ^{109}Ag MAS NMR experiments were recorded at

18.60 MHz using a 7 mm probe and spinning the samples at 5 kHz. $AgNO_3$ was used as a reference ($\delta = 0$ ppm).

3.3.9 UV-Vis spectroscopy

UV-Vis spectroscopy measures the electronic transitions taking place from low-energy to high-energy atomic or molecular orbitals when the material is irradiated with light at those wavelengths (UV and visible). Electronic transitions may take place in transition metal ions (d-d and ligand-to-metal or metal-to-ligand charge transfer transitions), inorganic and organic molecules (mainly $n \rightarrow \pi^*$ and $\pi \rightarrow \pi^*$ transitions). For solids, preparation of transparent films is quite challenging which makes transmission experiments often used for gases and liquids almost impossible. As an alternative, the spectrum can be collected by diffuse reflectance (DR). In this way, it is possible to obtain information about the oxidation state and coordination environment of transition metal ions in catalytic solids.[178] A UV-Vis Cary 5000 spectrometer equipped with a diffuse reflectance accessory (Praying Mantis Harrick) was used for UV-Vis spectroscopic measurements. The spectra were taken using $BaSO_4$ as internal standard.

3.4 XAS measurements

X-ray absorption spectroscopy was the flagship technique used in this thesis to characterize the Pd and Ag local environments in metal-based materials under activation and

catalytic conditions. Currently, XAS is still a scarce technique and the obtaining of data is completely related to the competitive system of proposals submission to large facilities. This thesis presents data obtained from several projects granted with XAS beamtime in most synchrotrons around Europe, so it is convenient to describe the technique with some detail below.

3.4.1 Synchrotron radiation

An X-ray source is necessary to scan a XAS spectrum continuously through different energies. The best way to do that is to use a synchrotron light source, or in a simple way, a synchrotron. In this machine (main components are depicted in **Figure 3.3** – the following bold numbers within the text are related to main individual machine components), electrons are emitted through a linear accelerator (**1** - linac) and pass to a circular accelerator called booster (**2**) where are accelerated by strong magnetic fields until reach the required speed (near the light speed). Once the electrons are traveling near the light speed the machine injects them into a storage ring (**3**) (with a circumference of hundreds of meters) to produce wide energy X-rays (so-called synchrotron radiation). The ring is composed by straight and curved sections. In the curved ones, magnetic fields created by bending magnets accelerate the electrons in a circular way and after changes in the electrons trajectory the broad-range X-rays are generated.[179]

Additional X-rays can be provided by using insertion devices formed by arrays of magnets arranged in the straight sections. The generated X-rays coming either from bending magnets or insertion devices are then targeted to beamlines (**4**), where the beam is tuned (optical hutch) and the whole instrumentation needed for the experiments and their control are mounted (detectors, sample environment, etc). The main components of a synchrotron radiation facility commented above are represented in **Figure 3.3**.

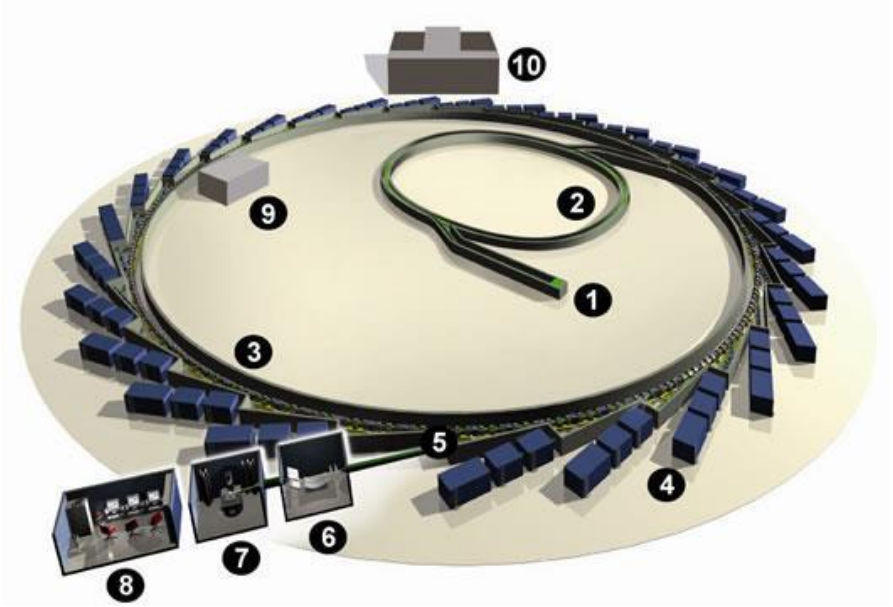

Figure 3.3. Main components of a synchrotron light source, where: (1) Injection system - electron gun and linac, (2) Booster, (3) Storage ring, (4) Beamlines, (5) Front ends, (6) Optics hutch, (7) Experimental hutch, (8) Control cabin, (9) Radiofrequency (RF) cavity and (10) Synchrotron staff house.[180]

The synchrotron light sources are classified by generations, with different features for each one, mainly due to the technological possibilities at the time that machines were built.[179] The installations are classified as follows:

1- First-generation sources are composed by the first storage rings, what were originally made for particle physics, which differs from the purposes that are currently intended.
2- Second-generation sources were designed to be X-ray sources.
3- Third-generation sources are designed and built to have the insertion devices in the straight sections and to possess beams with significantly better collimation.

Currently, the successors to third-generation synchrotrons are available, such as free electron lasers and energy recovery linacs. Free electron lasers displays extremely intense X-rays in extremely short pulses. At the same time, the radiation damage can be high due to such intense pulses. This type of machine is useful for the study of sub-picosecond time resolution of chemical reactions. On the other hand, energy recovery linacs are more similar to storage rings but the intensity is significantly higher. Both facilities are called fourth-generation sources, despite the huge difference between them.[179]

The beam originated by a synchrotron can be characterized by a concept called brilliance (**Figure 3.4**), which

is known as the number of photons per second per square millimeter of area per square milliradian of solid angle within a bandwidth of 0.1% of any given energy.[181] A typical brilliance offered by bending magnets is in the range of 10^{14}-10^{15} (usual units) at around 10 keV (energy for XAS experiments, for example). Despite the possibilities of tuning the X-rays using mirrors and monochromators (important factor that limits the beamlines energy capabilities), for example, the brilliance cannot be increased by optical means.[179] However, by using tools such as wigglers and undulators, the brilliance can increase significantly up to four orders of magnitude.[179] It is important to mention that not always more brilliance is better, because in determined studies, especially in biology, the samples are beam sensitive and can be damaged during the measurements. On the other hand, in samples where the concentration of absorbing element is very low and beam resistance is high, this might be very useful.

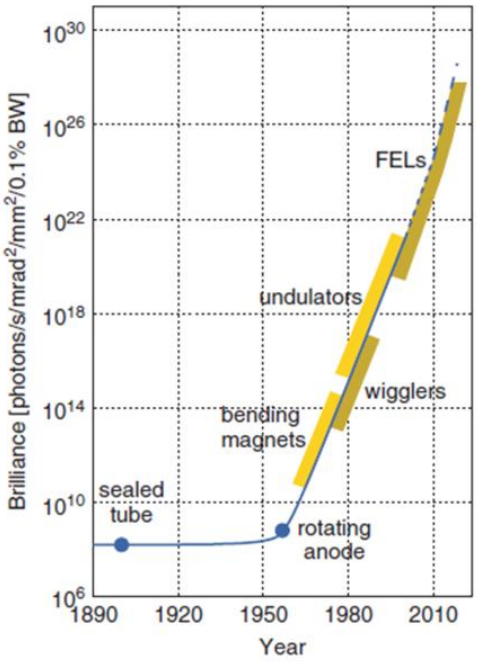

Figure 3.4. The brilliance of X-ray sources: a historical graph showing the enormous increase in brilliance starting from the second half of the twentieth century. (Adapted from reference[182])

3.4.2 Interaction of X-ray with matter, XAS and related phenomena

When X-rays interact with matter, mainly two processes can take place: absorption and scattering.[183-184]

The absorption measures the capability of a material to attenuate a photon beam, providing information about the distribution of energy levels of a sample and giving insights on its electronic properties. The absorption of a photon (which consequently give all its energy to the atom)[184] brings the

system to its excited state and depending on the excitation level some photoelectrons can be emitted, opening the doors for the study of photoelectrons properties by emission spectroscopy. The absorption attenuation can be measured directly by means of a transmission experiment, where the attenuation of a photon beam passing through a sample is determined as a function of the incoming photon energy. The indirect way is by measuring the secondary processes related to the absorption, such as the yield of the photoemitted electrons or the consequence of a decay process (fluorescence photons, Auger electrons, etc).[183] In more energetic regimen (use of hard X-rays) the appearance of fluorescence photons are favored while for less energetic cases (soft X-rays) the Auger process is dominant.[185] The **Figure 3.5** exemplifies both ways cited above.

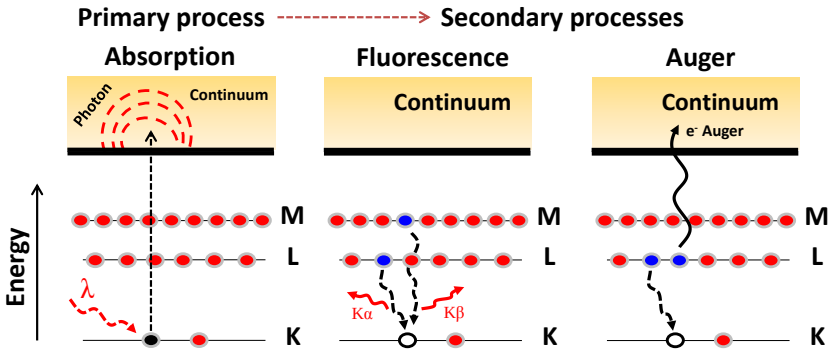

Figure 3.5. X-ray absorption (primary) and consequent decay process (secondary).

The other mechanism of interaction of X-rays with matter (scattering) is characterized by the finite probability of an

X-ray to change its direction of propagation after diffusion through the sample. This diffusion can be elastic or inelastic, depending if an energy exchange between the photons and matter exists. If so, the process is called inelastic, where the outcoming photons have different energy respect to incoming ones. One example of elastic scattering process is the X-ray diffraction while Raman spectroscopy is based on inelastic scattering.[178, 183]

Considering both mechanisms which contributes to photon beam attenuation, in the energy range from 1 to 40 keV the absorption process is dominant respect to those of scattering (elastic and inelastic), as shown in **Figure 3.6**, where the solid line is predominantly intense respect to the others.[183]

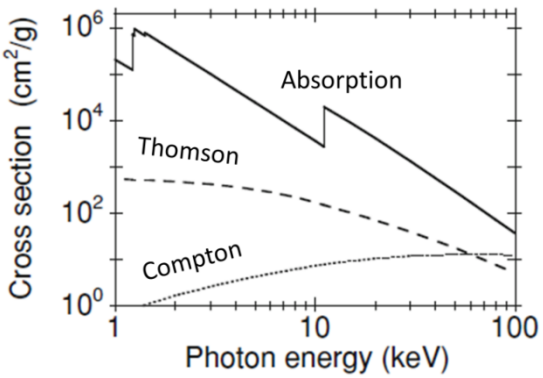

Figure 3.6. (a) X-ray absorption cross-sections for Ge. Solid line: photoelectric absorption, with the three L edges (1217, 1248 and 1414 keV) and the K edge (11103 keV); dashed line: elastic Thomson scattering; dotted line: inelastic Compton scattering. (Adapted from reference[183])

When discussing about X-ray absorption, it is fundamental to define the *absorption coefficient* μ, which measures the probability of a photon to be absorbed. When a collimated X-ray beam passes through a sample of *x* thickness, the intensity is diminished according to Lambert-Beer **Equation 3.2**:

$$I = I_0{}^{-\mu(E)x} \qquad \textbf{Equation 3.2}$$

where I_0 is the X-ray intensity incident on a sample, *x* is the sample thickness, and I is the transmitted intensity after photon attenuation. Moreover, the absorption coefficient depends on the sample composition and incident energy (E) of X-rays. So that with the increase in energy, there is a decrease in the absorption coefficient, which can be correlated with the decrease of the cross-section in **Figure 3.6**. This decreasing is given in first approximation by:[186]

$$\frac{\mu(E)}{\rho} \approx \frac{Z^4}{AE^3} \qquad \textbf{Equation 3.3}$$

where ρ is the sample density, Z the atomic number (i.e., the number of electrons) and A the atomic mass.[1] This is a fundamental property of X-rays and that is the reason this radiation is useful for medical and imaging applications such as X-ray computed tomography. Due to this Z^4 dependence, the absorption coefficient is different for each element, so that good

contrast between different materials (orders of magnitude) can be achieved by changing the X-ray energy.[187]

Notwithstanding, along solid line of **Figure 3.6**, sharp discontinuities related to absorption edges are visible, which take place when the photon has enough energy to extract an electron from a deep atomic level. Once every atom possesses specific core-level electrons with well-known binding energies, the selection of the appropriate absorption edge can be done tuning the energy of the X-ray, which makes XAS an element-specific technique. The **Table 3.2** exemplifies the relationship between the energy required from electron extraction and respective core levels. When the extracted electron comes from the most intern atomic level (1s), the absorption edge is called K-edge and so on.

Table 3.2. Electronic transitions as a function of core level.[183]

Transition	Absorption edge (core level)
1s → continuum	K
2s → continuum	L_I
2p → continuum	L_{II} and L_{III} ($2p_{1/2}$ and $2p_{3/2}$)
3s → continuum	M_I
3p → continuum	M_{II} and M_{III} ($3p_{1/2}$ and $3p_{3/2}$)
3d → continuum	M_{IV} and M_V ($3d_{3/2}$ and $3d_{5/2}$)

The edge energies change with atomic number approximately as Z^2, but both K and L levels can be used in the hard X-ray regime (M edges can serve for heavy elements in the soft X-ray regime, as well), which allows most elements to be probed by XAS with X-ray energies between 5 and 35 keV, as shown in **Figure 3.7**.

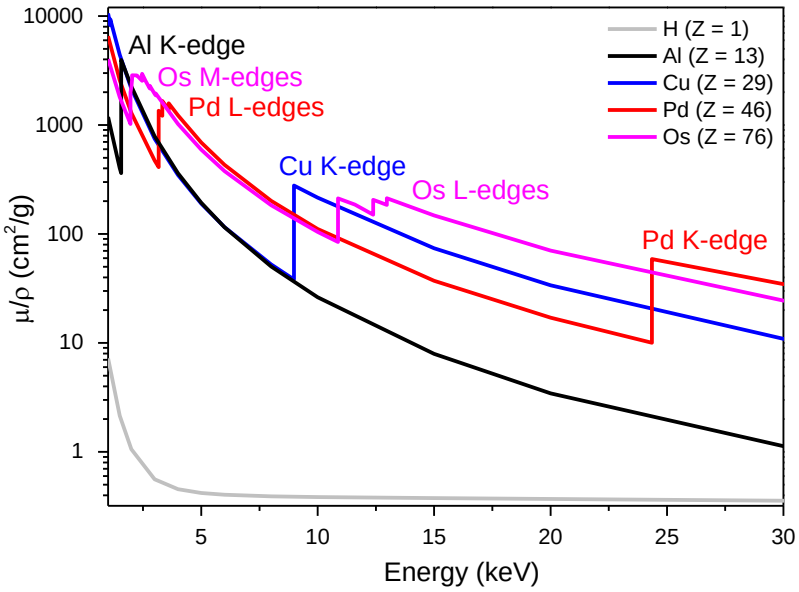

Figure 3.7. The absorption cross-section μ/ρ for several elements over the X-ray energy range 0-30 keV.

The absorption phenomena can be described by allowed dipole transitions which are more intense and predominant.[183] However, as for other spectroscopies, other less probable transitions can be present in a XAS spectrum following the selection rules (Fermi golden rules[188]), especially working with hard X-rays. For example, for the first period of transition metals on periodic table measured at K-edge, weak transitions 1s→3d before the absorption edge (which corresponds to the principal 1s→4p transition) appear. These transitions in metals with empty 3d orbitals are mainly due to local hybridization of 3d-4p orbitals as well as the possible quadrupole coupling.[189-190] Therefore, the presence of these transitions can be used as a

probe for geometry, with the intensity directly related to the centrosymmetric distortion around the studied atom: $I_{octahedral} < I_{square\ planar} < I_{tetrahedral}$.[189, 191]

A XAS spectrum can be divided into two regions, being the absorption edge (E_0) the most important feature present on it. The region surrounding the absorption edge is known as XANES (X-ray Absorption Near Edge) and comprises an energy range of $E_0 \pm 50$ eV. This region is important in the determination of the oxidation state, empty density of states (HOMO-LUMO) and geometry around the absorber. Since there are a high number of factors (longer mean free path of low energy photoelectrons enhances the multiple scattering terms)[183] that affect considerably the absorption energy, the mathematical interpretation and theory about XANES are complex. However, XANES are less dependent on statistics, sample and beam quality,[183] which makes this technique very suitable for distinct scientific areas, especially in catalysis.[192] Moreover, the thermal and structural disorder effects are generally weak close to the edge, this allows extremely high temperature measurements preserving the main structural information about the element. Moreover, the data collection is normally fast so time-resolved experiments can be performed even in the ps scale, which is important for tracking really time-sensitive states of catalysts.[193]

The qualitative character of XANES usually makes the data interpretation easier in comparison with EXAFS. Generally, the shape and position of absorption edge are very sensible to

variation in the formal oxidation state, ligand types and geometry around the absorber. Because of that, XANES is recognized as a fingerprint technique, where the studied sample is compared with references of well-known crystalline structure and oxidation state. Furthermore, by using models and reference compounds semi-quantitative information can be extracted through linear combination approach.[187] On the other hand, quantitative information based on theoretical simulations is quite complex to be obtained. The **Figure 3.8** shows two of the most classic examples of using XANES in the characterization of oxidation states.

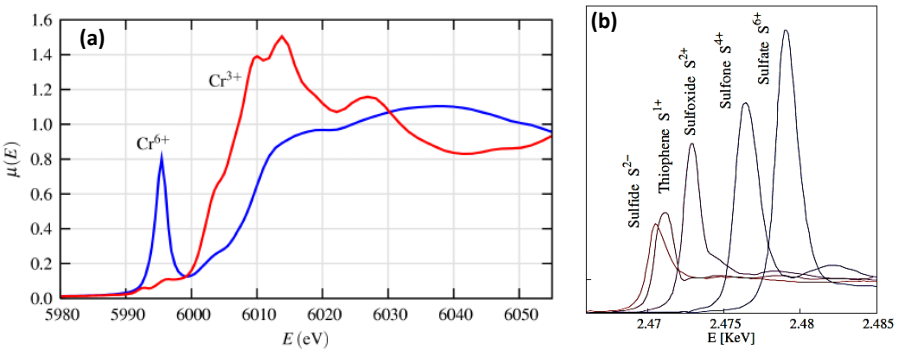

Figure 3.8. Cr K-edge XANES for Cr^{3+} and Cr^{6+} oxides (a) and Sulfur K-edge chemical shift in different S compounds (b). (Adapted from references[183, 187])

The first one in **Figure 3.8a** is the case of chromium oxides with different oxidation state, where the strong pre-edge peak in the Cr^{6+} spectrum is a consequence of the tetrahedral symmetry causing considerable overdue of the empty d-electron

orbitals with the p-states that the photoelectron must fill. The other example of **Figure 3.8b** is related to the shift in the absorption edge of S-containing samples, characteristic to the different formal oxidation state typical of each compound.

It is worth noticing that here it is not being considered the pre-edge region as a distinct part of a XAS spectrum, once it could be nicely correlated.

The second region of XAS spectra is called EXAFS (Extended X-ray Absorption Fine Structure) and comprises the range of (E_0 + 50 eV – E_0 +1000 eV), where the appearance of pronounced oscillations takes place. These oscillations (dominated by single scattering processes) are characteristic of interacting process between the "expulsed" photoelectron of the absorber with the electronic waves backscattered by neighborhood atoms (either in solids or liquid state). The crests in the absorption spectra are due to constructive interference of incoming and outcoming waves, whilst the valleys are characterized to be the opposite, as better visualized in **Figure 3.9**. As the photon energy increases a decreasing in the intensity of oscillations is observed, due to the short mean free path of the photoelectron, typically limited to about 10 Å, which makes EXAFS insensitive to long-range order.[183] Notwithstanding, the rigorous analysis of these oscillations allows one to have information about the local environment around the absorber.

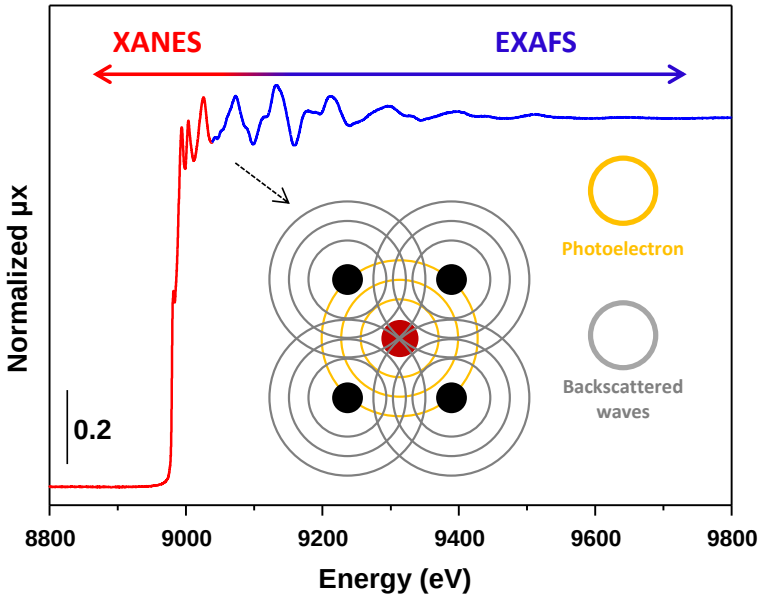

Figure 3.9. Normalized XAS spectra where both XANES (red) and EXAFS (blue) can be visualized as well as the backscattering process of incoming and outcoming waves giving rise to the spectra oscillations.

The EXAFS oscillations are described following the function χ(E) which takes into account solely the interactions with neighbor atoms[187]:

$$\chi(\mathrm{E}) = \frac{\mu(\mathrm{E}) - \mu_0(\mathrm{E})}{\Delta\mu_0(\mathrm{E})} \qquad \textbf{Equation 3.4}$$

Where:

μ(E) = absorption coefficient measurement

μ_0(E) = smoothed background function of isolated atom absorption

However, for a better understanding of EXAFS region an undulating behavior of photoelectron originated from the absorption process is assumed, converting the energy of X-rays to wavenumber of photoelectron (k) units in which the dimensions are distance^{-1} (so, k^{-1}) and is defined by[183, 187]:

$$k = \sqrt{\frac{2m(E - E_0)}{h^2}} \qquad \textbf{Equation 3.5}$$

Where:

E = measured energy

E_0 = electron excitation energy or energy of the absorption edge

m = electron mass

h = Planck constant

Taking it into account and considering the EXAFS oscillations are the sum of frequencies related to different coordination shells of the same neighbor atom, the **Equation 3.6** as function of k comes out[187]:

$$\chi(\mathrm{k}) = \sum_j \frac{N_j f_j(k) e^{-2k^2\sigma_j^2}}{kR_j^2} \sin[2kR_j + \delta_j(k)] \qquad \textbf{Equation 3.6}$$

Where:

f_j and δ_j = properties of photoelectric scattering of neighbor atoms

N_j = number of neighbor atoms (coordination number)

R_j = bond distance from absorber to neighbor atoms
σ^2 = thermal and static disorder on bond distances respect to the neighbor atoms

The application of above mentioned **Equation 3.6** allows the obtaining of type, number (N) and distance (R) of neighbor atoms surrounding the absorber element as well as the disorder factor (σ^2) that could be either thermal or static. The reader is referred to reference books and reviews for further details about fundamentals of XAS.[187, 194-196]

3.4.3 XAS experiment and data treatment

As already commented in the beginning of section *3.4.1*, a continuously tunable X-ray source with very high incident flux is required to resolve the fine structure of XAS spectra, which turns this technique synchrotron-dependent or synchrotron-only method.[181] Most EXAFS studies use hard X-rays mainly from 2 keV onwards. This regime comprises the K-edges for elements up to the second row of the transition metals in periodic table and L-edges for lanthanides and further heavier elements, in which the K-edge EXAFS measurement is unpractical,[181] as the case of Os in **Figure 3.10a**. A scheme representing the basic configuration for XAS measurements is found in **Figure 3.10b**, where the transmission and fluorescence modes are pictured. In the first case, the absorption coefficient at fixed energy E is obtained by measuring the intensity of the X-ray beam before the sample (I_0) and transmitted after the sample (I_1), usually

using two ionization chambers filled with proper gas mixture for energy range of interest. Once I_0 and I_1 are determined, μx (E) can be obtained (x is the sample thickness), through the Lambert Beer law:

$$\mu x\,(\mathrm{E}) = \ln\frac{I_0}{I_1} \qquad \textbf{Equation 3.7}$$

Moreover, a reference sample (e.g. a metal foil of the same element selected as the absorber element) is placed after the I_1 ionization chamber, followed by a third ionization chamber along the beam path (named as I_2 in **Figure 3.10b**). By this measurement approach it is possible to simultaneously acquire the XAS spectra for both the sample and the reference (using the I_1 and I_2 outputs) and use the latter for an accurate calibration of the sample spectrum.

Even if transmission is the most used mode due its accuracy and easiness, in several cases it is not applicable. For example, when the amount of absorber element is too low (excessively diluted) or the specimen is too thick or supported, fluorescence mode can be applied. By using this method, the incident intensity of beam is measured by I_0 ionization chamber, whilst a multi-element semiconductor detector positioned at 90º respect to the sample (which in turn is rotated at 45º) is used to collect the fluorescence photons (secondary process of the X-ray absorption phenomenon), as seen in **Figure 3.10b**. Here,

considering a linear response of the multi-element semiconductor detector, μx (E) is proportional to I_f/I_0.

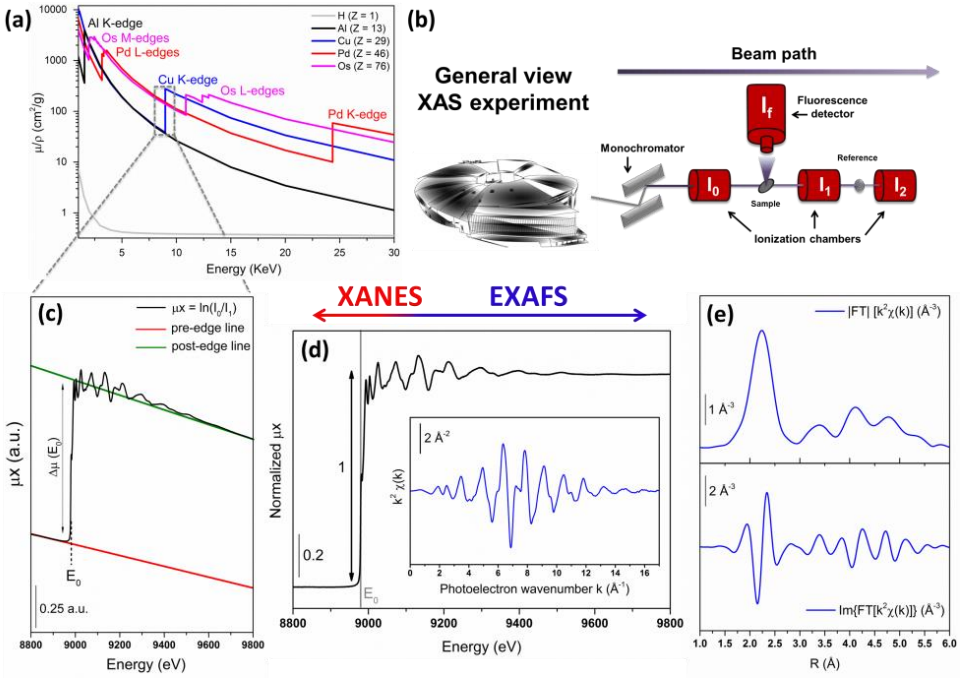

Figure 3.10. Schematic representation of general view of a XAS experiment and different steps of data reduction. See text for details. (Adapted from reference[1, 181])

One of interesting features of XAS lies in the fact that completely different spectra from different times can be compared after data normalization, regardless the measurement conditions (sample thickness, absorber concentration or detector configuration) or theoretical simulations. The normalization is generally done to the edge jump Δμ, as indicated in **Figure 3.10c**. The analysis of EXAFS spectra begins in k-space extracting the oscillatory part of μ(E) by subtraction of the

atomic-like background $\mu_0(E)$ from the normalized XAS spectrum, resulting into the determination of the EXAFS function $\chi(E)$. The function is then converted into $\chi(k)$ by using the **Equation 3.5** (inset of **Figure 3.10d**). Afterwards, $\chi(k)$ function can be Fourier-transformed to R-space, where the different coordination shells are easily seen as maxima in the modulus of the FT (**Figure 3.10e**).

For a better understanding of **Figure 3.10**, it is explained as following: (a) X-ray absorption coefficient as a function of the incident X-ray energy, in the 1–30 keV range, for a selection of elements commonly found in coordination compounds. In particular, $\mu(E)/\rho$ is reported for two "light" atoms, i.e. H (Z = 1) and Al (Z = 13), and three metals belonging to the 1st, 2nd and 3rd row of the transition metal series, i.e. Cu (Z = 29), Pd (Z = 46), and Os (Z = 76). The X-ray absorption edges found in the reported range are indicated for each element. Note the logarithmic scale of the ordinate axis. (b) Schematic representation of a typical experimental setup for XAS measurements: I_0, I_1, and I_2 are ionization chambers, I_f indicates a fluorescence detector. (c) Cu K-edge XAS spectrum (black thick line) for the Cu foil. In the figure are also reported: pre-edge (red) and post-edge (green) lines (obtained by fitting the experimental data with two polynomial functions in suitable pre and post-edge energy intervals) required to estimate the edge-jump $\mu(E_0)$ for normalization of the raw spectrum; atomic-like background $\mu_0(E)$ (not shown), employed in the extraction of the

EXAFS oscillations. (d) Normalized XAS signal for Cu foil obtained from the raw data reported in part (c). The inset shows the extracted k^2-weighted $\chi(k)$ EXAFS function obtained by subtracting the absorption signal expected for an isolated atom, labelled as $\mu_0(E)$ in part (c), and converting the E-values in k-values using the above-mentioned **Equation 3.5**. (e) R-space EXAFS spectra obtained by calculating the FT of the $k^2\chi(k)$ spectrum reported in the inset of part (d) in the 2–16 $Å^{-1}$ k-range; both modulus (top part) and imaginary part (bottom part) of the FT are reported.

3.4.4 Technique limitations

Even though XAS (especially EXAFS region) is well-understood and widespread, the technique has some limitations such as the following[197]:

- It is not possible to distinguish atoms with too similar atomic numbers like: C, O and N.
- The broadening of core-hole lifetime generated can make XAS spectra intrinsically broad, which difficult the detailed data interpretation, especially in XANES region at high energies.
- The uncertainty of coordination numbers obtained after fitting are elevated and strongly correlated with Debye-Waller factor (σ^2), i.e. thermal and static disorders. In the case of *in situ*/*operando* studies where high temperatures

or harsh conditions are used this should be taken into account.

- X-ray absorption spectroscopy is an average technique. The spectrum is composed by all signals coming from the absorber so that a sample with different absorber sites could be difficult to be studied.

3.4.5 Beamlines specifications

X-ray absorption experiments, at the Pd (24350 eV) and Ag (25514 eV) K-edges, were performed at the BL22 (CLÆSS) beamline of ALBA synchrotron (Cerdanyolla del Vallès, Spain).[198] The white beam was monochromatized using a Si (311) double crystal cooled by liquid nitrogen; harmonic rejection has been performed using Rh-coated silicon mirrors. The spectra were collected in transmission mode by means of the ionization chambers filled with appropriate gases (Pd K-edge: 93 % N_2 + 7 % Kr for I_0 and 17 % N_2 + 83 % Kr for I_1; Ag K-edge: 88 % N_2 + 12 % Kr for I_0 and 100 % Kr for I_1). Reference patterns (e.g. metal foil) were measured simultaneously between I_1 and I_2 and used for spectra alignment.

3.4.6 Sample environment

Samples in the form of self-supported pellets of optimized thickness (normally to obtain a jump of about 1, approximately), have been located inside an in-house built

multipurpose cell described by Guilera[199] allowing *in situ* experiments (**Figure 3.11**).

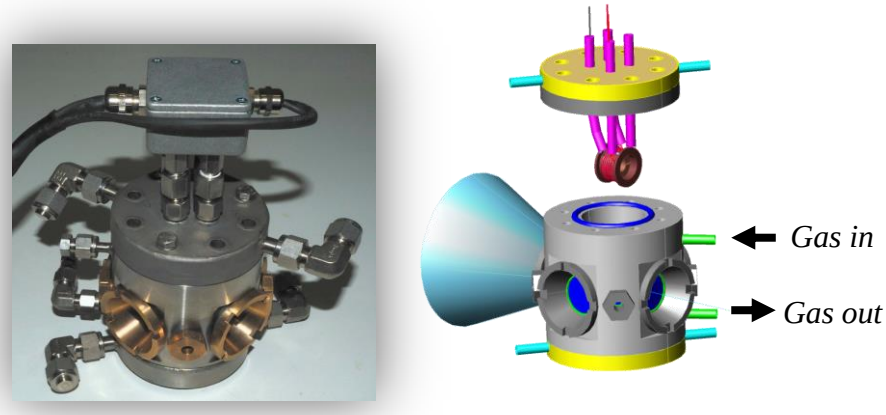

Figure 3.11. External view and scheme of the multipurpose *in situ* cell for solid-gas catalysis.

3.4.7 Measurement protocol for Pd-based catalysts

The spectra (sample + Pd foil reference) were collected at different steps (summarized in **Figure 3.12** – the measurements were launched at the beginning of each temperature step), starting from room temperature (25 ºC) up to 500 ºC at 10 ºC/min under O_2 flow (20 % O_2/He) in the calcination process, then the sample is cooled down to room temperature. After, the temperature is raised to 200 ºC at 10 ºC/min under H_2 flow (5 % H_2/He - reduction process) and then it is cooled down again. Several scans were acquired at each measurement step to ensure spectral reproducibility and good signal-to-noise ratio.

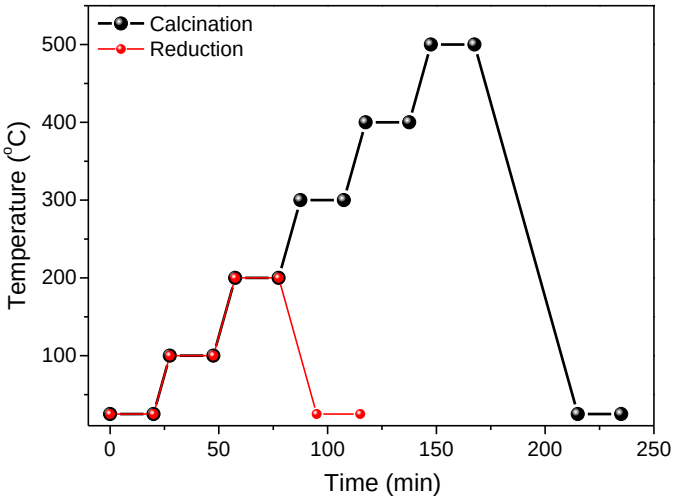

Figure 3.12. Experimental steps used in the XAS study of Pd-based catalysts: calcination under O_2/He flow (black line) and reduction under H_2/He flow (red line).

3.4.8 Measurement protocol for Ag-based catalysts

In a similar way as detailed for the Pd catalysts, the spectra of Ag-based materials were collected at different steps (summarized in **Figure 3.13** – the measurements were launched at the beginning of each temperature step). Three temperature profiles were carried out during this study, all of them starting from room temperature (25 ºC) up to determined limit of temperature at 10 ºC/min, as explained in schemes (a), (b) or (c) of **Figure 3.13**.

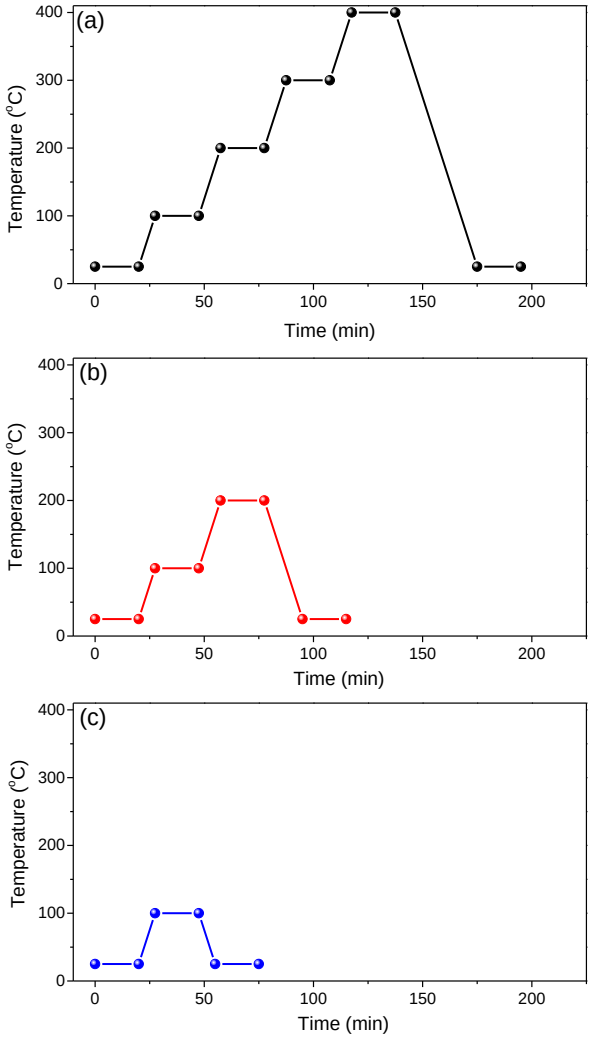

Figure 3.13. Experimental steps used in the XAS study of Ag-containing zeolites: treatment at 400 ºC (a), 200 ºC (b) and 100 ºC (c).

During single treatments (only reduction in H_2 or calcinations in He and O_2) the profile (a) was adopted for acquiring the data. In the study of silver reduction/reoxidation,

the three profiles were used in the reduction step followed by a reoxidation according to profile (a), i.e. the temperature of metal reduction was varied while the reoxidations were carried out always in the same way (RT → 400 ºC → RT). Several scans were acquired at each measurement step (allowing 20 min for temperature stabilization in each step) to ensure spectral reproducibility and good signal-to-noise ratio.

3.4.9 Data treatment

The data reduction and extraction of the $\chi(k)$ function has been performed using Athena code.[200] EXAFS data analysis has been performed using Artemis software.[200] Two methodologies of data fitting were adopted during this thesis: regular data fitting and corefinement approach. In the first one independent N, R, ΔE_0 and σ^2 parameters were refined for each spectrum. The latter is based on constraining determined parameters in order to decrease correlation problems usually found in XAS data analysis. As common strategy, the ΔE_0 is let to vary but fixed (and equal) for spectra with atoms in same local environment and the Debye-Waller factor can be constrained considering similar disorder within the absorber atoms. These strategies were adopted due to the reliability of the fits in terms of small errors. Additional information will be displayed as a note below the table of EXAFS results. Phase and amplitudes have been calculated by FEFF6 code using crystallographic files for well-known Pd- and Ag-based standards as input. In the case

of as-made AgCHA and AgRHO spectra, crystallographic data of similar materials were used, which were modified in order to obtain experimentally reasonable results. Specifically, the FEFF file used to fit the AgCHA data was built based on DFT calculations considering two crystallographic positions within CuCHA structure (**Figure 3.14 - bottom**). On the other hand, the FEFF file used to fit the AgRHO data was built using experimental XRD data of NaRHO available in literature (**Figure 3.14 - top**). In both cases the input file was a modified CIF file considering silver as cations instead Cu and Na.

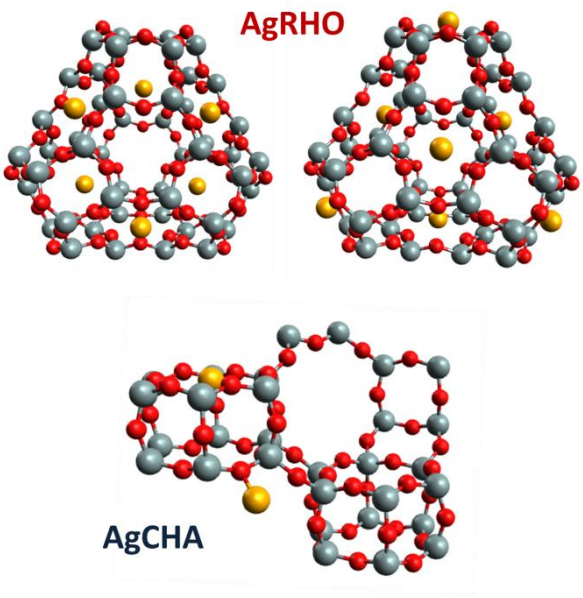

Figure 3.14. Hypothetical clusters with silver crystallographic sites used for EXAFS data analysis of as-made AgRHO (top) and AgCHA (bottom).

The average particle size of Pd has been obtained following the method used by Agostini et al.[11, 79]. In this approach, layers of atoms are built around a central one giving a determined dimension and a particle shape need to be assumed (in our case, observed by TEM analysis, cuboctahedral). For face centered cubic (*fcc*) metals, the number of layers added is indicated by letter "*m*"[10] obtained by **equation 3.8**:

$$CN = \frac{24m(5m^2 + 3m + 1)}{10m^3 + 15m^2 + 11m + 3} \qquad \textbf{Equation 3.8}$$

where CN is the coordination number obtained from EXAFS data analysis. The relationship between the number *m* of layers and cluster dimension changes as a function of the lattice parameter and it is defined by the **equation 3.9**:

$$d(m) = 1.173am + 2R_{cov} \qquad \textbf{Equation 3.9}$$

where *a* is the cell parameter (3.889 for Pd) and R_{cov} the covalent radius of the chemical element considered (metallic distance obtained by EXAFS). It is worth noticing that, although this method does not put any constrain in particle size, the empirical construction method using **equation 3.9** does not allow obtaining particles with less than a complete shell around central atom. Nevertheless, below this limit it is not possible to define a real shape as there is not a unique complete shell of atoms which could be arranged in a precise way following *fcc* structure.

In a XAS spectrum the signal is composed by the contribution of a large number of absorbing atoms, and the distribution of scattering atoms in the neighborhood of each absorber is different due to the static or thermal disorder.[179] If the local disorder is small, the distance distribution within a coordination shell can be expressed as a Gaussian function. When EXAFS equation is used to express systems with large disorder, incorrect values can be obtained from fit parameters.[42] The non-symmetric or anharmonic distribution of bond lengths can be seen at elevated temperatures or caused by static disorder. This asymmetry can influence directly the Debye-Waller factor and phase shift, which have consequences on coordination numbers and distances determination. To overcome this issue, the cumulant approach has been adopted by few groups.[42]

The deviation of the radial distribution from the Gaussian shape is measured by coefficients C_n called cumulants (see reference literature[179, 201-202]). Odd cumulants should affect the phase of $\chi(k)$ while even cumulants affect its amplitude.[179] The first cumulant C_1, according to literature, can be expressed in different ways, while the second cumulant (C_2) is the Debye–Waller factor.[179] For coordination shells showing Gaussian-type distribution of bond lengths, all cumulants with $n > 2$ are zero and the regular EXAFS equation serves to yield correctly the target parameters. However, when a deviation of Gaussian shape takes place, the higher cumulants may be important. The third

cumulant (C_3) measures the asymmetry respect symmetric shape and the fourth cumulant (C_4) the sharpening or broadening of the radial distribution. The C_3 may be negative, positive of zero, although it is frequently positive, with values in the order of 0.001 Å^3. If C_3 is negative the bond distances were previously overestimated and viceversa. Its effect is well seen in PDF example of **Figure 3.15**, where the red curve is visibly shifted and with alternate shape respect to the Gaussian one (blue curve).[203]

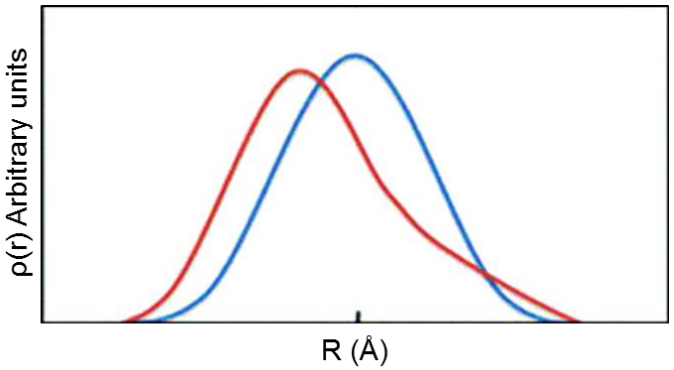

Figure 3.15. Effect of deviation (red curve) of Gaussian distribution (blue curve) frequently seen in disordered systems. (Adapted from literature[203])

Several studies describe radial distribution asymmetry in highly disordered systems like liquids, molten salts and alloys while in catalysis this issue has been addressed in much less extension. In this thesis, the third cumulant was included as parameter in some fits of **Chapter 5** aiming to evaluate the correct bond distances in different thermally treated Ag-loaded

zeolites. In the study of Pd-based catalysts, this methodology was preferably skipped due to the presence of palladium hydrides. Because of this, we have chosen not to include this methodology in the analysis of data in **Chapter 4**.

Chapter 4

XAS study on formation of precursor-dependent Pd nanoparticles

4.0 Introduction

Palladium-based catalysts are used since many years as selective heterogeneous catalysts for hydrogenation reactions in different industrial processes, from petrochemical to the synthesis of fine and bulk chemicals and removal of water pollutants.[25, 204-210] Since palladium is one of the rarest elements available on earth, the European Community has recently included this metal in the list of raw materials deemed critical in terms of supply risk.[211] Because of this, the control of the synthesis parameters of Pd-based catalysts, such as: metal precursor, activation method and type of support, should be evaluated for tuning the catalysts properties in order to ultimately impact the catalytic performance. On this optimization, proper characterization of the Pd-catalysts is a key stone for increasing catalytic activity and selectivity, while reducing the required amount of noble metal.

Among the variables that influence the catalyst activity, the study of metallic precursor is important due to the different decomposition pathway/kinetic of the precursor during catalyst activation processes (calcination/reduction).[37-38] Indeed, the nature of Pd precursor can determine the final properties of the metal nanoparticle, such as particle size and remaining undecomposed species, which could poison the catalysts.[212] A second important parameter is the type of the activation process, which influences the final activity of the Pd-based

hydrogenation catalysts. Also, the transformation *precursor to nanoparticle* can be dictated by the type of support due to its different thermal and chemical properties.[213] Therefore, systematic investigation that makes possible the characterization of complex and disordered nanoparticle systems capable to track information at different catalysts activation steps is essential for understanding the final catalytic performance of the Pd-based catalyst.

Currently, X-ray absorption spectroscopy is one of the most powerful tools for characterization of metal nanoparticles, due to its element-selective character, making possible the *in situ* follow-up of changes resulting from activation treatments, as already observed in literature.[214-217] Performing linear combinations, mixed phases can be characterized, since XANES features are considered the fingerprint of phases present in the sample.[195] Also, by analyzing the EXAFS region (either looking at the imaginary or real part of Fourier transform), the absorber neighbors with different scattering ($Z > 1$) can be discriminated, helping in the understanding of complex systems which cannot be characterized by other techniques due to the lack of order of these compounds. Moreover, with development of methods for data analysis/interpretation, it is possible to estimate nanoparticle size, shape and disorder in the nm range by different approaches.[46-47, 218-219] The combination of characterization techniques is being used to rationalize particle

size distribution interpretations, using EXAFS as a core technique.[11]

In the present chapter, we have studied the influence of the metal precursor on the formation of Pd species on two series of catalysts, using two types of supports (activated carbon and γ-alumina), as well as the activation procedure for yielding to the final catalysts. To do that, a comprehensive study by *in situ* X-ray absorption spectroscopy has been performed during catalysts activation (as-prepared/calcination/reduction), trying to follow the evolution and changes in the physicochemical properties (oxidation state, size of metal formed species) of the catalysts and the difference among them for further structure-reactivity relationships. Furthermore, an elegant approach has been used to determinate the fraction of oxidized Pd and undecomposed precursor, when the XAS spectrum is formed by both types of species. Finally, the consequences of different activation procedures have been discussed in terms of average coordination number obtained from EXAFS corefinement fits.

4.1 Results and Discussion

4.1.1 Characterization of supports and Pd-based catalysts

Crystallinity and crystal phase of samples were investigated by XRD. Patterns of Al_2O_3 supported catalysts (in their oxidized state), reported in **Figure 4.1a**, are dominated by reflections of γ-Al_2O_3. Lower intense peaks of alumina in PdAl-

Cl are due to loss of ordering attributed to acid treatment suffered by the sample during Pd impregnation with $PdCl_2$ + HCl (used for $PdCl_2$ solubilization). Besides, the support damage is also confirmed by the appearance of a peak at 27º attributed to $AlCl_3 \cdot 6H_2O$ formation. In addition to alumina peaks samples exhibit reflections at 34.5º angles assigned according literature data to PdO phase. This peak is much more pronounced for PdAl-NO_3 respect to catalysts synthesized with other precursors (not well visible for PdAl-Cl). This behavior is related to the easily decomposition of $Pd(NO_3)_2$ with temperature, which consequently results in the formation of PdO even during impregnation step.

On the other hand, the catalysts based on carbon (**Figure 4.1b**) present the broad peaks attributed to amorphous graphitic carbon which are suppressed after metal impregnation. As observed for PdAl-NO_3, the catalyst PdC-NO_3 also displays a peak due to PdO formation during impregnation step. No significant additional phase could be detected pointing out to well dispersed palladium species.

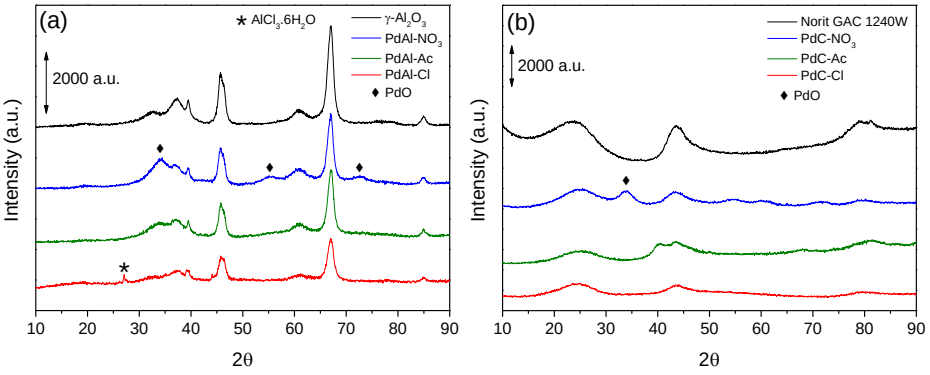

Figure 4.1. X-ray diffraction patterns of the as-made Pd-supported on γ-Al_2O_3 (a) and activated carbon (b) catalysts as well as their supports.

In order to evaluate the textural properties and consequently possible pore blockage, N_2 adsorption isotherms (**Figure 4.2**) for the Pd-based catalysts and supports were performed and the derived textural properties are summarized in **Table 4.1**. Catalysts based on γ-Al_2O_3 (**Figure 4.2a**) present Type III isotherms, characteristic of non-porous or macroporous solids. In this case, the isotherms do not present Point B and consequently no identifiable monolayer generation. Moreover, the adsorbed molecules are grouped around most favorable sites on the surface of solid and most of amount adsorbed remain close to saturation pressure (i.e., at $p/p^0 = 1$).[220] As γ-Al_2O_3 used in this work does not present micropores, the contribution of micropores to S_{BET} is negligible. Conversely, the catalysts based on activated carbon (**Figure 4.2b**) show Type I isotherms, which are given by microporous solids having relatively small external

surfaces. The steep increase in quantity adsorbed at very low p/p^0 is due to enhanced adsorbent-adsorptive interactions in narrow micropores of molecular dimensions, resulting in the filling of these pores at very low p/p^0. Between two Type I isotherms, the studied samples can be classified as Type I(b), typical of materials with pore size distributions over a broader range including wider micropores and possibly narrow mesopores (< 2.5 nm).[220]

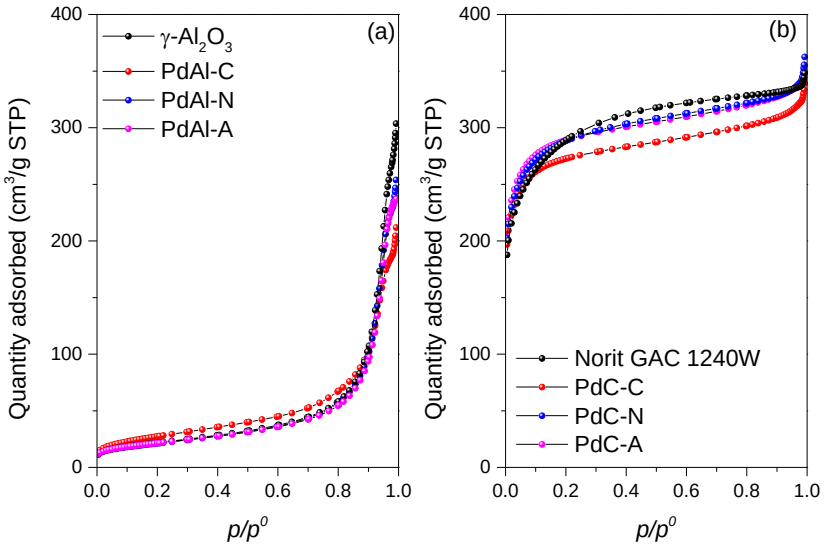

Figure 4.2. N_2 adsorption isotherms for the activated Pd-supported on γ-Al_2O_3 (a) and activated carbon (b) catalysts as well as their supports.

The PdAl-Cl catalyst presented a slightly higher surface area (97 m^2/g) and decreased TPV value (0.28 cm^3/g) among the studied catalysts using γ-Al_2O_3 as support, which can be

explained by the partially modification of support (as seen by XRD) suffered by the addition of HCl drops during metal impregnation. The other catalysts present roughly the same textural properties in comparison with γ-Al_2O_3 (difference of 13% in TPV), demonstrating that metal impregnation does not affect the porosity of the system. The textural properties of carbon-based Pd catalysts remain essentially unchanged with respect to the original activated carbon as is shown in **Table 4.1**, regardless the nature of the Pd precursor used for catalyst preparation.

The Pd content of the catalysts measured by ICP-OES is presented in **Table 4.1**. The concentration of Pd in the catalysts supported on alumina is in good agreement with the targeted value (7 wt.%), with little deviation between 1-2% for PdAl-Ac (6.9 wt.%) and PdAl-Cl (7.2 wt.%). On the other hand, it was not possible to determinate the Pd content by ICP-OES on samples based on carbon due to insolubility of carbon materials in the acid mixture used for the measurement. Also, due to presence of ashes in the carbon composition, the determination of Pd content by other techniques becomes difficult working with this system.

Table 4.1. Chemical composition and textural properties of supports and Pd-based catalysts.

Sample	wt.% Pd	S_{BET} (m^2/g)	Vμ (cm^3/g)	TPV (cm^3/g)
γ-Al_2O_3	-	77	0	0.40
PdAl-Ac	6.9	76	0	0.35
PdAl-Cl	7.2	97	0	0.28
PdAl-NO_3	7.0	75	0	0.35
Activated carbon	-	1068	0.26	0.52
PdC-Ac	n.d.	1109	0.36	0.52
PdC-Cl	n.d.	1050	0.35	0.50
PdC-NO_3	n.d.	1094	0.33	0.52

4.1.2 Characterization of activation process of catalysts by XAS

It has been demonstrated that XAS can be a powerful technique in the *in situ* characterization of metal systems during catalysis and/or activation process, providing information on local and electronic structure of metal atoms present in the samples.[19, 28, 30, 135, 146, 221-227] In order to allow correct interpretation a set of reference compounds (Pd foil, PdO, $Pd(NO_3)_2$, $Pd(OAc)_2$, $PdCl_2$) was measured under ambient conditions and used as standards. **Figure 4.3** exhibits the XANES spectra (a) and k^3-weighted (phase-uncorrected) |FT| (b) of Pd standards with oxidation state 2+ and 0. All patterns have been chosen considering possible Pd local environments that could be present during the activation step of catalysts. The absorption edge feature for Pd metal at 24350 eV (better seen in first-derivative, inset of **Figure 4.3a**) is due 1s to 4d dipole forbidden transition according to the selection rules, $\Delta l=1$ and $\Delta j=1$, where l and j are the orbital angular momentum and the total angular momentum of the local density of states,

respectively.[228] The first oscillations of Pd metal appear immediately after the edge, positioned at 24367 and 24391 eV, referent to 1s→5p and 1s→4f electronic transitions,[228] respectively. These two strong features are due to the well-arranged local *fcc* structure, where 12 Pd atoms are coordinated at the same distance from the central Pd atom.[79] Therefore, the intensity of these features contains intrinsically information on the Pd particle size.

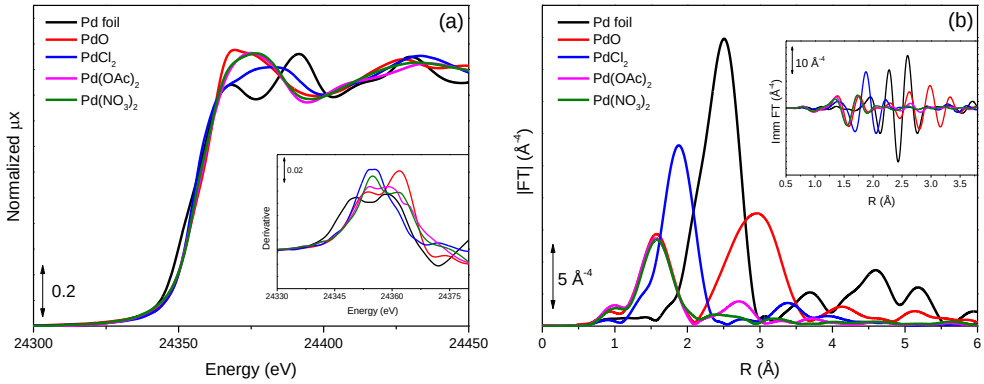

Figure 4.3. Normalized XANES spectra (a) and |FT| of the k^3-weighted phase-uncorrected χ(k) functions (b) of Pd standards. Inset (a) reports the first-derivative of XANES spectra while (b) shows the imaginary part of |FT|.

When the size of Pd metal particles is small, there is a large fraction of low coordinated atoms, causing low amplitude of the EXAFS oscillation.[228] Features in the pre-edge region are not observed in any spectra of patterns, which suggest centrosymmetric geometry around palladium atoms in any

temperature/atmosphere studied (which will be the case of all studied catalysts in this chapter).[192] For compounds with oxidation state 2+, such as PdO, $PdCl_2$, $Pd(OAc)_2$ and $Pd(NO_3)_2$ the energy threshold appears at 24354 eV. When a d-p orbital hybridization take place, as for Pd^{2+} compounds, a significantly strong absorption cross-section can be seen, compared with that of Pd foil.[228] The position and intensity of the peaks in the |FT| (**Figure 4.3b**) reflect the coordination and the distances around metal. The PdO, $Pd(OAc)_2$ and $Pd(NO_3)_2$ show the first coordination shell at the same position (~1.5 Å) in the k^3-weighted (phase-uncorrected) |FT|, characteristic of Pd-O bond in square-planar compounds. With the exception of PdO, which contain a significant contribution between 2-4 Å (red spectrum), the higher shells of $Pd(OAc)_2$ and $Pd(NO_3)_2$ are not easily visible and it is hard to discriminate even looking at the imaginary part of the |FT| (inset of **Figure 4.3b**). Unlike the oxygen-based standards, the $PdCl_2$ and Pd metal first shells lie at longer distances (1.88 Å for $PdCl_2$ and 2.5 Å for Pd^0, respectively) and are much more intense (15-20 $Å^{-4}$ in intensity) due to the presence of heavier atoms and/or in more quantity (e.g. 12 Pd first-neighbors in Pd metal). In case of overlapping of mixed phases (close R-values in |FT|), the imaginary part of Fourier transform is very informative and can help in the EXAFS data interpretation, for example, PdO and $PdCl_2$ exhibit the minimum position of first contribution at 1.57 and 1.69 Å,

respectively. Nonetheless, the first shell in Pd^0 and second and third shells of PdO are composed by Pd-Pd contributions and can be differentiated in the Imm of |FT| using the minimum at 2.79 and maximum at 2.97 Å of PdO which are not present in Pd metal spectrum.

The quantitative results derived from EXAFS data analysis of Pd standards are shown in **Table 4.2**.

Table 4.2. Summary of EXAFS fit of the Pd standards.

Standard	CN	S_0^2	Path	R (Å)	σ^2 (Å^2)	ΔE_0 (eV)	r-factor
Pd foil[b]	12	0.75(7)	Pd-Pd	2.743(3)	0.0053(5)	4.3(8)	0.0013
$PdCl_2$[c]	4	1.07(7)	Pd-Cl	2.314(2)	0.0033(3)	4.2(6)	0.0013
PdO[d]	4	0.77(7)	Pd-O	2.022(7)	0.0016(10)	-0.2(1.4)	0.0088
$Pd(OAc)_2$[d]	4	0.84(13)	Pd-O	2.001(10)	0.0021(8)	1.0(1.9)	0.0184

[a]The fits were performed on the first coordination shell (at different ΔR) over FT of the k^3-weighted χ(k) functions performed in the Δk = 2.3-13.7 Å^{-1} interval, resulting into a number of independent parameters of $2\Delta R\Delta k/\pi = 7.0$ (6.8 for Pd foil). Non optimized parameters are recognizable by the absence of the corresponding error bar. [b]ΔR = 2.0-3.0 Å; [c]ΔR = 1.4-2.4 Å; [d]ΔR = 1.0-2.0 Å.

For all optimized compounds, only the first coordination sphere was fitted using a specific k-range for each studied standard, depending on the distance of Pd-ligand path. For Pd metal foil, a characteristic coordination number of 12 is fixed according to bulk value and the Pd-Pd distance of 2.74 Å was obtained, typical of noble metals arranged in *fcc* local structure. The other standards exhibit coordination number of 4, typical of palladium compounds in oxidation state 2+ in square-planar geometry,[229] with distances Pd-O of 2.022 and 2.001 Å for PdO

and $Pd(OAc)_2$, respectively, and a distance Pd-Cl of 2.314 Å for $PdCl_2$, in accordance with crystallographic data of these compounds. All studied standards show a Debye-Waller factor typical of well-ordered materials.[28]

The state of Pd in the catalysts was evaluated in different stages of the activation process. The normalized XANES spectra collected during the activation process of PdAl-Ac catalyst are represented in **Figure 4.4,** bulk $Pd(OAc)_2$, PdO and Pd foil are also reported for comparison.

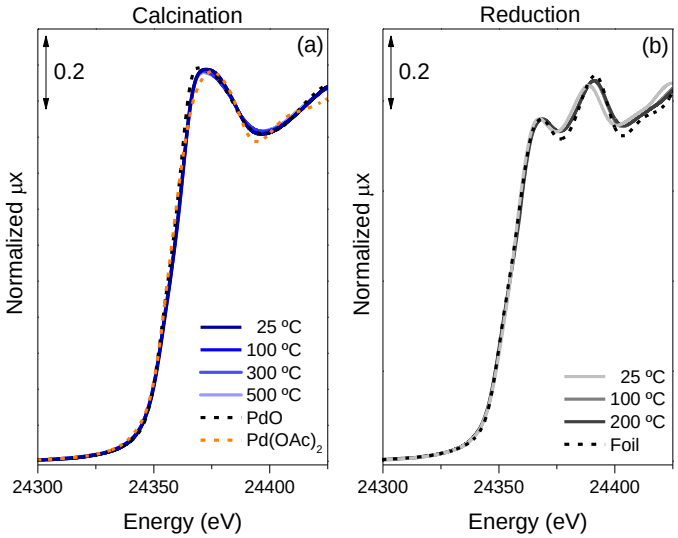

Figure 4.4. Normalized XANES spectra of PdAl-Ac during calcination in O_2 (a) and reduction in H_2 (b).

The spectrum of PdAl-Ac at room temperature reported in **Figure 4.4a** surprisingly presents the same features of PdO instead $Pd(OAc)_2$, indicating a decomposition of the organic

precursor during the impregnation/drying step with consequently formation of PdO. The absorption edge is positioned at 24354 eV during the whole calcination process, characteristic of Pd in oxidation state 2+. Nevertheless, when the atmosphere is changed to hydrogen (**Figure 4.4b)**, the edge is immediately displaced to 24350 eV even at room temperature, indicating a fast reduction of Pd^{2+} species to Pd^0. Also, the first oscillations beyond the edge are flattened respect to foil, indicating a large fraction of low coordinated Pd atoms. It is also worth noticing that at room temperature (in the beginning of reduction) the oscillations beyond edge are slightly shifted 3 eV to the left respect to spectrum of Pd metal foil, which could be explained by the formation of PdH_x, which decomposes at higher temperatures.[230-231]

The k^3-weighted phase-uncorrected $\chi(k)$ functions attributed to the calcination/reduction steps of PdAl-Ac catalyst are represented in **Figure 4.5** and compared to those of bulk $Pd(OAc)_2$ and PdO. As already discussed in XANES above, all spectra at different stages of activation are different compared to $Pd(OAc)_2$ and this is also reflected in the EXAFS signal. The intensity of oscillations shows the nanometric character of formed species during calcination (**Figure 4.5a**). In the reduction process (**Figure 4.5b)** the changes in intensity are more visible respect to normalized XANES, also the

displacements (0.3 $Å^{-1}$ compared to Pd^0) respect to the formation of palladium hydride is visible, as well as its decomposition.

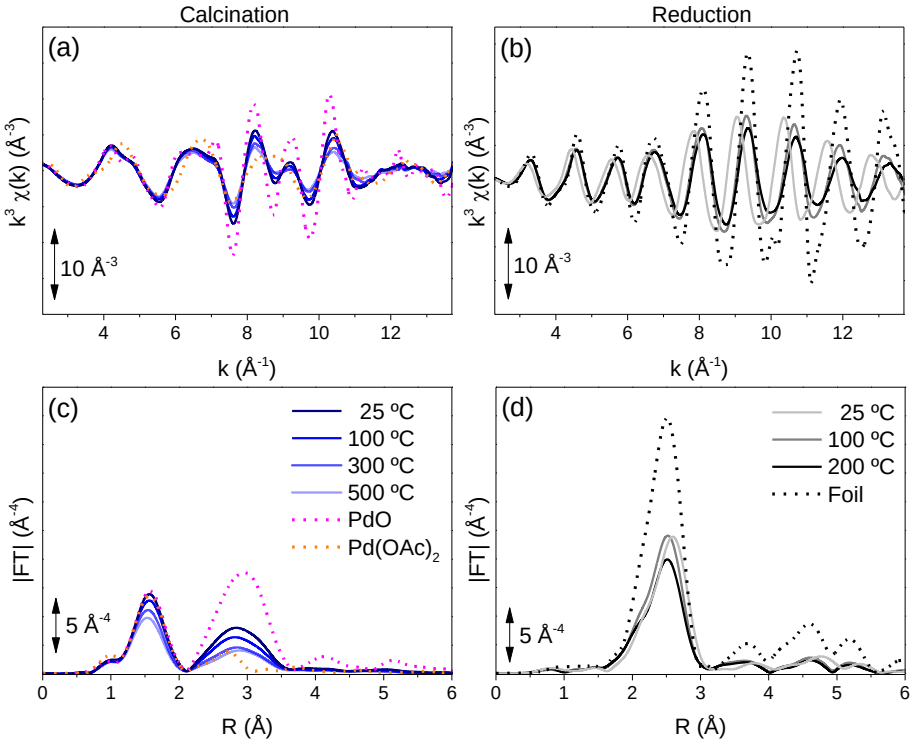

Figure 4.5. k^3-weighted phase-uncorrected χ(k) functions (top) and |FT| EXAFS spectra (bottom) of calcination (a,c) and reduction (b,d) process of PdAl-Ac.

The big difference in the intensity of foil oscillations reinforces the differences already observed in XANES spectra. However, the increasing of Debye-Waller factor with temperature should be mentioned when the intensity of the oscillations is discussed, which strongly affects these features.[47]

The k^3-weighted EXAFS data were Fourier transformed and the results are expressed in **Figure 4.5c-d**. FT spectra of catalyst during calcination (**Figure 4.5c)** present essentially two peaks. The first one between 1-2 Å (not corrected in phase), related to the contribution Pd-O from the PdO phase and the second one falling between 2-3.5 Å is attributed to Pd-Pd contribution, not attributed to Pd metal formation, but to the higher coordination shells of PdO. The impact of Debye-Waller is well visualized in this case, being the spectrum obtained at 500 ºC flattened 2.1 $Å^{-4}$ respected to the spectrum obtained at room temperature. Also, the difference in the second coordination shell of $Pd(OAc)_2$ respect to the sample and PdO is seen, which, one more time, suggest the absence (with the technique limitation) of acetate in this sample. In the reduction step, a difference of 0.1 Å in distance between the sample at 200 ºC under H_2 flux and cooled down to 25 ºC after reduction can be stated, due the PdH_x formation. Only one peak between 2-3 Å is present in all spectra, related to Pd-Pd distance of Pd metal. The nanoparticles are less ordered than the foil, because of the absence of peaks at high R-range, due to Pd second, third and fourth shells. However, this behavior is not rare and has been well discussed in literature for nanoparticles.[232]

The normalized XANES spectra collected during the activation process of PdAl-Cl catalyst are represented in **Figure 4.6** and compared to those of bulk $PdCl_2$, PdO and Pd foil.

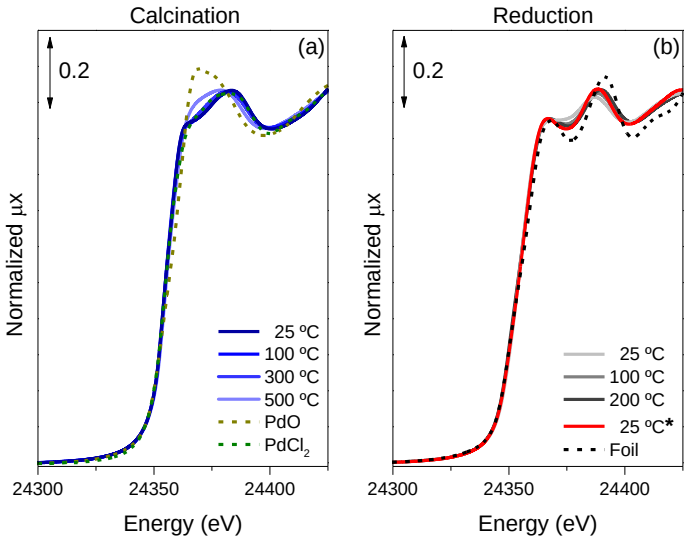

Figure 4.6. Normalized XANES spectra of PdAl-Cl during calcination in O_2 (a) and reduction in H_2 (b).

It is possible to observe a different behavior for this catalyst respect to the first one (PdAl-Ac). The spectrum of sample at beginning of calcination is different from PdO and closely attributed to $PdCl_2$, suggesting that $PdCl_2$ is not decomposed like $Pd(OAc)_2$ during impregnation/drying step of catalyst preparation. During calcination, an evolution in the XANES spectra (**Figure 4A.1**) from that typical of $PdCl_2$ at 25 ºC to an intermediate (possibly PdO_xCl_y[233-234] mixed phase) spectrum that does not resembles PdO at the end of thermal treatment is observed. Two main isosbestic points (A and B) positioned at 24363 and 24381 eV, respectively, can be seen. It is well-known that $PdCl_2$ is difficult to decompose (see TGA

analysis in **Figure 4A.2** in Appendix),[235] which makes it a complicated candidate in catalyst preparation when the final phase needs to be surface clean (without rests of precursor). As both $PdCl_2$ and PdO have the absorption edge at same position, no changes in this feature could be observed. However, during the reduction step it is possible to see that already at room temperature, the spectrum resembles to the spectrum of metal foil (but with different intensities of the oscillations beyond the edge), with the edge positioned at 24350 eV. Also, an evolution of the marked feature in the spectra during the reduction can be noted. The spectrum of the sample after reduction (cooled down to room temperature) presents the same oscillations of metal foil, but slightly displaced (3 eV), related to the formation of PdH_x. The displacement is also observed in the beginning of reduction (5 eV), where the temperature is low and the insertion of H in the Pd cell parameter is favored. When the temperature is increased (200 ºC), the PdH_x is no longer stable and consequently is decomposed. This behavior is better visualized in the EXAFS oscillations (k-space - light gray and red curves) of **Figure 4.7**. It is noticed in EXAFS signal of initial sample that its oscillations resemble the oscillations of $PdCl_2$ (**Figure 4.7a**), confirming the presence of the chloride precursor, as observed in normalized XANES spectrum. During the process of calcination the oscillations become flattened due the thermal effect on these features and no oscillations similar to PdO could

be observed. However, even with a little shift of oscillations to higher k-values, the features still very similar to $PdCl_2$, reinforcing the difficult decomposition of $PdCl_2$.

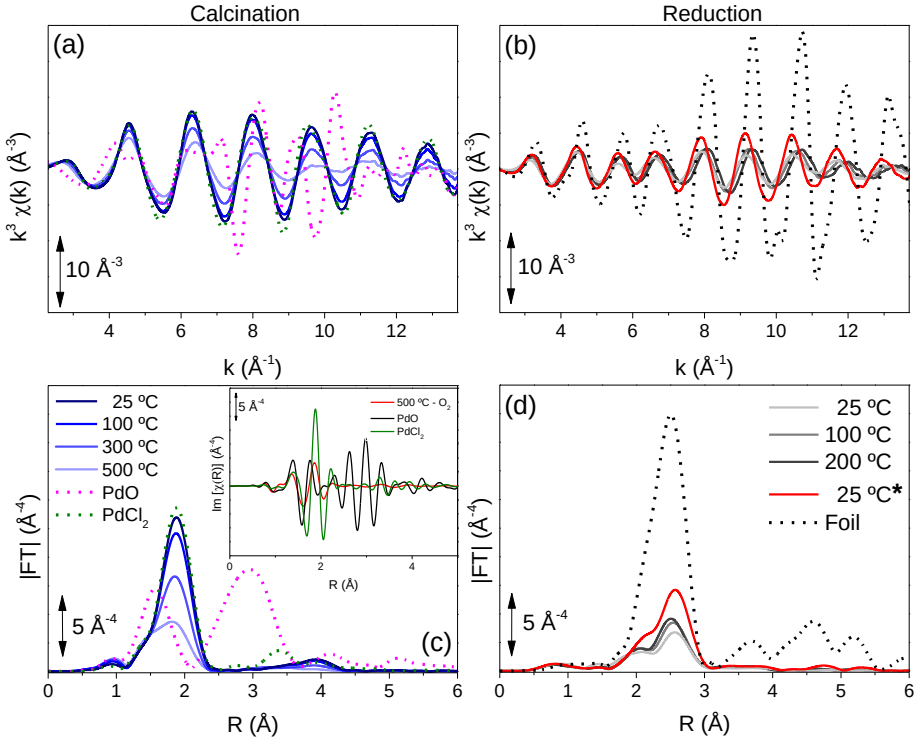

Figure 4.7. k^3-weighted phase-uncorrected χ(k) functions (top) and |FT| EXAFS spectra (bottom) of calcination (a,c) and reduction (b,d) process of PdAl-Cl.

The calcined catalyst has been submitted to reduction process with H_2, which lead to a reduction of Pd^{2+} to Pd^0, as discussed above. The EXAFS signal (**Figure 4.7b**) changed dramatically respect to as-prepared and/or calcined material,

being similar to metal foil, as expected in the final of reduction process. The intensity of oscillations of the material after reduction at 25 ºC is approximately 5 $Å^{-3}$, when the metal foil present oscillations close to 20 $Å^{-3}$, indicating that formed Pd species are not bulk. The already discussed formation and decomposition of Pd hydride can also be visualized in this case.

The EXAFS signal has been Fourier transformed from k-space to r-space and the results are represented in **Figure 4.7(c-d)**. The sample presents essentially one peak in FT during all calcination process, attributed to the contribution Pd-Cl. With increasing temperature, the peak becomes flattened and starts to shift to the left. This shift is due to Pd-O distance in PdO (2.0 Å) that is shorter than Pd-Cl distance in $PdCl_2$ (2.3 Å), being this displacement another indicative of formation a mixed PdO_xCl_y compound. The use of features (maxima and minima) of imaginary part of |FT| to obtain subtle information about metal systems is already known through literature.[236] In order to find the proportion of PdO and $PdCl_2$ present in the catalyst at the end of calcination we have used the position of the feature *a* present in the imaginary parts of |FT| of spectra collected during calcination (inset of **Figure 4.8**) as fingerprint for PdO fraction (*b* value) and the results are expressed in **Table 4.3**. At 25 ºC, the feature *a* lies at 1.684 Å, closely related to the position obtained for $PdCl_2$ (1.696 Å) and as the temperature increases the position of *a* shifts to lower R (related to higher PdO

fraction) values until reaching 1.608 Å at 500 ºC, giving rise to the formation of a $PdO_{0.75}Cl_{0.25}$ compound.

In the reduction process, a peak between 2-3 Å related to Pd-Pd contribution of formed metal nanoparticle and a significant difference in intensity attributed to the size of formed Pd nanoparticle respect to Pd foil are noticed. However, a little shoulder can be visualized in the left side of the main peak, being this shoulder a vestige of Cl attached to the Pd nanoparticles, which cannot be visualized in XANES or in k-space. The presence of this shoulder reinforces the difficult to remove Cl traces from the sample, even after calcination at 500 ºC and reduction at 200 ºC. It is well-known that Cl vestiges in nanoparticles can act as poisoner in some catalytic reactions, which turns the utilization of $PdCl_2$ a drawback in catalyst preparation for determined applications.[9, 212]

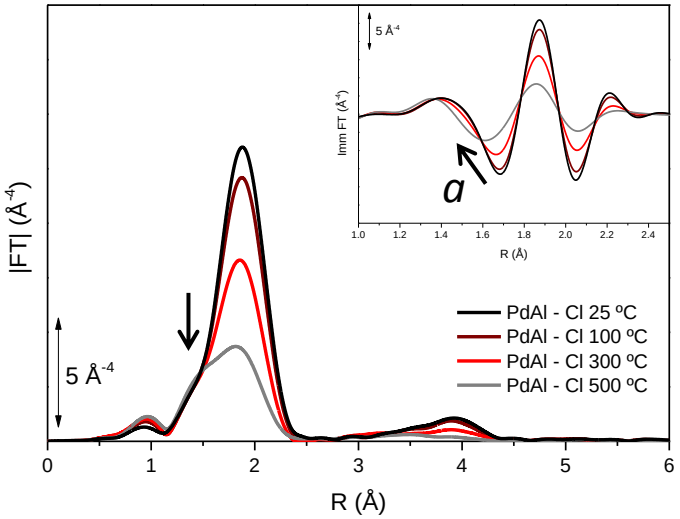

Figure 4.8. |FT| of the k^3-weighted χ(k) functions of PdAl-Cl sample during calcination. The inset shows the imaginary parts of the FT of the k^3-weighted χ(k) functions of the sample during calcination.

Table 4.3. Correlation between the position of feature *a* in the imaginary parts of the FT of the k^3-weighted χ(k) functions and the fraction of PdO (*b*) in the PdAl-Cl sample at different steps of calcination.

Sample	T (ºC)	*a* Position (Å)	*PdO* Fraction (%)[a]
PdO	-	1.580	1
$PdCl_2$	-	1.696	0
PdAl-Cl	25	1.684	0.10
	100	1.680	0.13
	300	1.667	0.25
	500	1.608	0.75

[a]Calculated according PdO fraction = (1.696-a)/-0.116

The normalized XANES spectra collected during the activation process of PdAl-NO_3 catalyst are represented in **Figure 4.9** and compare to those of bulk $Pd(NO_3)_2$ and PdO

used as references for Pd^{2+} and Pd foil, used as reference for Pd^{0} species.

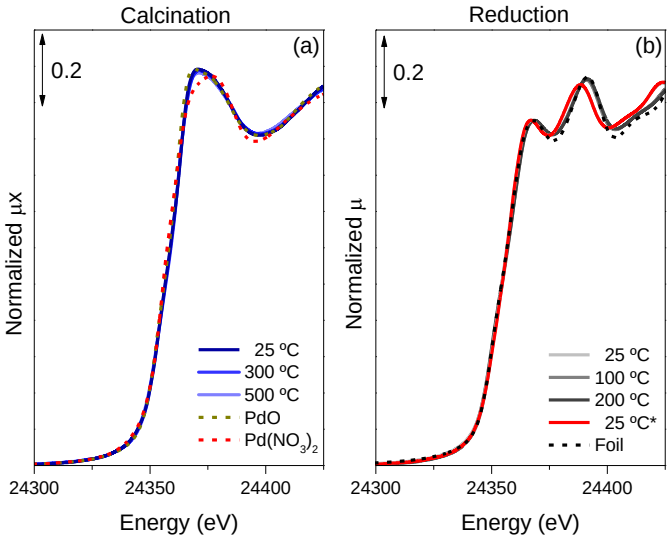

Figure 4.9. Normalized XANES spectra of PdAl-NO_3 during calcination in O_2 (a) and reduction in H_2 (b).

This catalyst present XANES spectrum different from $Pd(NO_3)_2$ and exactly equal to PdO even at RT due to the easily decomposition of $Pd(NO_3)_2$ at low temperature (see TGA analysis in Appendix) and consequently formation of oxide phase. The position of the edge (24354 eV – related to Pd^{2+}) is maintained constant during whole calcination process without changes in XANES oscillations. Changing the gas atmosphere to H_2, immediately reduction is observed, although spectrum is slightly different respect to foil at 25 ºC. As already reported for

above mentioned catalysts, shift in oscillations to the left due formation of PdH_x can be observed after cool the sample down in H_2 flow, which cannot be observed at higher temperatures due hydride decomposition. The nanosized nature of nanoparticle can be noticed by intensity of the oscillations, which are crushed in relation to foil spectrum.

The EXAFS signals attributed to calcination/reduction process of sample PdAl-NO_3 are shown in **Figure 4.10**. In the beginning of calcination step, the presence of oscillations referent to PdO instead $Pd(NO_3)_2$ as already explained above in XANES discussion are visible. Here, differences in intensity of oscillations are nicely visible and reinforce the nanosize of formed species during activation of catalyst. In the reduction process the changes in intensity could be better seen respect to normalized XANES, the alteration respect to the formation of palladium hydride is explicit, as well as its decomposition. The big difference in the intensity of foil oscillations reinforce the differences already observed in XANES spectra. However, the increasing of Debye-Waller factor with temperature should be mentioned when the intensity of the oscillations is discussed, which strongly affects these features. The FT spectra (**Figure 4.10**) of catalyst during calcination present two peaks: the first one between 1-2 Å, related to the contribution Pd-O from the PdO phase and the second one falling between 2-3.5 Å is

attributed to Pd-Pd contribution, not attributed to Pd metal formation, but the second coordination shell of PdO.

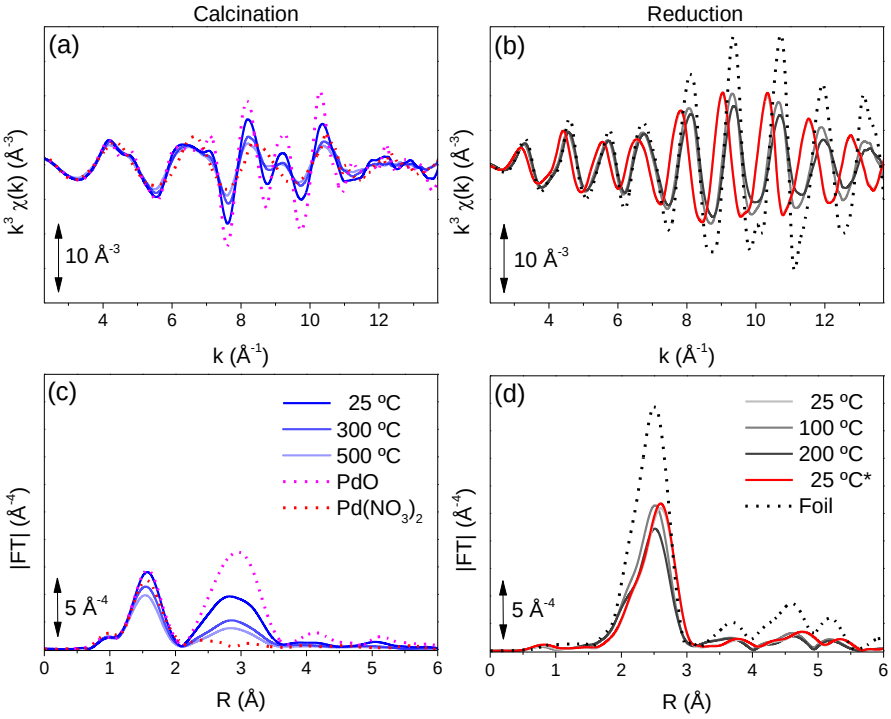

Figure 4.10. k^3-weighted phase-uncorrected χ(k) functions (top) and |FT| EXAFS spectra (bottom) of calcination (a,c) and reduction (b,d) process of PdAl-NO_3.

The impact of Debye-Waller is well visualized in this case, being the spectrum obtained at 500 ºC flattened respected to the spectrum obtained at room temperature. Also, the difference in the second coordination shell of $Pd(NO_3)_2$ respect to the sample and PdO is noticed. In the reduction step, it can be

seen the difference in phase due the PdH_x formation/decomposition. Only one peak between 2-3 Å is present in all spectra, related to Pd-Pd distance in Pd metal. The nanoparticles seem to be less ordered than the palladium metal pattern, due the absence of the peaks at high R-range.

From this point, the catalysts based on Pd/C will be discussed. Owing the sensitivity of carbon to oxidation in O_2 atmosphere and temperature, the catalysts have been activated in one step using hydrogen up to 200 ºC. XANES spectra of PdC-Ac during reduction are plotted in **Figure 4.11.**

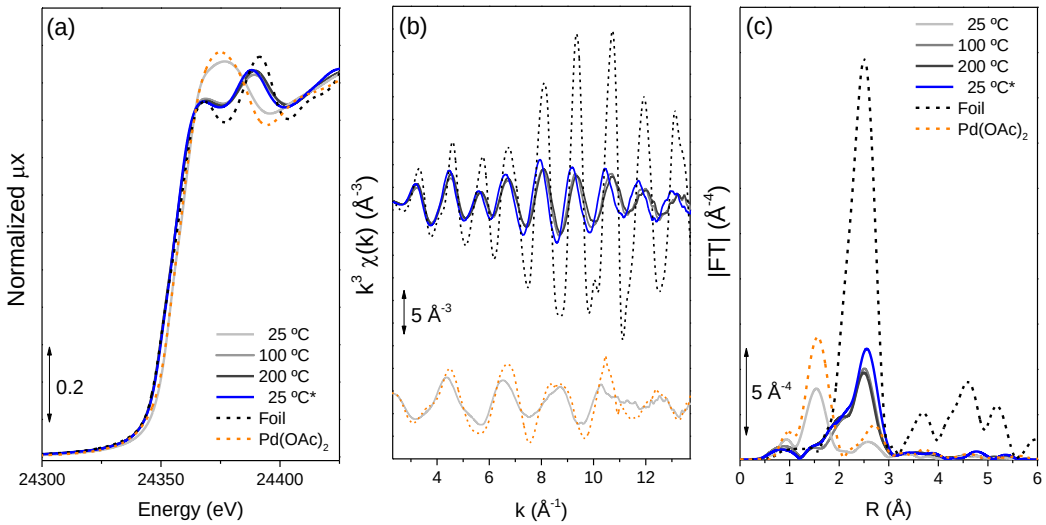

Figure 4.11. Normalized XANES spectra (a), k^3-weighted phase-uncorrected χ(k) functions (b) and |FT| of the k^3-weighted EXAFS spectra (c) of PdC-Ac during reduction in H_2.

XANES spectra of bulk $Pd(OAc)_2$ and Pd foil standards were used as fingerprint for Pd^{2+} and Pd^0, respectively. It is possible to observe that initial spectrum presents similar features compared to $Pd(OAc)_2$ (not resembling exactly to the standard), but since the first spectrum was collected already in H_2 (only for this sample), a reduction of Pd can occur, changing the features attributed to palladium acetate. At 100 ºC, the spectrum of catalyst shifts 4 eV to lower energy, indicating the reduction of Pd^{2+} to Pd^0, and the two features at 24367 and 24392 eV corresponding to Pd metal formation appear. The features of Pd^0 are maintained until the end of process, only being able to observe the formation of PdH_x when the sample is cooled down. Without the calcination step, at the end of reduction process, the catalyst presents oscillations of 10 $Å^{-3}$ at higher-k in $\chi(k)$ compared to 30 $Å^{-3}$ of foil, which supports the difference in size between the Pd standard (bulk) and the catalyst (nano). The formation of PdH_x results in a shift to the left of about 0.1 $Å^{-1}$ in spectrum of catalyst respect to foil. These differences observed in $\chi(k)$ can also be extrapolated to the peaks related to Pd-Pd contribution in |FT| where different intensities can be visualized comparing the sample after the treatment (blue line) and the pattern (6 $Å^{-4}$ for the sample and 22 $Å^{-4}$ for the Pd^0). It is worth noticing that is also possible to observe a tail between 1-2 Å in Fourier transform that cannot be observed in XANES and in EXAFS signal. This feature is probably attributed to the

presence of some Pd^{2+} bonded to ligands due to incomplete decomposition of precursor/reduction process. Once in this case there is no calcination step, the complete removal of precursor is more difficult; on the other hand, a sintering process from calcination process at high temperature is avoided.

XANES spectra of PdC-Cl during reduction are represented in **Figure 4.12.** XANES spectra of bulk $PdCl_2$ and Pd foil patterns were used as fingerprint for Pd^{2+} and Pd^0, respectively. Unlike the catalyst mentioned above, the initial spectrum of PdC-Cl was measured initially in O_2 atmosphere. It is noticed from XANES spectrum of PdC-Cl at room temperature in O_2 that features corresponding to $PdCl_2$ matches perfectly with features of studied sample, indicating that there is no modification of sample, as already reported for PdAl-Cl catalyst where $PdCl_2$ has been used as Pd precursor. The changes in atmosphere from O_2 to H_2 do not alter the profile of XANES at 25 ºC, only been visible changes when the temperature is increased to 100 ºC, where the catalyst presents similar features to palladium metal. From the beginning of activation to 200 ºC, the feature of $PdCl_2$ present between 24368 and 24384 eV is gradually suppressed and a shift in 4 eV in edge position is observed, confirming the reduction of Pd^{2+} to Pd^0.

The **Figure 4.12b** represent the $\chi(k)$ functions of PdC-Cl during activation. It can be seen that oscillations of impregnated sampled closely resemble those of $PdCl_2$ standard. On the other

hand, when the atmosphere is changed to H_2, the spectra no longer resemble the $PdCl_2$, only being possible to see one feature at approximately 6 $Å^{-1}$, indicating an almost complete change in Pd environment. From 100 ºC to the final spectrum (25 ºC after cooled the sample down – blue line) is possible to observe a huge difference in intensity of EXAFS signal respect to foil, indicating the nanosize of species formed. As in all cases presented so far, a displacement of blue spectrum to higher-k can be observed, which corresponds to the formation of palladium hydride.

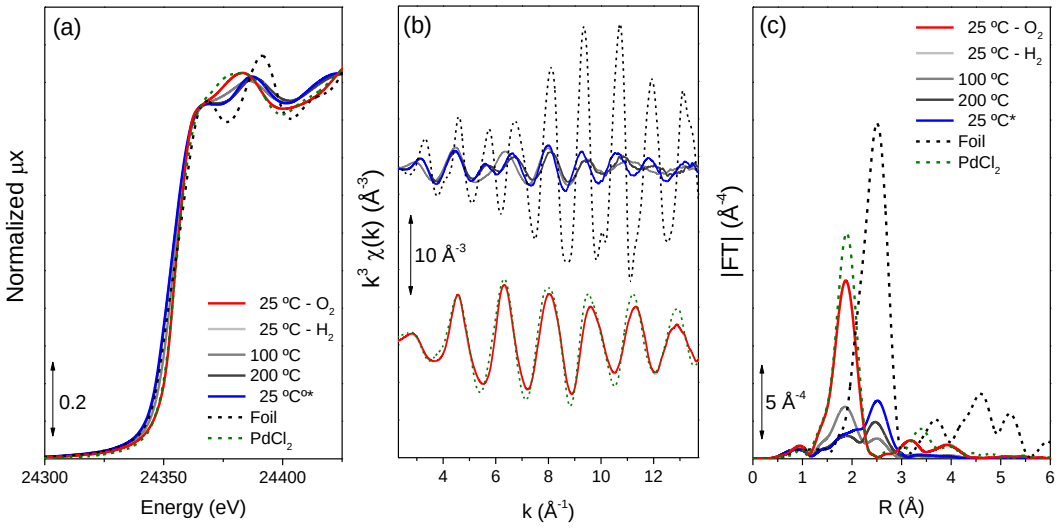

Figure 4.12. Normalized XANES spectra (a), k^3-weighted phase-uncorrected χ(k) functions (b) and |FT| of the k^3-weighted EXAFS spectra (c) of PdC-Cl during reduction in H_2.

The k^3-weighted EXAFS data were Fourier transformed and the results are expressed in **Figure 4.12c**. The initial sample measured at 25 ºC in O_2 present essentially one peak between 1-2.5 Å, related to contribution Pd-Cl (at 2.3 Å) and when the atmosphere is changed to H_2 and the temperature increased to 100 ºC, the intensity decrease considerably and another weak contribution appears between 2-3 Å, attributed to Pd-Pd contribution related to Pd nanoparticle formation.

However, increasing the temperature by 100 ºC and cooling the sample to room temperature (end of activation), the contribution of Pd-Cl is still present, which was already reported for the PdAl-Cl catalyst. Nevertheless, for the catalyst based on alumina, the sum of calcination plus reduction process is able to remove almost completely the precursor. Furthermore, is possible to observe in the moduli of |FT| the large difference in magnitude between the foil and nanoparticle formed in activated sample, indicating that nanodomains of Pd are formed in this sample. Also, comparing both supports (Al_2O_3 and C) impregnated with $PdCl_2$, once again is possible to conclude that calcination step is crucial in the size of Pd species formed, for instance, the nanoparticle supported on alumina present a magnitude of 7 $Å^{-4}$ compared to 3.8 $Å^{-4}$ related to nanoparticle supported on carbon.

XANES spectra of PdC-NO_3 during reduction are represented in **Figure 4.13**. The spectra of bulk $Pd(NO_3)_2$ and

Pd foil patterns were used as fingerprint for Pd^{2+} and Pd^{0}, respectively.

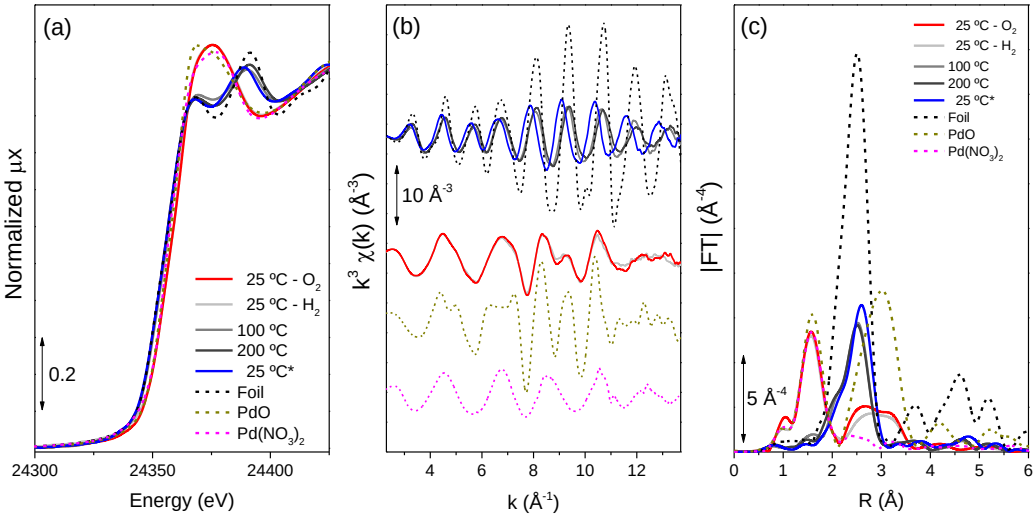

Figure 4.13. Normalized XANES spectra (a), k^3-weighted phase-uncorrected χ(k) functions (b) and |FT| of the k^3-weighted EXAFS spectra (c) of PdC-NO_3 during reduction in H_2.

Surprisingly, the initial sample measured in O_2 and H_2 present features between $Pd(NO_3)_2$ and PdO with edge position at 25354 eV, attributed to Pd in oxidation state 2+. A reduction of Pd^{2+} to Pd^{0} is immediately observed with increasing the temperature to 100 ºC by displacement in edge position from 25354 to 25350 eV and the spectrum resembles to the metal foil (but with different intensities of the oscillations beyond the edge). After the activation, the spectrum collected at room temperature presents flattened oscillations in comparison with

Pd foil, which is due to size effects of nanoparticle formed. Also, the PdH_x formation can be seen by the shift in spectrum to lower energy. The character of Pd species present in the sample just after impregnation can be better visualized in $\chi(k)$ EXAFS functions (**Figure 4.13b**). Comparing the samples measured in O_2 and H_2 at room temperature with their respective patterns, it can be seen that, in fact, the catalyst in initial state present contributions from PdO and $Pd(NO_3)_2$, being the two first waves in EXAFS signal very similar to $Pd(NO_3)_2$. Conversely, at higher-k values (beyond 7 $Å^{-1}$), the features are very similar to PdO, giving indicia that contributions of Pd species present in the beginning are coming from both standards. The EXAFS signals were Fourier transformed and moduli are represented in **Figure 4.13c**. It can be seen in moduli of FT that initial sample possess mainly two peaks, the first one centered at 1.5 Å, regarding to Pd bonded to O (2.0 Å), and a second broad contribution between 2-3.5 Å, related to higher shells of PdO. It is important to note that, even XANES and $\chi(k)$ functions showing a mixed contribution of PdO and $Pd(NO_3)_2$ for initial sample, the features in |FT| are much more similar to PdO than $Pd(NO_3)_2$. Except for the peak at 1.5 Å (not corrected in phase) of nitrate precursor, the higher shells are not visible or are covered by the contribution of PdO. After increasing the temperature to 200 ºC and cool the sample down, just one peak attributed to Pd-Pd bond between 2-3 Å is visible; this confirms

the reduction of sample. The nanosized character of Pd species and formation of PdH_x are also observed in this case.

The quantitative results derived from EXAFS data analysis of as-prepared Pd catalysts are shown in **Table 4.4**. Most catalysts present the expected average coordination number of approximately 4, with the exception of PdAl-Ac, measured in presence of H_2, which presented an average coordination number of 1.9, corresponding to the loss of ligands due the reduction step ($Pd(OAc)_2 \rightarrow Pd^0$). For this catalyst, a higher Debye-Waller factor (0.0052 $Å^2$) has been observed in comparison with other samples, possibly due to a disorder effect with respect to decomposition process of precursor. Except for PdAl-Ac catalyst, all catalysts in their as-prepared state presented main parameters in accordance with crystallographic data of respective studied precursors.

Table 4.4. Summary of optimized parameters by fitting EXAFS data of as-prepared catalysts at 25 ºC in H_2[a]

Sample	CN	Path	R (Å)	σ^2 ($Å^2$)	ΔE_0 (eV)	r-factor
PdAl-Ac	4.0(5)	Pd-O	2.028(6)	0.0033(8)	1.5(1.8)	0.0077
PdAl-Cl[b]	3.7(1)	Pd-Cl	2.311(2)	0.0034(2)	4.3(0.5)	0.0009
PdAl-NO_3	4.2(5)	Pd-O	2.030(6)	0.0034(8)	0.2(1.7)	0.0068
PdC-Ac	1.9(5)	Pd-O	2.021(11)	0.0052(15)	2.1(2.7)	0.0144
PdC-Cl[b]	3.6(1)	Pd-Cl	2.308(2)	0.0040(2)	4.3(0.4)	0.0007
PdC-NO_3	3.9(8)	Pd-O	2.023(11)	0.0039(15)	2.1(2.9)	0.0185

[a]The fits were performed on the first coordination shell (ΔR = 1.0-2.0 Å) over FT of the k^3-weighted $\chi(k)$ functions performed in the Δk = 2.3-13.7 $Å^{-1}$ interval, resulting into a number of independent parameters of $2\Delta R\Delta k/\pi$=7.0. [b]ΔR = 1.4-2.4 Å.

The quantitative results derived from EXAFS data analysis of Pd catalysts during reduction at 200 ºC are shown in

Table 4.5. The results obtained fitting the spectra at 200 ºC have been used to obtain the average particle size due the absence of PdH_x, which lead to an increase in Pd-Pd distance and consequently affect the particle size calculation. The average coordination number obtained for the studied catalysts at 200 ºC presented small deviation respect to the spectra measured after reduction (25 ºC) and varied significantly according to the precursor. As already discussed above, the difficult decomposition of $PdCl_2$ generates catalysts with significantly low average coordination number irrespective to the studied support (4.7 for Pd/Al_2O_3 and 2.3 for Pd/C). These obtained coordination numbers point to the formation of aggregated Pd species using $PdCl_2$ as precursor. It is worth noticing that despite the presence of remaining Pd-Cl contribution visible in |FT|, it is challenging to fit these contributions since we do not have a safe model. On the other hand, using $Pd(NO_3)_2$ the catalysts presented higher number of neighbors (12 for Pd/Al_2O_3 and 7.6 for Pd/C), achieving bulk size of formed Pd species in the case of Pd/Al_2O_3. Among the examined precursors, the nitrated compound produces Pd nanoparticles with higher CN for Pd-Pd contribution and consequently bigger nanoparticles. The catalyst PdAl-Ac similarly presented considerable Pd-Pd coordination number (CN = 10.7), which can also be considered as bulk. As expected, the Pd-Pd distance for the investigated catalysts is shorter than in Pd foil (R_{Pd-Pd} = 2.74 Å), equivalent to quantum

size effects. In the case of PdC-Cl, the Pd-Pd bond is even shorter than the other catalysts due to substantially small size of Pd aggregates.

The r-factors explicit the quality of adjusted parameters and the catalysts prepared with $PdCl_2$ showed the higher error among their data set, for instance, 0.0746 for PdC-Cl among Pd/C samples, and 0.0198 for PdAl-Cl among Pd/Al_2O_3 samples. This can be explained by the unfitted "tail" visible in |FT| related to the presence remaining ligands of $PdCl_2$ precursor, which is also visible in PdC-Ac. The other catalysts presented very small errors, confirming the high quality of the fit. The fits in both R-space and q-space are included in the appendix (**Figure 4A.3** and **Figure 4A.4**, respectively).

Table 4.5. Summary of optimized parameters by fitting EXAFS data of catalysts at 200 ºC in H_2[a]

Sample	CN	Path	R (Å)	σ^2 (Å^2)	ΔE_0 (eV)	r-factor
PdAl-Ac	10.7(4)		2.731(2)			0.0024
PdAl-Cl	4.7(2)	Pd-Pd	2.735(3)			0.0198
PdAl-NO_3	12.0(4)		2.733(2)			0.0026
PdC-Ac	4.9(3)		2.733(3)	0.0095(2)	2.4(4)	0.0123
PdC-Cl[b]	2.3(2)	Pd-Pd	2.726(8)			0.0746
PdC-NO_3	7.6(4)		2.729(4)			0.0007

[a]A simultaneous fit of the spectra was adopted, fixing the σ^2 and ΔE_0 values; the fits were performed on the first coordination shell (ΔR = 2.2-3.0 Å) over FT of the $k^1k^2k^3$-weighted $\chi(k)$ functions performed in the Δk = 2.3-13.7 Å^{-1} interval, resulting into a number of independent parameters of $2\Delta R\Delta k/\pi$=38.8. [b]ΔR = 1.4-3.0 Å.

The quantitative results derived from EXAFS data analysis of Pd catalysts after reduction at 200 ºC and cooled to

room temperature under H_2 flow (state in which the catalysts will be used) are shown in **Table 4.6**.

Table 4.6. Summary of optimized parameters by fitting EXAFS data of catalysts after reduction in H_2 at 25 ºC[a]

Sample	CN	Path	R (Å)	σ^2 (Å^2)	ΔE_0 (eV)	r-factor
PdAl-Ac	-		-			-
PdAl-Cl	6.4(3)	Pd-Pd	2.792(3)			0.0027
PdAl-NO_3	12.0(6)		2.823(3)	0.0082(3)	2.9(5)	0.0041
PdC-Ac	5.6(3)		2.783(3)			0.0126
PdC-Cl[b]	3.1(2)	Pd-Pd	2.775(6)			0.0559
PdC-NO_3	7.6(4)		2.806(4)			0.0029

[a]A simultaneous fit of the spectra was adopted, fixing the σ^2 and ΔE_0 values; the fits were performed on the first coordination shell (ΔR = 2.2-3.0 Å) over FT of the $k^1k^2k^3$-weighted $\chi(k)$ functions performed in the Δk = 2.3-13.7 Å^{-1} interval, resulting into a number of independent parameters of $2\Delta R\Delta k/\pi$=33.3. [b]ΔR = 1.4-3.0 Å.

With exception of Pd-Pd distance, there are only small differences between the samples after reduction and during reduction at 200 ºC, the average coordination numbers and the r-factors slightly deviate from the spectra measured at 200 ºC. The biggest differences are attributed to Debye-Waller factor (which in this case is smaller at room temperature than at 200 ºC due to decrease in temperature) and Pd-Pd distances. With the decrease in temperature, the distances Pd-Pd increase due to the insertion of H in Pd lattice in the formation of PdH_x. However, the distances seem to be different for each catalyst, and it is possible to correlate the different Pd-Pd distances to the different coordinate numbers obtained, thus the shorter is the distance, the smaller the coordination number is. This behavior can be explained by the fact that when the particle is bigger, there are a higher number of interior octahedral sites available for hydrogen

incorporation. Frenkel et al.[46] has been proposed a method for the determination of Pd cluster size from H/Pd ratio in nm-size metal particles. However, we decided to adopt another methodology to evaluate the size of particles since we do not have the spectrum of PdAl-Ac after reduction.

For a better visualization and comparison, the moduli of Fourier transform of catalysts during reduction in H_2 at 200 ºC are gathered in **Figure 4.14**.

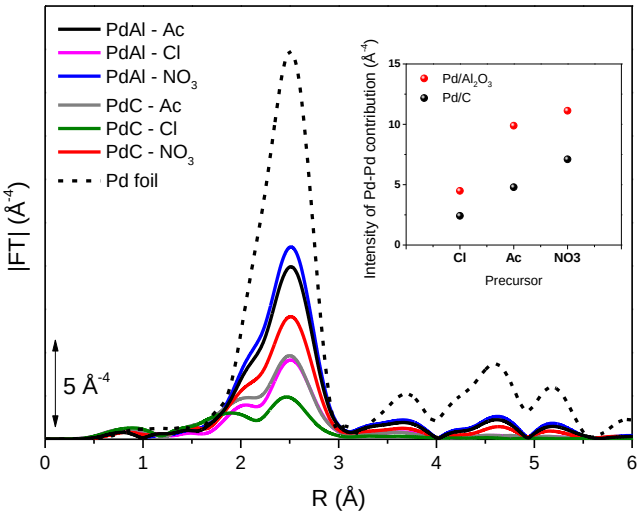

Figure 4.14. |FT| of the k^3-weighted χ(k) functions of catalysts during reduction in H_2 at 200 ºC. The inset shows the plot of intensity of |FT| versus type of Pd precursor in Pd/Al_2O_3 and Pd/C catalysts during reduction in H_2 at 200 ºC.

A clear trend between Pd precursor and intensity of Pd-Pd contribution in |FT| is observed for both supports, with larger nanoparticles observed for the catalysts based on Al_2O_3 in

comparison with carbon (better seen on inset of **Figure 4.14**). Therefore, the average size of nanoparticles among all catalysts is as follows: PdC-Cl < PdAl-Cl ≈ PdC-Ac < PdC-NO_3 < PdAl-Ac < PdAl-NO_3. On the other hand, comparing the three precursors, both classes of catalysts (Pd/Al_2O_3 and Pd/C) behave equally, i.e., the $PdCl_2$ generates smaller nanoparticles than $Pd(OAc)_2$, which in turn generates smaller nanoparticles than $Pd(NO_3)_2$.

Since studies comparing particle size distribution by multitechnique approaches (using EXAFS as a way to obtain metal particle sizes) are reported in literature,[11] it is also important to perform other characterization methods (e.g. TEM and CO chemisorption) in order to validate EXAFS results. With this purpose, CO chemisorption analyses have been performed on Pd-based catalysts studied by EXAFS and results are reported in **Table 4.7** compared with CN and corresponding average particle sizes obtained by EXAFS calculated according the method reported in literature.[11, 218]

Table 4.7. Average particle sizes obtained by EXAFS and metallic surface area obtained by CO chemisorption of Pd-based catalysts after H_2 reduction.

Sample	CO chemisorption	EXAFS[a]		
	Metallic surface area (m^2/g)	CN		<d> (Å)
PdAl-Ac	3.2	10.7	→	40
PdAl-Cl	9.4	4.7	→	9
PdAl-NO_3	2.4	12.0	→	126
PdC-Ac	3.5	4.9	→	9.2
PdC-Cl	15.9	2.3	→	6.9
PdC-NO_3	3.7	7.6	→	13.8

[a]Values obtained from spectra measured at 200 ºC during reduction in H_2

Small particle diameter corresponds to low values for CN and the opposite in case of big nanoparticles. On the other hand, higher metallic surface area is correlated with small particle size whereas for larger nanoparticles low surface area is expected. Comparing the data reported in **Table 4.7** it can be seen that the trend observed by EXAFS is evidenced also by CO chemisorption.

Unfortunately, in this study it was not possible to perform a reliable quantitative comparison across EXAFS, chemisorption and TEM as reported in literature converting metal surface area in particle size. The general issue is that the samples described in this chapter undergone to the same condition during XAS measurements in terms of temperature, gas feed, timing of each reduction step, and sample environment. In this way we were able to collect a homogeneous and consistent data set for our comparison. In case of CO chemisorption and TEM it was not possible to reproduce the final experimental condition of XAS experiment since thermal treatment was not exactly the same since temperature was not increased by stepping as during XAS experiments. Additionally, the XAS cells for sample treatments has not the same design than the reactor used in preparation of TEM and chemisorption samples, resulting in different conditions like temperature, dead volume, and contact time sample-gas. All these parameters

could affect particles size distribution making impossible a direct and reliable comparison.

In addition, we observed by TEM (see **Figure 4.15**) that Pd particles often result into a well-ordered core surrounded by a disordered external shell. According to this observation some consequences can be pointed out: (i) EXAFS results could be undergone to underestimation of CN and so particles size of nanoparticle population; (ii) disordered metal surface can affect the absorption of CO on nanoparticles and so the surface area calculated; (iii) the geometrical model adopted to correlate CN versus particle size assumes perfect cluster with cuboctahedra shape: moving from this hypothesis particle size determination can be affected.

A few TEM images of Pd/Al_2O_3 catalysts are included in **Figure 4.15** to demonstrate the presence of Pd nanoparticles even with the high metal loading used for catalyst preparation (7 wt.%). The presence of larger nanoparticles in the $PdAl\text{-}NO_3$ catalyst (bulk Pd nanoparticles), is the evident explanation for the higher CN for Pd-Pd contribution and higher value of chemisorbed CO among the whole set of samples.

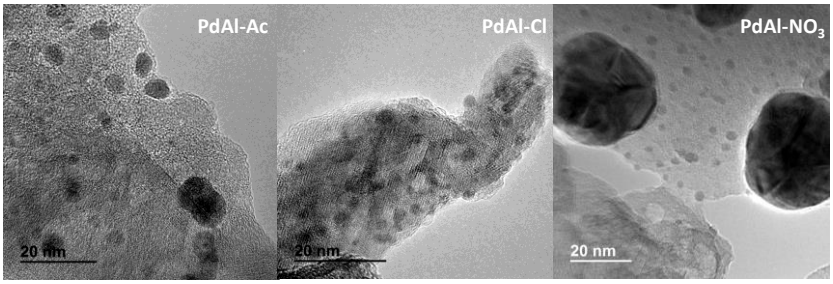

Figure 4.15. TEM images of Pd nanoparticles formed upon reduction in H_2 of Pd/Al_2O_3 catalyst.

4.2 Conclusions

In this work we followed by *in situ* XAS the activation process of 7 wt.% Pd-based catalysts (Pd supported on Al_2O_3 and activated carbon) using three different metal precursors: $Pd(OAc)_2$, $PdCl_2$ and $Pd(NO_3)_2$. We find that the nature of Pd precursor and activation procedure (e.g. calcination process) influence metal dispersion and average particle size. First, the easiest decomposition of $Pd(NO_3)_2$ respect to other precursors always gives rise to PdO formation, even during the impregnation step, and consequently larger nanoparticles are formed at the end of activation process. Similarly, $Pd(OAc)_2$ follows a very similar activation path through PdO species, but its formation needs slightly higher temperatures. Finally, the activation of the catalysts in which $PdCl_2$ was used as precursor goes by a different way. Al_2O_3-based catalysts pass through an intermediate phase ($PdO_{0.75}Cl_{0.25}$) during calcination in air, which is decomposed during reduction. On the other hand, Cl-

species were identified in the carbon-based sample even after reduction. Moreover, according to the decrease in EXAFS amplitude, we found that $PdCl_2$ generates smaller nanoparticles than $Pd(OAc)_2$, which in turn generates smaller nanoparticles than $Pd(NO_3)_2$, independent of used support. The use of *in situ* XAS has allowed tracking the activation processes of a series of Pd supported catalysts and could be useful for the selection of the right Pd precursor during synthesis of Pd based catalysts.

4.3 Appendix

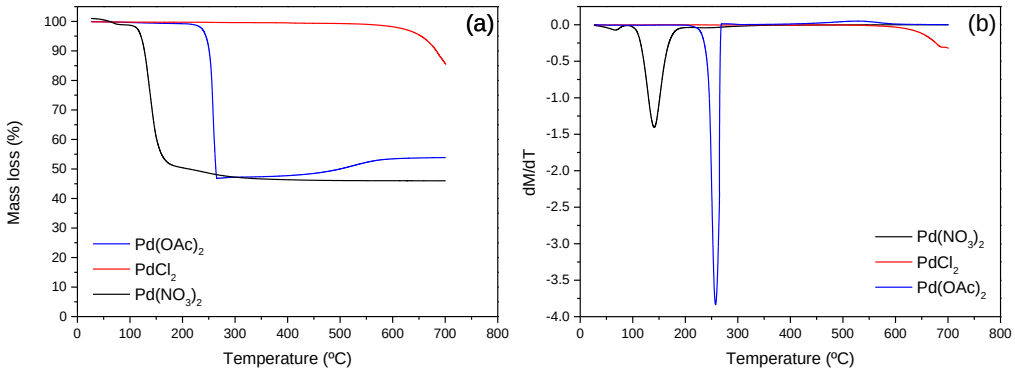

Figure 4A.1. Thermogravimetric analysis (a) and respective derivative (b) of $Pd(OAc)_2$, $PdCl_2$ and $Pd(NO_3)_2$ precursors.

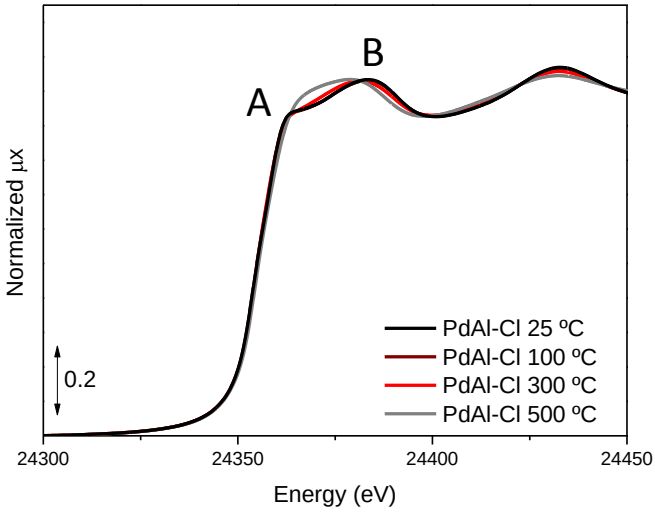

Figure 4A.2. Normalized XANES spectra of PdAl-Cl sample during calcination.

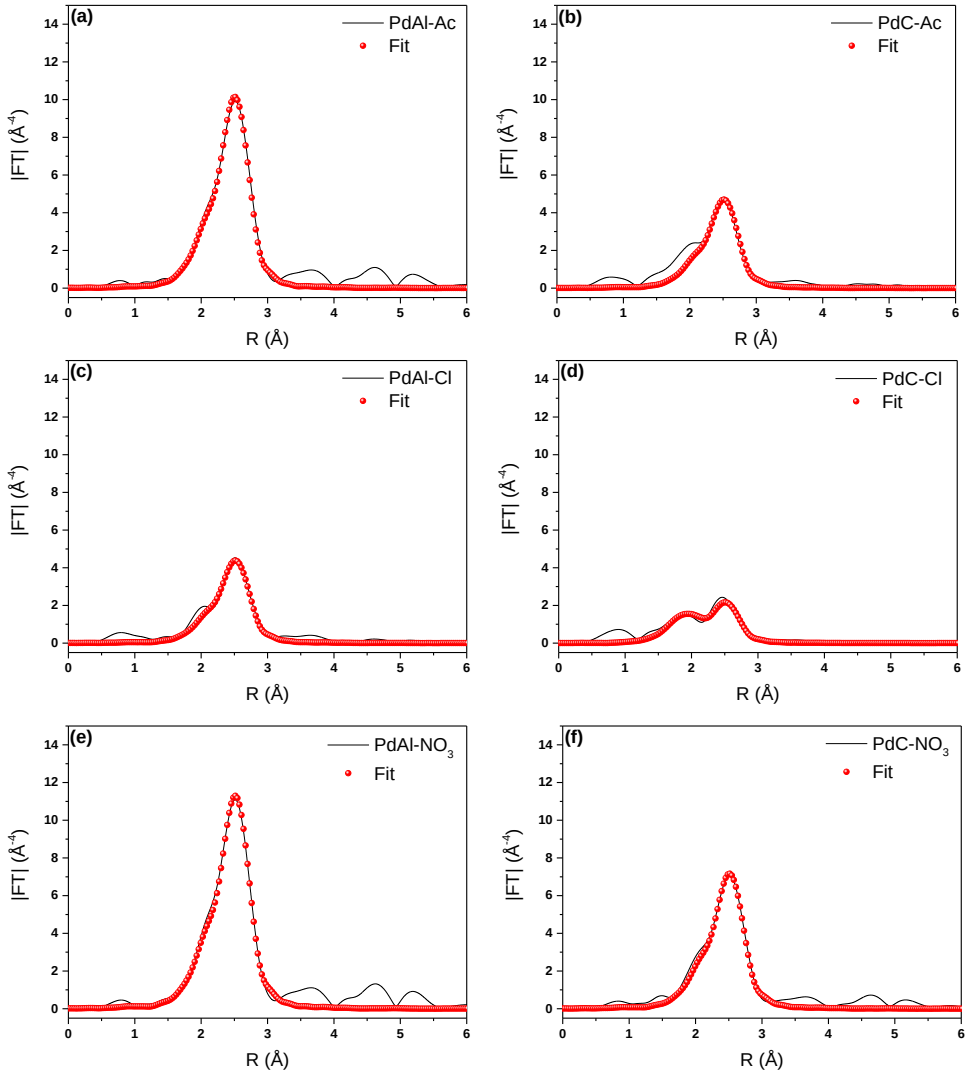

Figure 4A.3. |FT| of the k^3-weighted $\chi(k)$ functions of catalysts during reduction in H_2 at 200 ºC: (a) PdAl-Ac (b) PdC-Ac (c) PdAl-Cl (d) PdC-Cl (e) PdAl-NO_3 (f) PdC-NO_3.

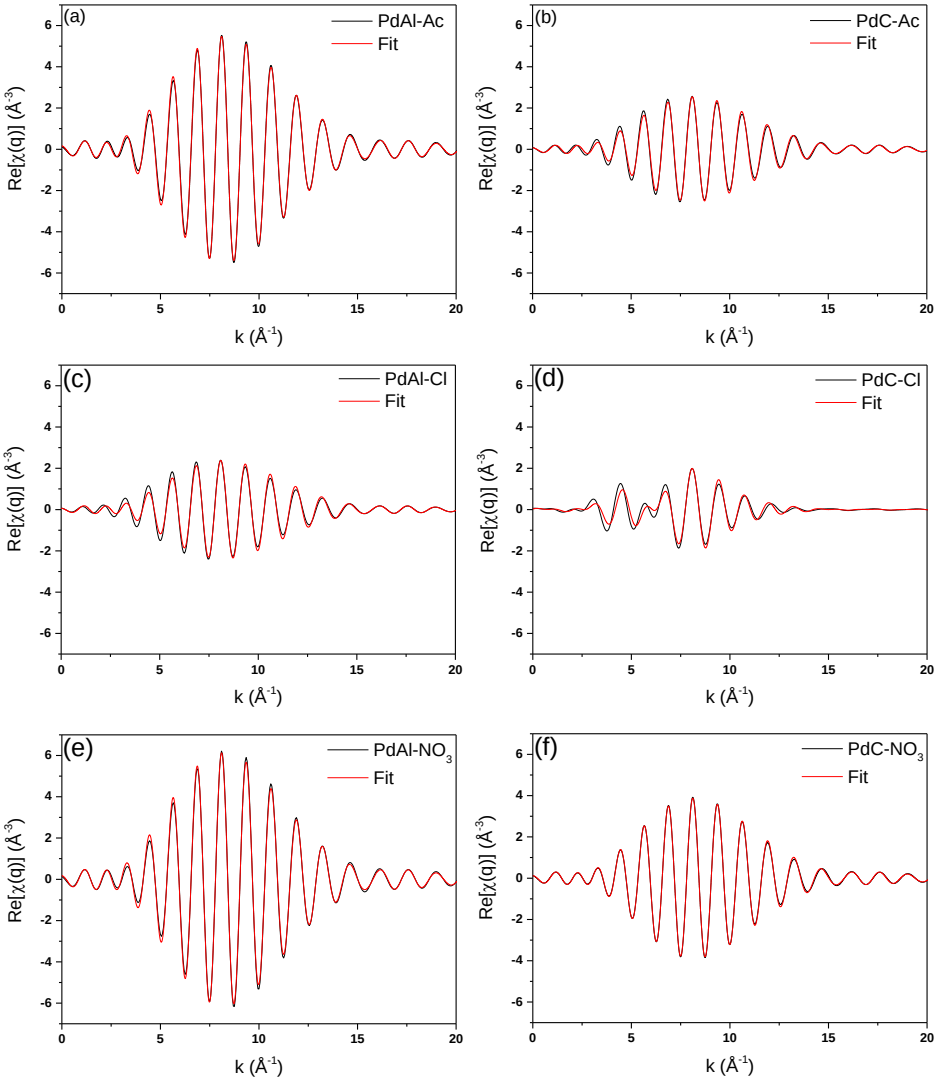

Figure 4A.4. k^3-weighted χ(q) functions (q-range = 2.2-3.0 Å) of Pd-based catalysts during reduction in H_2 at 200 ºC: (a) PdAl-Ac (b) PdC-Ac (c) PdAl-Cl (d) PdC-Cl (q-range = 1.4-3.0 Å) (e) PdAl-NO_3 (f) PdC-NO_3.

Chapter 5

Zeolite-driven Ag species during redox treatments and catalytic implications for SCO of NH_3

5.0 Introduction

Zeolites are microporous aluminosilicates, constituted by $[TO_4]$ tetrahedra (T = Si, Al, etc) that belong to the family of tectosilicates, and are highly interesting due to their multiple applications in industrial processes, mainly in separation and catalysis. The functional and catalytic properties of zeolites usually can be modulated either by the framework composition or by the presence of different extraframework cations located in the channels and cavities of zeolites.[237]

As discussed in the introduction section, XAS has been proven to be a very efficient tool for studying ion-exchanged zeolites. Among them, silver loaded zeolites have been studied as catalysts and in other applications (such as antimicrobial agents).[126, 238] Ag-exchanged zeolites are of particular interest because of the unusual properties of the Ag^+ cations.[239] Ag^+ is the only noble monopositive cation that forms mononuclear stable species in water. Thus, Ag^+ can be easily exchanged into zeolites from aqueous solution. The reversible oxidation-reduction of silver in zeolites provides an excellent model system for studying the mechanism of formation of noble metal clusters within zeolite channels and cavities.[240] Moreover, the use of zeolites as silver-hosts meets the requirements for obtaining clusters of noble metals at nanoscale. The size of zeolite-entrapped clusters is constrained along one or more dimensions. Such constraints usually render substantial changes

in the structural, physical, electronic, magnetic and also optical properties of the clusters. Furthermore, the zeolite cages provide practical means of preventing the cluster coalescence, because small metal clusters have a strong tendency to form larger particles (d > 10 nm) driven by surface energy minimization.[241] It would be expected that the zeolite porosity could favor the clustering of Ag species during thermal activation of Ag-zeolites, preventing the formation of large metal particles.

The formation and growth of clusters in some silver-containing zeolites (or zeotypes) have been studied under several conditions.[129, 151, 164, 242-245] However, the influence of zeolite properties (particularly, small-pore zeolites) on the formation of silver clusters has been poorly studied.[30, 246-249] Apart from typical activation treatments used to generate clusters and nanoparticles, the inverse path has also been reported, where silver cations are redispersed within zeolite extraframework positions once the nanoparticle is formed in a process involving thermal treatments in an oxidizing atmosphere.[30, 67, 128, 155] This approach has been also extended for other metal-containing zeolites[69] and is often used as a convenient procedure to regenerate the active metal center of catalysts.[65] Furthermore, reduction/reoxidation treatments are pivotal in the catalyst design, especially for those applied in certain reactions, such as selective catalytic oxidation of ammonia to N_2 (SCO-NH_3).

Ammonia (NH_3) is one of the key chemicals with worldwide massive industrial production around millions of tons per year. This fact is related to its extensive use in agriculture for the manufacturing of fertilizers, such as urea, anhydrous ammonium nitrate, etc.[250] It is estimated that 75% of ammonia release to atmosphere is connected with its use in agriculture while the other 25% are related with non-agriculture sources like biomass burning, fossil fuel combustion and emission from industrial processes.[250] Among several ways to control the ammonia emissions, SCO-NH_3 is one of the most promising technologies and it is often associated to selective catalytic reduction of NO_x (SCR-NO_x). The latter uses ammonia as reducing agent, which can be incompletely oxidized during SCR process. The oxygen containing waste gases after SCR process require no additional reactants for ammonia conversion. Low temperature (250-400 ºC) conversions of ammonia are highly desirable for use in power plants while the temperature of exhaust gases emitted by diesel engines can reach up to 600 ºC.

Recent works suggest the catalytic activity of Ag-based catalysts in selective catalytic oxidation of ammonia and their selectivity to N_2 depend on several parameters, such as the oxidation state of silver (e.g. Ag^+, Ag^0), the size of Ag^0 domains and the amount of metal used as catalyst.[251-252] According to this, controlling the silver oxidation state and size of species by appropriate selection of the support, which could modulate these

properties, combined with the adequate thermal treatment, is a key step during catalyst design.

In this chapter, we have comprehensively studied, by a multitechnique approach, the redox behavior of Ag-exchanged small-pore zeolites CHA and RHO and the catalytic consequences of differently-activated Ag-zeolites in SCO-NH_3 reaction. The influence of thermal treatments performed under different atmospheres (O_2, H_2 and He) on the silver clustering/aggregation was followed by *in situ* XAS and complementary characterized by *ex situ* techniques. The influence of framework structure, zeolite chemical composition, silver loading and nature of co-cations on the formation of silver species have been evaluated. To the best of our knowledge, it is the first time that the correlation between catalytic activity for SCO-NH_3 and type/size of silver species in Ag-loaded zeolites is addressed so far.

5.1 Results and Discussion

The results in this chapter can be divided into three parts. The first one is dedicated to the characterization of as-prepared zeolites, their Ag-exchanged and thermal-treated forms but characterized mainly by laboratory techniques. The second one is related to the *in situ* tracking of silver species by X-ray absorption spectroscopy during redox treatments with other laboratory techniques supporting the observed features detected

by XAS. Finally, the last part is dedicated to discuss how different (in terms of type and size) silver species formed on small-pore zeolites CHA and RHO can affect the catalytic results for selective catalytic oxidation of ammonia. Some results obtained for AgCHA (Si/Al = 4.5) will be included for comparison purposes, as this material has similar chemical composition than AgRHO. Additional samples as AgCHA (Si/Al = 4.5) will help in drawing the conclusions about the role of zeolite structure type on silver clustering and consequently on the catalytic performance for the SCO-NH_3.

5.1.1 Characterization of as-made and ex situ thermally-activated Ag-exchanged zeolites

The as-synthesized zeolites were characterized initially by XRD to confirm the success of the syntheses and the results are shown in **Figure 5.1**.

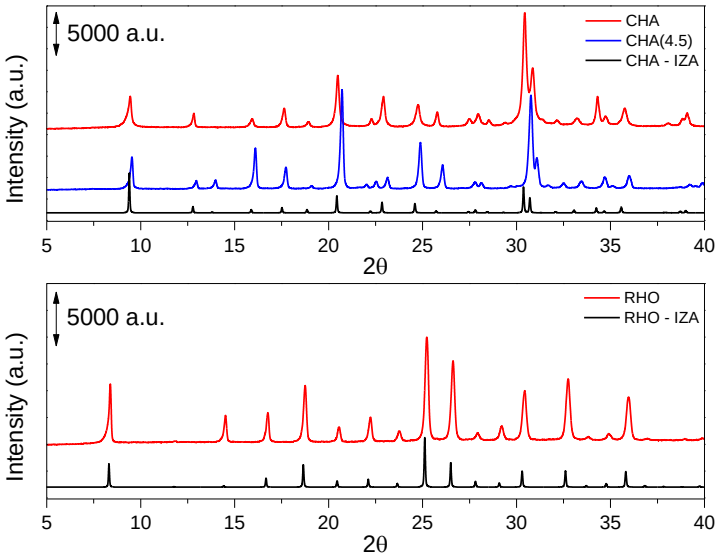

Figure 5.1. X-ray diffraction patterns of as-prepared zeolites RHO, CHA and CHA(4.5) compared to those profiles obtained from IZA[94] for both structures.

The as-prepared zeolites present the same peaks as for the simulated patterns obtained from IZA database, without the presence of concurring or dense phases (e.g. quartz or cristobalite), which confirm the synthesis success. The differences in angle and intensity of some peaks between samples and the standard from IZA can be attributed to the different composition between them since the standard pattern is calculated considering a pure silica material as well as the presence of water within the zeolite pores. By changing the chemical composition of the zeolite, the unit cell parameters are modified with repercussion on XRD patterns.[124]

Moreover, SEM (see **Figure 5.2**) investigation reveals that the typical morphology for NaCs-RHO and K-CHA structures is observed.

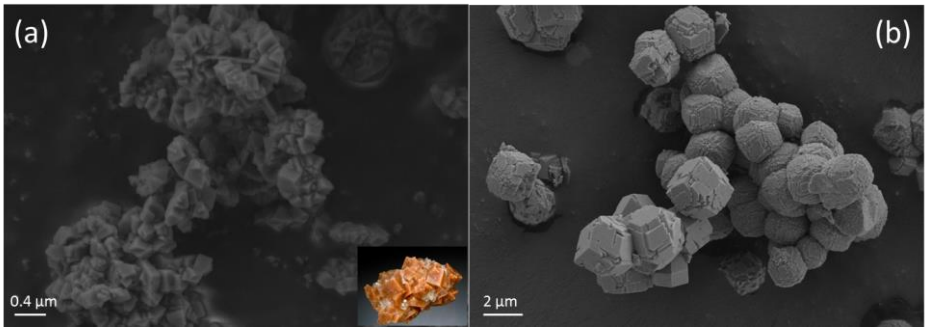

Figure 5.2. FESEM images of CHA (a) and RHO (b) zeolites. The inset of part (a) reports the morphology of natural chabazite crystal.

The NaCs-RHO crystals are characterized to be cubic with homogeneous size of ca. 2-4 µm while K-CHA zeolite possesses intergrowth of spiral-shaped crystals (typical for natural chabazite – see inset of **Figure 5.2a**) with crystal sizes smaller than 1 µm. Taking advantage of the EDS complementary technique available during FESEM measurements, the Si/Al ratio was verified for the zeolites (**Table 5.1**). From these measurements it is confirmed that target Si/Al ratios were achieved in all zeolites, since CHA and RHO show Si/Al ratio of ca. 2.2 and 4.3, respectively. These values were supported by ^{29}Si MAS NMR analysis, which shown very similar results (**Table 5.1**) after deconvolution of different Q-

type species of Si atoms in different local environment. The coincidence between bulk (EDS chemical analysis) and framework (^{29}Si MAS NMR) Si/Al ratios suggest that there is no extraframework Al species in the synthesized zeolites (or in very small amount). This was further confirmed by ^{27}Al MAS NMR. Indeed, the absence of any resonance at ca. 0 ppm and the presence of a single resonance around 50 ppm indicate that all Al atoms are isomorphically incorporated in both CHA and RHO frameworks with target Si/Al ratios. Both ^{29}Si and ^{27}Al MAS NMR spectra of as-prepared samples are in agreement with those for Ag-exchanged materials which will be shown after.

As-made zeolites NaCs-RHO, K-CHA and KH-CHA(4.5) were submitted to ion-exchange process in order to replace Na^+, K^+ and Cs^+ cations by Ag^+. The theoretical amount of silver was calculated to incorporate silver cations in 100 % of ion-exchange positions. As can be seen in **Table 5.1**, for both zeolitic structures the obtained degree of exchange reached ca. 70 % after silver exchange, being the remaining ion-exchange positions occupied by Cs^+ and K^+ for RHO and CHA, respectively. These values are compatible with ca. 6 (AgRHO) and 8 (AgCHA) Ag^+ per unit cell. In the case of RHO, it can be seen that sodium cations are selectively exchanged by silver, while Cs^+ remains at the same proportion than before ion-exchange procedure (ca. 30 %), most likely due to the large

ionic diameter of Cs^+ and its high stabilization inside the cages of RHO. For both AgCHA and AgRHO, the chemical analyses confirm that all exchange positions are occupied by cations since the $(Ag^+ + M^+)/Al$ ratio is close to 1, resulting in a silver loading of 26 and 16 wt.%, respectively (**Table 5.1**).

Table 5.1. Chemical composition of Ag-loaded zeolites.

Sample	Si/Al_{EDS}	Si/Al_{NMR}	Ag/Al_{EDS}	$(Ag^+ + M^+)/Al_{EDS}$	Ag wt.%
AgCHA	2.22	2.20	0.66	1.02 $(K^+)^a$	26
AgRHO	4.38	4.51	0.67	1.09 $(Cs^+)^a$	16
AgCHA(4.5)	4.23	-	0.53	0.86 $(K^+)^a$	14

[a]co-cation ($M^+ = Na^+$, Cs^+ or K^+) present after silver ion-exchange procedure

Differently, the obtained exchange degree in AgCHA(4.5) was slightly smaller (Ag/Al = 0.53, 14 wt.% of Ag) respect to the other samples, which can be attributed to the presence of small amount of H^+ as compensating cation in the starting material (formed during the decomposition of OSDA used for zeolite preparation). The presence of protons is known to suppress the exchanging of silver. In this case, the Ag/Al is decreased in comparison with AgCHA and AgRHO samples and the $(Ag^+ + M^+)/Al$ ratio ($M^+ = Na^+$, Cs^+ or K^+) is smaller than 1.

It is important to comment that it was not possible to obtain the chemical composition of Ag-based materials from ICP-OES due to the difficult sample disaggregation in the acidic mixture used during sample preparation. It is widely known that Ag^+ precipitates in presence of Cl^- ions, which made difficult the samples to be correctly analyzed. However, a good response was

obtained from EDS since the results for Si/Al ratio matched those obtained from solid state NMR.

The incomplete incorporation of silver in the three cases could be explained by the size of pore entrance in these small-pore zeolites which can hindrance the mobility of the cations. This problem has been reported in the preparation of Fe-CHA used as catalyst in NH_3-SCR. The ionic diameter of hydrated-Fe^{3+} cations (>8 Å)[253] is larger than the pore entrance of the zeolite (3.5 Å), making impossible the ion-exchange procedure. To overcome this problem the use of Fe^{2+} (under inert atmosphere to avoid Fe oxidation) instead of Fe^{3+} is necessary to prevent the formation of undesired bulky extraframework species. For this reason, some "one-pot" methodologies to introduce the cations already in the synthesis gel have been proposed.[136-137]

The zeolite stability after silver incorporation was verified by X-ray diffraction (**Figure 5.3**).

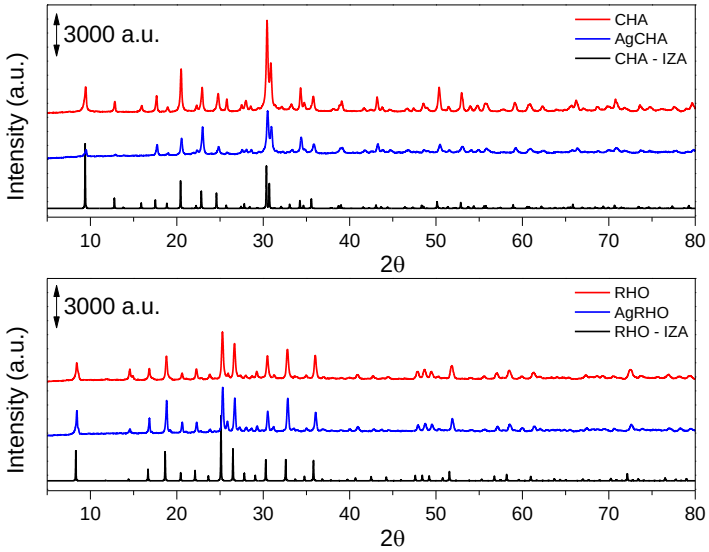

Figure 5.3. X-ray diffractograms of as-made and Ag-loaded CHA and RHO zeolites.

The silver-exchanged zeolites present similar diffraction patterns as for as-synthesized zeolites, with no structural amorphization indicia. It is known that silver (as well as other metals) as extraframework cation affects significantly the electronic densities of *hkl* planes,[254] which explain the differences in intensities of some diffraction peaks in Ag-zeolites respect to as-synthesized ones. It is possible to localize the silver cations in the zeolite channels by means of XRD, but in this work we were not able to perform such analysis. However, a similar procedure will be addressed by EXAFS further in the text. Importantly, no diffraction peaks related to

Ag_2O or metallic phase were observed, indicating that silver are well-dispersed within extraframework positions of zeolites.

XAS, UV-Vis spectroscopy and ^{109}Ag MAS NMR were used to assess the electronic structure and local environment of silver species and **Figure 5.4** gather the respective results from these techniques. The as-prepared Ag-loaded materials as well as Ag foil, $AgBF_4$, and bulk Ag_2O standards were analyzed by XANES at Ag K-edge (**Figure 5.4a)**. They present several well-defined features regarding the multiple scattering at around 25520 eV, and other bands arising from continuum resonances involving multiple scattering effects in the region above 25550 eV.[255] The shape of XANES spectra of AgCHA and AgRHO was close to that of $AgBF_4$, suggesting that Ag species in both zeolites are present as Ag^+ ions. Features in the pre-edge region are not observed in any spectra, indicating centrosymmetric geometry around silver atoms in the starting point. The |FT| of k^3-weighted $\chi(k)$ signal of Ag-zeolites (**Figure 5.4b**) shows that the local environment of silver is very similar in both zeolites since there is only one prominent peak centered 1.7 Å (not corrected in phase) attributed to Ag-O resembling in intensity either in CHA or RHO. Ag-O contribution of Ag_2O is more intense respect to that in zeolites and it is also slightly shifted to shorter distances, which confirm that the local order of Ag_2O is not found in the studied samples (see **Figure 5A.1** for data in k-space). The absence of higher shells in the spectra of samples

indicates that most likely the cations are highly dispersed within the zeolite. The chemical shift observed at 115 ppm in ^{109}Ag MAS NMR spectra is attributed to isolated Ag atoms in Ag-zeolites (**Figure 5.4c**). The small shift observed between the spectra can be explained by the different environment imposed by the unlike crystalline structure of the materials. In addition, the line width is typical from hydrated silver cations in zeolites.[239] Both Ag-loaded samples exhibit a band at 220 nm attributed to the charge transfer transition between $4d^{10}$ and $4d^9 5s^1$ levels of highly dispersed Ag^+ cations (**Figure 5.4d**), in agreement with earlier data from literature.[256] All these results from different characterization techniques strongly indicate that silver is present as Ag^+ and no clustering or nanoparticle formation were observed in the exchanged CHA and RHO zeolites.

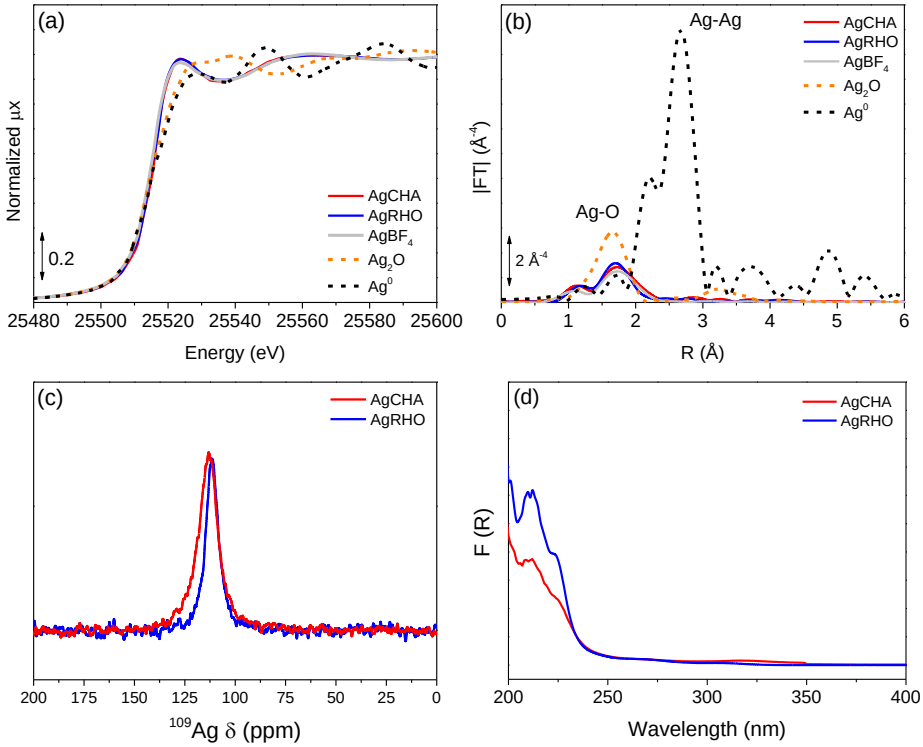

Figure 5.4. Normalized XANES (a) |FT| of the k^3-weighted EXAFS spectra (b), ^{109}Ag MAS NMR (c) and UV-Vis (d) spectra of as-made AgCHA and AgRHO.

The quantitative results derived from EXAFS data analysis for the initial state of AgCHA and AgRHO samples are reported in **Table 5.2**. Despite of using two completely different models to fit the data of both initial samples, the results converged to similar local environment around the silver atoms (curve-fittings available in **Figure 5A.2**). Two different Ag-O distances at 2.26 and 2.43 Å were necessary to fit the EXAFS signal, with average coordination number close

to 3. The introduction of Ag-T (T = Si or Al) path in the fit gave rise to results with no physical meaning and no Ag-Ag or Ag-K(Cs) distances were observed. Similar results were previously obtained by our group when studying the initial state of AgLTA zeolites, in which Ag-O distances ranging from 2.29-2.32 and similar N_{Ag-O} were obtained.[257] The results indicate that silver cations are interacting with oxygens atoms from the framework. However, the contribution of oxygen atoms from water molecules cannot be ruled out once the measurements were performed with samples in their hydrated state.

Table 5.2. Summary of EXAFS fit of the as-prepared Ag-loaded zeolites.[a]

Sample	CN	Path	R (Å)	σ^2 (Å^2)	ΔE_0 (eV)	r-factor
AgRHO	1.6(4) 1.2(2)	Ag-O	2.265(26) 2.432(36)	0.0060(35)	2.5(2.2)	0.0455
AgCHA	1.7(2) 1.7(2)	Ag-O	2.269(40) 2.427(43)	0.0082(52)	1.6(2.6)	0.0567

[a]Fits were performed on the first coordination shell (ΔR = 1.1-3.0 Å) over FT of the k^3-weighted $\chi(k)$ functions performed in the Δk = 2.3-11.8 Å^{-1} interval, resulting into a number of independent parameters of $2\Delta R\Delta k/\pi$ = 11.2. Non optimized parameters are recognizable by the absence of the corresponding error bar. S_0^2 = 0.80.

The clustering and nanoparticle formation on AgCHA and AgRHO upon *ex situ* thermal activation treatments under H_2 and O_2 flow were studied by a combination of laboratory techniques, such as XRD, UV-Vis, FESEM, TEM and solid-

state multi-nuclei NMR. The thermal treatment seen in the scheme of **Figure 5.5** was adopted.

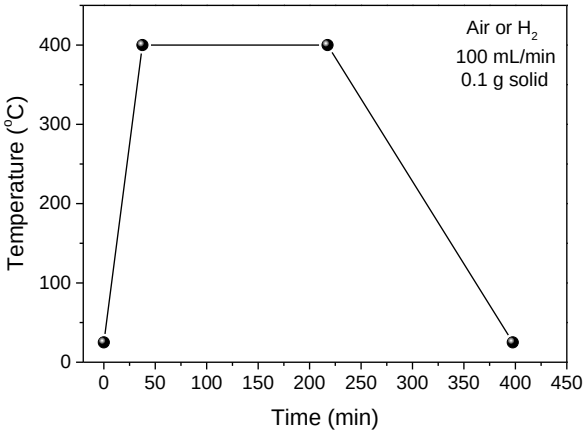

Figure 5.5. Scheme of *ex situ* thermal activation treatments performed on AgCHA and AgRHO.

During an experiment in chemistry several ways can be used to figure out if some phenomenon is taking place or not. One, though rather simple, is based on visual observation of sample coloration after a treatment. We compared the colors of AgCHA and AgRHO after "calcination" and "reduction" processes, and clear indication about the presence of different species can be observed in **Figure 5.6**. Both as-prepared silver-exchanged samples have a slightly yellowish coloration before treatments, which turned into completely white after calcination. It is know that for some Ag-zeolites the calcination strongly affects the sample colors, which can be dark yellow, orange or red in FAU and LTA structures.[239, 258-259] Such coloration is

strongly correlated with silver location in particular sites upon treatment. For instance, the yellow color in AgLTA is attributed to partially dehydrated Ag^+ cations coordinated to four member rings of the structure.[258] On the other side, the red color in the same zeolite is attributed to fully dehydrated Ag^+ cations in the four member rings but with a second Ag^+ cation in its neighborhood.[259]

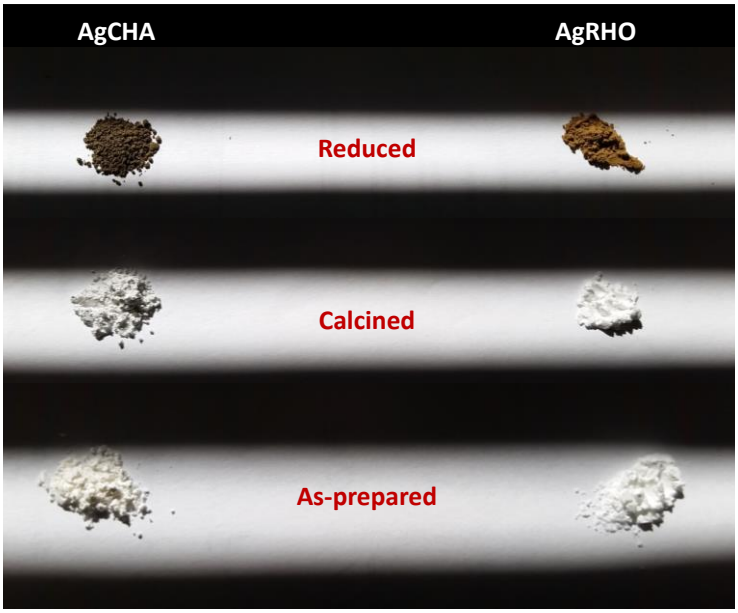

Figure 5.6. Color changes in zeolites AgCHA (left) and AgRHO (right) after *ex situ* activation treatments.

The CHA and RHO samples submitted to calcination in this work did not show any change in coloration after treatment, which is pointing out that there is no strong interactions between silver cations and framework oxygens or even cluster formation.

It is also important to highlight that an immediately rehydration process (after contact of the sample with the humidity of the air) does not produce any modification on samples' color, once it is not observed for other zeolite frameworks where colors were observed after activation (e.g. AgLTA[257]). Conversely, after the reduction process, the color of the samples rapidly changed from white to dark brown (CHA) and brown (RHO), indicating that clustering or nanoparticle formation occurred. Apart from differences in coloration, the color tones evolved over time, especially for AgRHO, going from brown to yellow only during storage while AgCHA remained almost unaltered. This behavior suggests that: i) different silver species or particle sizes are expected in the two samples and ii) evolution of silver species may occur specially on AgRHO sample.

UV-Vis spectroscopy (**Figure 5.7**) was used to study the electronic properties of samples after the above-mentioned thermal activation procedures (the spectra of as-made samples were included for comparison). The band at 220 nm assigned to the $4d^{10}$ to $4d^9s^1$ transition of Ag^+ ions initially present in spectra of as-made samples is maintained after calcination and no additional bands either in the UV region or in the visible can be detected, which is in agreement with the absence of color in samples before and after calcination in air. This indicates that the silver cations are very stable in the zeolite structure and resistant to the clustering process under oxidative conditions.[260]

On the other hand, when the samples are submitted to reduction under H_2 atmosphere, the evolution of different bands can be observed in two regions of the spectra. The UV-Vis profile observed for AgCHA will be named profile (I) while that observed for AgRHO will be named profile (II) along the text.

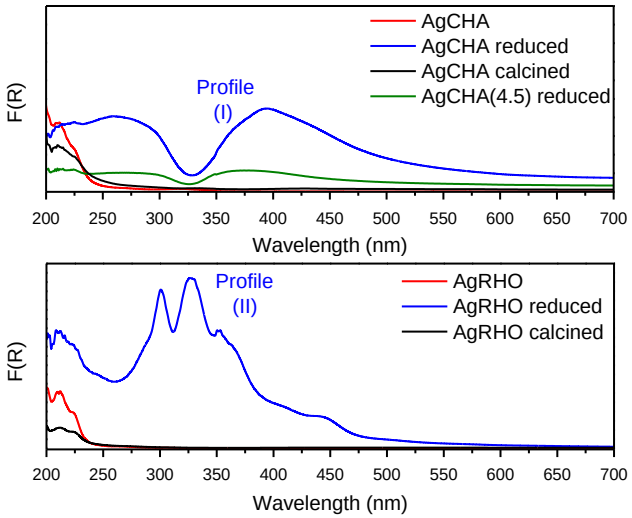

Figure 5.7. UV-Vis spectra of *ex situ* thermal treated AgCHA (top) and AgRHO (bottom) zeolites.

The profile (I) is composed by two broad bands ranging from 250-330 and 350-500 nm, which was attributed in literature to (bulk) silver nanoparticles.[261] More in detail, it is widely known that plasmon resonance band typical from Ag^0 and Au^0 nanoparticles is observed in the second range (350-500 nm)[262] while the first range is characteristic of metal clusters. Importantly, the AgCHA(4.5) in the reduced state also displayed

UV-Vis bands characteristics of profile (I), despite the differences in intensity that could be originated from instrumental effects (sample thickness, color, etc).

On the other hand, zeolite AgRHO shows profile (II), which is characterized by a split band ranging from 300 to 375 nm. This profile has been previously found in Ag-exchanged mordenite and erionite zeolites and ascribed as Ag_8 (Ag_8^0 and $Ag_8^{\delta+}$) clusters, although with slightly different peak positions due to the matrix effect (which could result in ca. 10 nm peak shift).[263-265] However, a tail is observed in the spectrum of reduced AgRHO, at the same position as for reduced AgCHA, which is an indicative that Ag metal particles could be also present in reduced AgRHO. A series of different silver clusters was reported for Ag-exchanged RHO,[266-268] but none of them are compatible with those observed in this work, most likely due to the different conditions used for activation.

The zeolite structure stability was also verified by X-ray diffraction after the thermal treatments under O_2 or H_2 (**Figure 5.8**). The presence of well-defined reflections typical of crystalline CHA and RHO materials demonstrates that no structural amorphization happened after oxidative and reductive treatments for both samples. The calcination with O_2 leads to almost equal XRD patterns as for as-prepared samples, despite some differences observed in the intensities of some diffraction peaks. Also, no peaks from silver oxide (Ag_2O – vertical red

lines in **Figure 5.8**) were observed, which confirms the interpretation performed by UV-Vis regarding the permanence of silver cations within the structure after activation. On the other hand, samples treated under H_2 atmosphere showed peaks assigned to metallic silver (black vertical lines in **Figure 5.8**) with *fcc* crystalline structure. Formation of silver nanoparticles gave rise to the main peaks positioned at 38, 44, 64, 77 and 81 degrees (asterisks). Moreover, the peaks from the zeolite are strongly suppressed due to the presence of reflections related to the formation of silver nanoparticles.

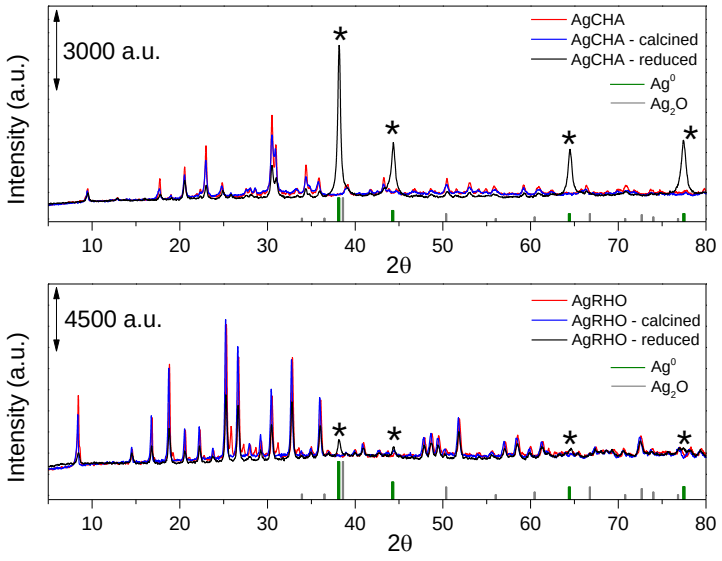

Figure 5.8. XRD patterns of *ex situ* thermal treated AgCHA (a) and AgRHO (b) zeolites.

Comparing XRD patterns of reduced AgCHA and AgRHO it is evident that the higher metal amount in AgCHA

result in narrow and well-defined peaks of Ag^0, which are much less pronounced in the pattern of reduced AgRHO. Using Scherrer equation for determination of crystallite size, values of 38 and 42 nm are obtained for AgCHA and AgRHO, respectively. As a comparison and in order to understand the results for zeolites with similar chemical composition (AgRHO and AgCHA(4.5)), the calculation of Ag metallic crystal size for reduced AgCHA(4.5) resulted in silver nanoparticles of 64 nm. It is important to underline that the overlapping of peaks from the matrix with those of Ag^0 could lead to inaccurate results.

As complementary information to verify the framework integrity, ^{27}Al and ^{29}Si MAS NMR were carried out. As for Ag-exchanged materials, the Al atoms remained tetrahedrally coordinated (chemical shift at ca. 50 ppm) in AgCHA (**Figure 5.9a**) and AgRHO (**Figure 5.9a**) after calcination with O_2, with minor differences in intensity related to the different number of scans during data acquisition.

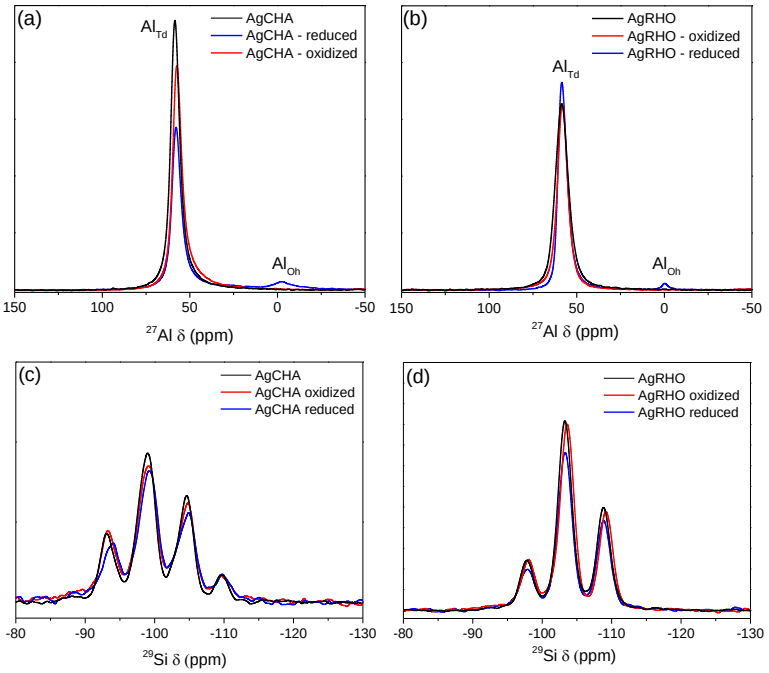

Figure 5.9. ^{27}Al and ^{29}Si MAS NMR spectra of treated AgCHA (a-c) and AgRHO (b-d), respectively.

In both cases, the activation with H_2 gave rise to a slightly formation of octahedral aluminum as extraframework species (chemical shift at 0 ppm). When silver species are reduced from Ag^+ to Ag^0, the negatively charged zeolite structure needs protons to compensate the charge that was previously compensated by silver ions. If this condition is not fulfilled, Al atoms come out of the framework, which results into the formation of Al species octahedrally coordinated (i.e. extraframework aluminum) and structural defects must be generated. Moreover, Al migration from framework to

extraframework positions could happen since aluminum-rich zeolites are less thermally stable than those silicon-rich.[69] On the other hand, the ^{29}Si MAS NMR spectra (**Figure 9bc**) shown the typical features observed in spectra of aluminosilicate zeolites with a Si/Al ratio up to 10, with few peaks corresponding to different number of AlO_4 tetrahedra connected to the silicon via oxygen atoms.[122] Furthermore, these peaks are related to the presence of only one T crystallographic sites in both CHA and RHO zeolites. The deconvolution of the spectra revealed minimum changes (**Table 5A.1**) in the local environment of the silicon atoms after treatment.

The silver particle sizes and morphology in reduced samples were characterized by transmission electron microscopy and some selected images are represented in **Figure 5.10**. Firstly, it is observed the typical morphology of zeolite crystals already seen by FESEM analysis (**Figure 5.2**). The CHA crystals appeared as an intergrowth, like fan-type crystals (see draw as example in **Figure 5.10a**), while RHO grows as cuboctahedra crystals (**Figure 5.10c)**, as shown by FESEM. The silver nanoparticles possess spherical-type shape with heterogeneous particle size distribution, since large silver particles can be seen in both cases.

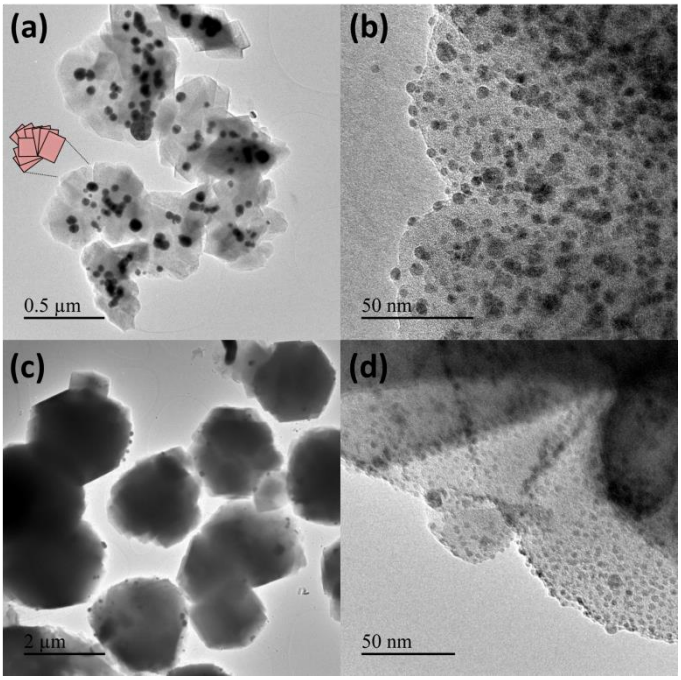

Figure 5.10. Selected TEM images of reduced AgCHA (a-b) and AgRHO (c-d).

It is important to underline that samples submitted to calcination were strongly affected by the electron beam and metallic nanoparticles were forming as far as the magnification was increased. Because of this, the results on calcined zeolites are clearly not reliable and will not be discussed here. The histograms showing the particle size distribution are gathered in **Figure 5.11**. Despite heterogeneity in size distribution is observed for AgCHA and AgRHO, both of them differ significantly in averaged size.

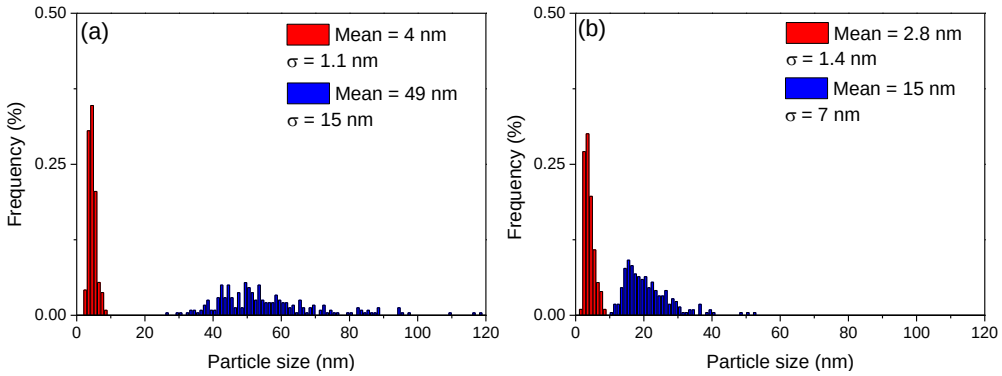

Figure 5.11. Particle size distributions of reduced AgCHA (a) and AgRHO (b). The histograms were divided into two (red and blue profiles) to express individual mean and σ for each part of the particle size distribution.

Both histograms of reduced AgCHA (**Figure 5.11a**) and AgRHO (**Figure 5.11b**) show bimodal profiles with significant maximum amount of particles between 2 and 8 nm, being the particles in this range (more specifically between 2 and 4) those which contribute more to frequency values. Moreover, it is clear that in both regions (red and blue columns) AgCHA displays higher mean values than AgRHO. Notwithstanding, due to the presence of significantly large nanoparticles (30-70 nm), the standard deviation (σ) is higher for AgCHA than AgRHO in the range of large particles (blue profiles). The large particles observed in AgRHO are shifted to smaller values (up to 40 nm) in comparison with AgCHA, most likely due to the lower silver amount present in this sample. Since beam sensitivity was observed in oxidized samples, with particles growing as

magnification was increased, the reduced samples could also be affected by this phenomenon, so apart from obvious formation of large particles at first seen, some care must be taken and the reliability of these results is not completely guaranteed.

5.1.2 In situ characterization of Ag-loaded zeolites during thermal treatments in oxidative and inert atmospheres

The activation procedure under O_2 atmosphere was also studied *in situ* by means of XAS. Alternatively, a similar thermal treatment was performed under inert atmosphere (He flow) to figure out if the so-called "autothermal" reduction under these conditions takes place. Here, the main advantage is that a powerful element-selective technique, such as XAS, was used to follow the evolution of silver species formed upon treatment without contacting the sample with air and/or moisture. The use of *ex situ* characterization techniques for tracking the evolution of silver species are useful for understanding the changes suffered by the material after activation. However, *in situ* XAS can provide strong additional information, like mobility of silver within framework, small clustering and corresponding local neighbors.

Figure 5.12 shows the XAS spectra of AgCHA and AgRHO collected at RT before and after thermal treatments under oxidative and inert atmospheres. The whole set of

temperatures (i.e. spectra collected at 100, 200, 300 and 400 ºC) is not included for brevity.

As already mentioned in literature, XANES features for Ag-based system are not so informative due to the small changes between the most common oxidation states found for silver, i.e. Ag^+ and Ag^0,[68] so the edge position cannot be used to following reduction process and also to estimate fractions of different compounds by linear combinations, as usually performed for other metals.[134] Nevertheless, the shape of XANES (**Figure 5.12)** in Ag-containing zeolites, Ag_2O and Ag metal is different and can be used as phase fingerprinting. The XANES spectra (**Figure 5.12ac**) of samples submitted to thermal activation do not suffer any strong modification regardless the used atmosphere, supporting the results obtained from previous *ex situ* techniques about Ag^+ stability. The moduli of Fourier transform (see **Figure 5A.3** for data in k-space) show that the Ag-O first shell contribution at 2.3 Å (not corrected in phase), which is related to silver interacting with framework oxygens, is retained. Also, it is observed the appearance of a second weak contribution between 2.5-2.6 Å (not corrected in phase) that is related to silver clustering (Ag–Ag path). The emergence of this second shell peak is more pronounced for He-treated samples (ca. 0.3 $Å^{-4}$ higher intensity) and a shift at lower distance is appreciated, which suggest different size or nuclearity of formed cluster. The term "cluster" is used due to

the enormous difference in intensity of this second shell peak in comparison with Ag foil, which is 10 times higher for metallic silver than for the sample.

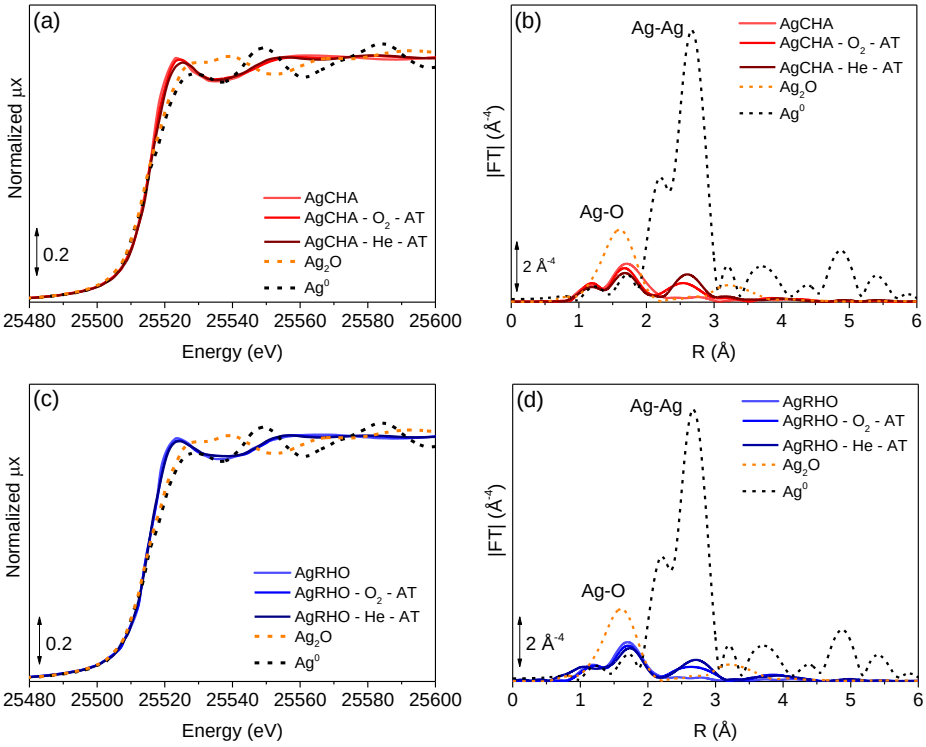

Figure 5.12. Normalized XANES spectra (left side) and |FT| of the k^3-weighted EXAFS spectra (right side) of AgCHA (a-b) and AgRHO (c-d) zeolites before and after thermal treatments under oxidative and inert atmospheres.

The pellets recovered from the *in situ* cell after XAS measurements were grinded (consequently exposed to air) and UV-Vis measurements were carried out to study the electronic

transitions of activated Ag-materials (**Figure 5.13**). As already observed in the case of samples treated *ex situ* the calcination with O_2 does not alter the initial UV-Vis profile of both AgCHA and AgRHO. Contrarily, the calcination under inert conditions does modify the spectra of Ag-loaded zeolites. In fact, in the spectrum of He-treated AgCHA the appearance of a double band positioned between 300 and 350 nm and another substantially broad band beyond takes place. He-treated AgRHO presented merely a broad band beyond 300 nm. The observed split band for He-treated AgCHA falls in the same region of the observed band in *ex situ* reduced AgRHO, which is attributed to the formation of Ag_8 clusters (UV-Vis profile (II)). However, the fact that most Ag atoms should be present as Ag^+ due to the maintaining of Ag-O contributions in |FT| and XANES features (**Figure 5.12**) of Ag-exchanged zeolites point out to a formation of small amount of clusters with this nuclearity. The presence of an additional broad band in plasmon region could be related to the formation of few silver nanoparticles.

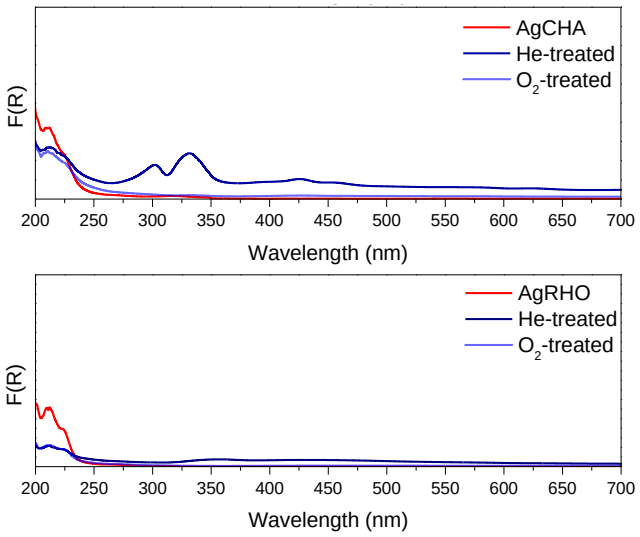

Figure 5.13. *Ex situ* UV-Vis spectra of *in situ* thermal treated AgCHA (top) and AgRHO (bottom).

As already observed in the case of samples treated *ex situ* the calcination with O_2 does not alter the initial UV-Vis profile of both AgCHA and AgRHO. Contrarily, the calcination under inert conditions does modify the spectra of Ag-loaded zeolites. In fact, in the spectrum of He-treated AgCHA the appearance of a double band positioned between 300 and 350 nm and another substantially broad band beyond takes place. He-treated AgRHO presented merely a broad band beyond 300 nm. The observed split band for He-treated AgCHA falls in the same region of the observed band in *ex situ* reduced AgRHO, which is attributed to the formation of Ag_8 clusters (UV-Vis profile (II)). However, the fact that most Ag atoms should be present as Ag^+ due to the maintaining of Ag-O contributions in |FT| and XANES features

(**Figure 5.12**) of Ag-exchanged zeolites point out to a formation of small amount of clusters with this nuclearity. The presence of an additional broad band in plasmon region could be related to the formation of few silver nanoparticles.

The differentiation of heavy atoms from lighter ones by FESEM using backscattered electrons mode can be an alternative way to visualize nanoparticles in solid matrices since under TEM analysis conditions the local environment of silver can be strongly modified. The red arrows in **Figure 5.14** indicate the presence of silver particles in both AgCHA **(a)** and AgRHO **(c)** upon thermal treatment under inert conditions in agreement with previous characterization techniques. Conversely, oxidative environment did not generate silver particles (or not large enough to be seen by FESEM) what suggests that under these conditions silver growth can be avoided (**Figure 5.14bd**). These results support the data obtained by XAS and UV-Vis which demonstrate that silver particles formation under inert conditions takes place although in minimal extension.

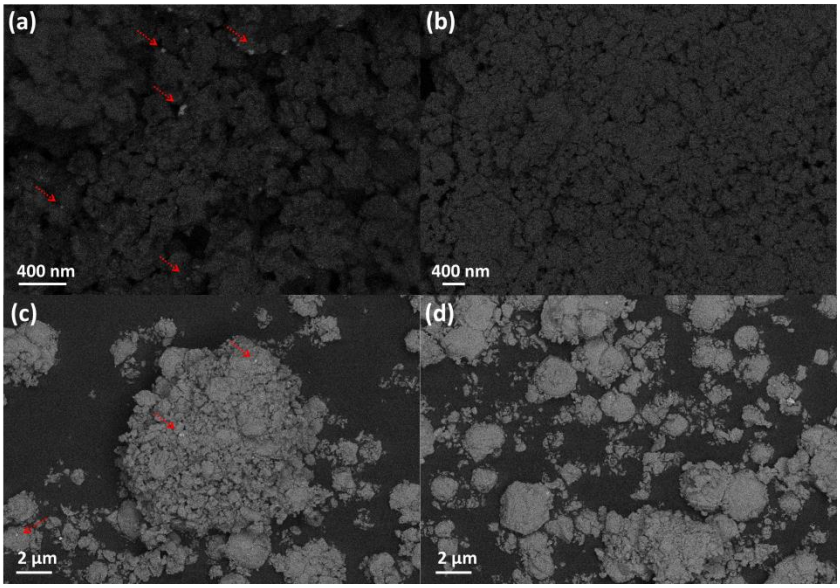

Figure 5.14. FESEM images collected in backscattered electrons mode of He- and O_2-treated AgCHA (a-b) and AgRHO (c-d), respectively.

The following scheme (**Figure 5.15**) is depicted aiming to sum up graphically the results obtained in this chapter so far, in which single thermal treatments under different atmospheres have been discussed.

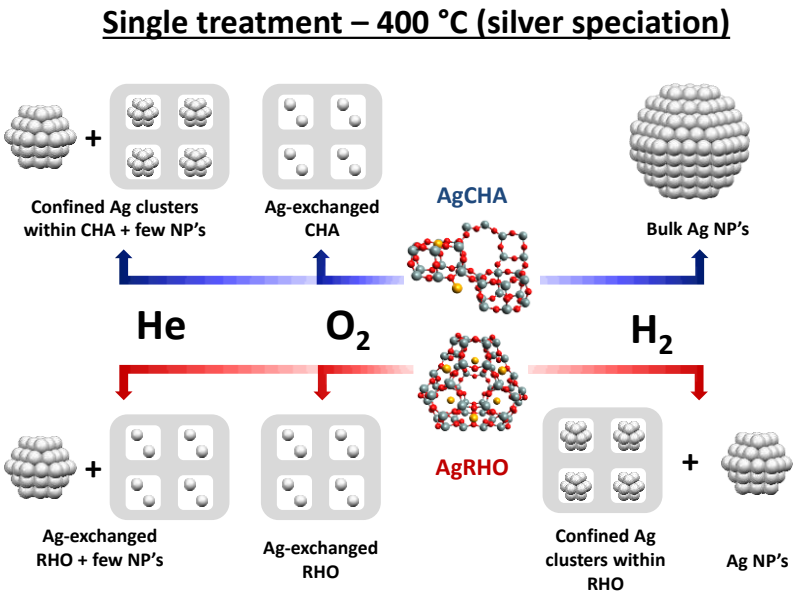

Figure 5.15. Summary of obtained results on silver speciation in AgCHA and AgRHO upon single thermal treatments under different atmospheres .

5.1.3 Nanoparticles formation and silver redispersion on Ag-loaded zeolites by thermal treatments

Since different species were observed for *ex situ* reduced AgCHA and AgRHO zeolites, an *in situ* XAS study of the influence of the reduction temperature on the size of silver nanoparticles was proposed. Also, the study of the reoxidation of reduced samples has been carried out for understanding the mechanism of redispersion of nanoparticles and clusters down to monoatomic silver cations (Ag^+).[30, 67] Then, the reduced Ag-

loaded zeolites were submitted to reoxidation after formation of Ag nanoparticles. This could be interesting for catalyst regeneration and for controlling the silver speciation, in terms of both size and type of species, for catalytic applications. **Figure 5.16** shows the XAS spectra of metal reduction in H_2 on AgCHA and AgRHO at increasing temperatures.

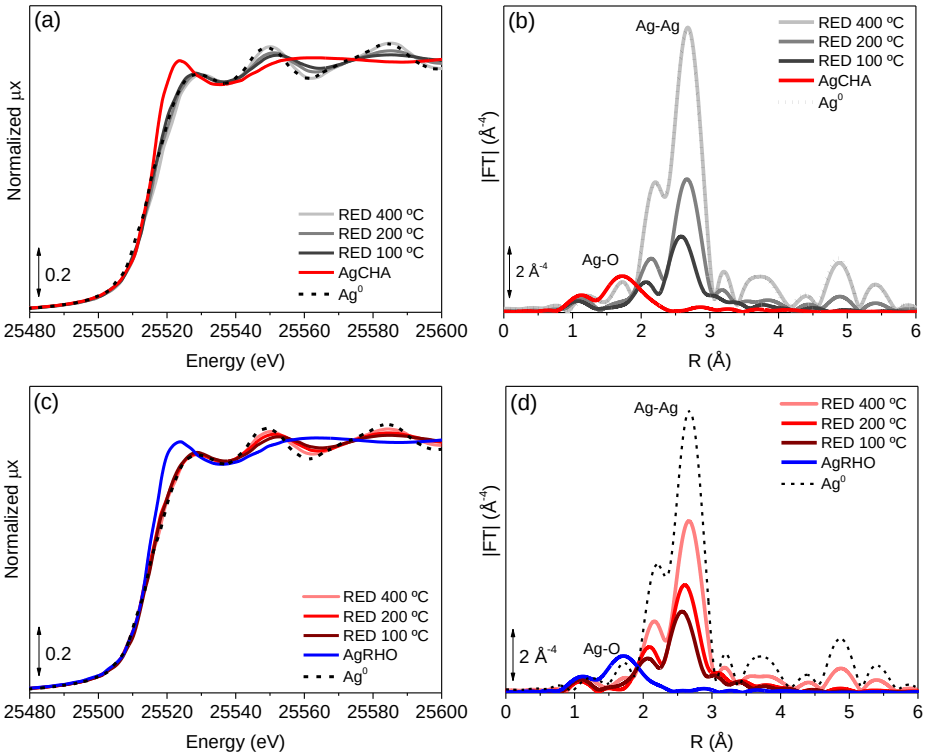

Figure 5.16. Normalized XANES spectra (left side) and |FT| of the k^3-weighted EXAFS spectra (right side) of AgCHA (a-b) and AgRHO (c-d) after reduction treatments.

After each reduction samples were cooled down at RT under H_2 atmosphere before data collection in order to minimize DWF and allow direct comparison. Normalized XANES spectra of reduced AgCHA at 400, 200 and 100 ºC (**Figure 5.16a**) did not present any shift in edge position compared to as-made AgCHA (E_0 at 25514 eV) according to the previous results discussed above. However, despite the absence of an edge displacement, the whiteline decreases and shifts to the right respect to the initial spectrum, being an indication of metal reduction and subsequent formation of an *fcc*-type spectrum resembling those for Ag^0 (black dashed line) in all cases. In addition, the oscillations beyond the absorption edge are flattened and slightly shifted around 25560 eV in spectra of samples reduced at lower temperatures (100 ºC > 200 ºC > 400 ºC). This behavior is related to the formation of different size metal nanoparticles where metallic atoms with lower coordination number give rise to the observed flattening.

The moduli of Fourier transform showing the changes before and after reduction processes are shown in **Figure 5.16b** (see **Figure 5A.4** for data in k-space). It is clearly seen that Ag-O (1.7 Å – not corrected in phase) first shell peak initially present completely disappears after metal reduction in all cases, giving rise to the appearance of intense Ag-Ag contribution at 2.6 Å coming from the formation of metallic silver. Here, the differences observed in XANES respect to the size of silver

nanoparticles become evident due to the different peak intensities formed depending on the reduction temperature. Sample $AgCHA_{RED400}$ gives rise to almost bulk silver metal since the spectra is similar in both shape and intensity in comparison with that of Ag^0 foil. Conversely, the samples $AgCHA_{RED200}$ and $AgCHA_{RED100}$ show a decrease of peaks intensity (ca. 6 and 8.2 $Å^{-4}$, respectively) accompanied by contraction of bond distances (0.02 and 0.09 Å, respectively). Both phenomena suggest the formation of much smaller nanoparticles under these reduction conditions. Furthermore, this is supported by the contraction on bond distances of 0.02 and 0.09 Å in |FT| (not phase corrected) for $AgCHA_{RED200}$ and $AgCHA_{RED100}$, respectively.

The normalized XANES at Ag K-edge related to the reduction treatments of AgRHO are shown in **Figure 5.16c**. As for AgCHA, the transition between Ag^+ to Ag^0 is observed after all reduction treatments and the effect of different particle size on XANES features as well. However, the spectra of sample reduced at higher temperature ($AgRHO_{RED400}$) did not resemble perfectly the XANES of Ag metal which suggests that particle sizes in AgRHO sample treated under harsher conditions are not as observed in AgCHA cases. This is confirmed by the |FT| in **Figure 5.16d** where is possible to see the same trend observed for AgCHA but with the Ag-Ag contribution significant less intense respect to chabazite-based samples, especially at 400 ºC.

In addition, the position of the nearest-neighbor peak is also shifted to smaller values of R (not phase corrected), which once again indicates the different reduction treatments generate silver nanoparticles with different sizes, following this order: NP's formed at 400 ºC > 200 ºC > 100 ºC.

The quantitative analysis on EXAFS data of reduced Ag-loaded zeolites was performed and is gathered in **Table 5.3** (curve-fittings available in **Figure 5A.5**).

Table 5.3. Summary of EXAFS fit of the reduced Ag-loaded zeolites.[a]

Sample	CN	R (Å)	σ^2 (Å^2)	ΔE_0 (eV)	C_3	r-factor
$AgCHA_{RED400}$[b]	11.1(8)	2.852(12)	0.0093(6)	2.0(5)	-	0.0045
$AgCHA_{RED200}$[b]	7.6(8)	2.837(16)	0.0127(11)		-	0.0148
$AgCHA_{RED100}$	5.1(5)	2.828(17)	0.0144(14)		0.0007(3)	0.0577
$AgRHO_{RED400}$[b]	8.6(7)	2.850(14)	0.0114(9)		-	0.0085
$AgRHO_{RED200}$	6.6(6)	2.835(15)	0.0134(11)		0.0006(3)	0.0221
$AgRHO_{RED100}$	4.5(5)	2.817(18)	0.0126(15)		0.0007(3)	0.0550

[a]The fits were performed on the first coordination shell (ΔR = 2.0-3.0 Å) over FT of the $k^1k^2k^3$-weighted $\chi(k)$ functions performed in the Δk = 2.3-11.8 Å^{-1} interval, resulting into a number of independent parameters of $2\Delta R\Delta k/\pi$ = 34.3 without C_3 (56.4 with C_3). S_0^2 = 0.80 [b]Values obtained without C_3 fitting Ag metal reference.

As discussed in **Chapter 1**, the clearest parameter to discuss nanoparticle size is the coordination number but also the bond distances and σ^2 can provide additional and valuable information about the system. The results summarized in **Table 5.3** show that there are at least 3 trends in the results: CN, R and r-factor. As the reduction temperature increase, the coordination number increase, demonstrating a clear sintering effect upon heating in H_2 flow. In principle, the fact that AgCHA has almost

twice amount of metal than AgRHO makes sensible the observed results (the effect of zeolite structure on the size of species will be further discussed). The Debye-Waller factor in all cases is relatively high in comparison with data of metal nanoparticles in literature (ca. 0.006 $Å^2$).[28, 69] This σ^2 value clearly increases with decreasing the metallic size, although for AgRHO sample the reduction at 100 and 200 ºC leads to similar results. The trend is also observed in fitting errors, which can be attributed to the fact that the model used for the fitting employs as FEFF input a crystallographic file coming from bulk metallic silver. When the number of low coordinated atoms is high in nanoparticles/clusters, the model of a bulk metal fails to unequivocally determine the parameters of the analysis, although good approximation can be achieved. Last but not least, increasing the CN, the bond distance also increases, which was already observed for Pd-based catalysts in **Chapter 4** and can be directly related to the different particle size. The application of the cumulant approach for characterizing the reduced Ag-loaded zeolites indicates that for CN below 8, the changes in R_{Ag-Ag} are really significant (**Figure 5.17**). For coordination numbers higher than 8 the values of C_3 obtained in fitting procedure was 0 within the error, for this reason for the final fit it is neglected and C_3 fixed to 0. This behavior is in agreement with literature where smaller errors were found for large metallic clusters in which most atoms are in the bulk.[42]

The obtaining of positive C_3 values for samples with coordination numbers smaller than 8 (more specific for $AgRHO_{RED100}$ and $AgRHO_{RED200}$) indicates that Ag-Ag bond distances were underestimated and needed a correction to obtain reliable values. Despite the inconsistencies found on using the cumulant approach or not to determine the Ag-Ag bond distances, a good trend is observed in both cases (see **Figure 5.16**), demonstrating that particle size affects directly the bond distance in silver nanoparticles.

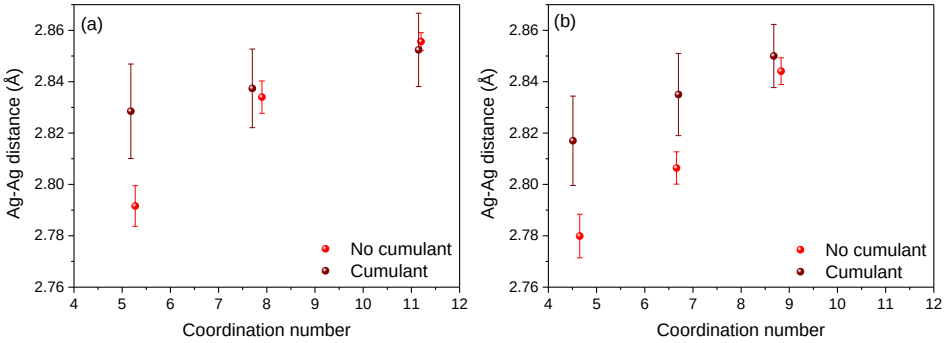

Figure 5.17. Consequences of using the cumulant approach on Ag-Ag bond distances in AgCHA (a) and AgRHO (b) zeolites.

The different reduction treatments were performed *ex situ* in order to correlate the coordination number with UV-Vis bands appearing at each reduction step (**Figure 5.18**). It can be seen that $AgCHA_{RED100}$ and $AgCHA_{RED200}$ displayed similar UV-Vis bands as for the AgCHA treated under inert conditions (UV-Vis profile (II)) which was previously ascribed as indicia

of clusters formation, more specifically Ag_8-type. With temperature rising up to 400 ºC, the spectrum attributed to bulk Ag^0 is formed. Conversely, AgRHO also presented a trend (from 100 ºC to 400 ºC) but never reaches the formation of bulk silver according to its spectra. In comparison with the obtained coordination numbers, it is reasonable to say that below CN = 8, the Ag_8 clusters are present which is in line with the discussion about bond distances where only samples with smaller coordination numbers are affected by R_{Ag-Ag} underestimation.

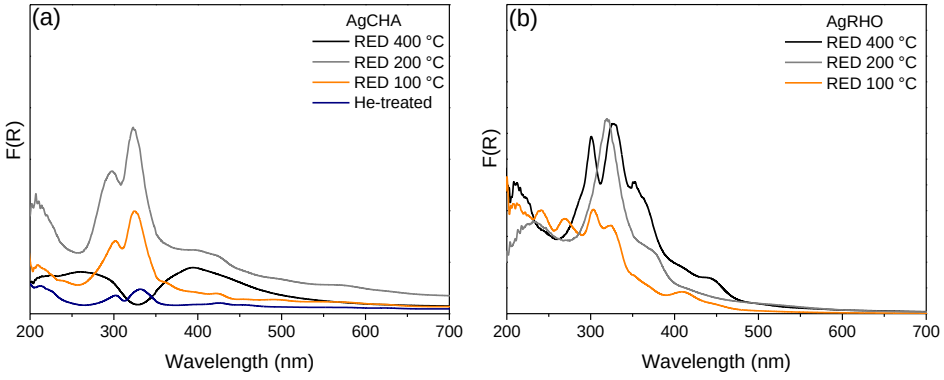

Figure 5.18. *Ex situ* UV-Vis spectra of reduced AgCHA (a) and AgRHO (b) at different temperatures.

Both EXAFS results and UV-Vis spectra strongly suggest the influence of RHO zeolite on the formation of silver species with different size respect to CHA zeolite. To support this hypothesis, ^{109}Ag MAS NMR was performed (**Figure 5.19**). Interestingly, the knight-shifts (chemical shifts attributed to Ag^0)[239] of $AgCHA_{RED400}$ and $AgRHO_{RED400}$ display different

broadening profiles in comparison with Ag metal. The first reproduces perfectly the broad background while AgRHO are significantly narrower, fact that proves the results obtained by other techniques. Moreover, the $AgCHA_{RED100}$ displayed the same narrowing effect in comparison with $AgRHO_{RED400}$, confirming the observations done so far. However, it is important to underline that knight-shifts observed for the samples should be related to silver metal particles present outside the zeolite cavities, since the assignation of this chemical shift is related to relatively large particles.[269]

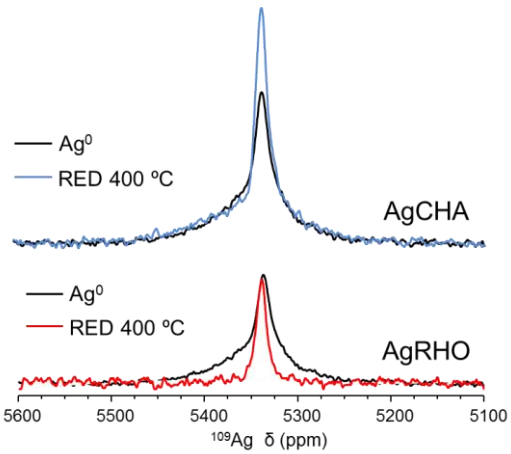

Figure 5.19. ^{109}Ag MAS NMR spectra of reduced AgCHA and AgRHO zeolites.

The *in situ* reoxidation of silver nanoparticles formed on Ag-containing zeolite was studied employing the same reoxidation temperature (400 ºC) for all samples. The prolongation of reoxidation up to temperatures higher than 400

ºC, as reported in literature,[69] was not performed due to the time limitation during XAS beamtime. The normalized XANES spectra of reoxidized AgCHA (**Figure 5.20a**) and AgRHO (**Figure 5.20c**) demonstrate that silver reoxidation from Ag^0 to Ag^+ occurs regardless of reduction temperature used to form the silver nanoparticles. This oxidation is characterized by the shift of the white line upwards with maintenance of absorption edge positioned at 25514 eV as for as-made samples. This process takes place along with the disappearance of the typical oscillations related to metallic *fcc*-type structure of silver. However, for the AgCHA-R4O sample (reoxidized after reduction at 400 ºC), it is still possible to observe some reminiscent oscillations, which indicates that complete reoxidation is not achieved in this case, most likely due to the large size of silver nanoparticles formed at the reduction step. As for the O_2- and He-treated samples reported above, no Ag_2O formation was observed, which demonstrate that silver is being redispersed within the framework as Ag^+.

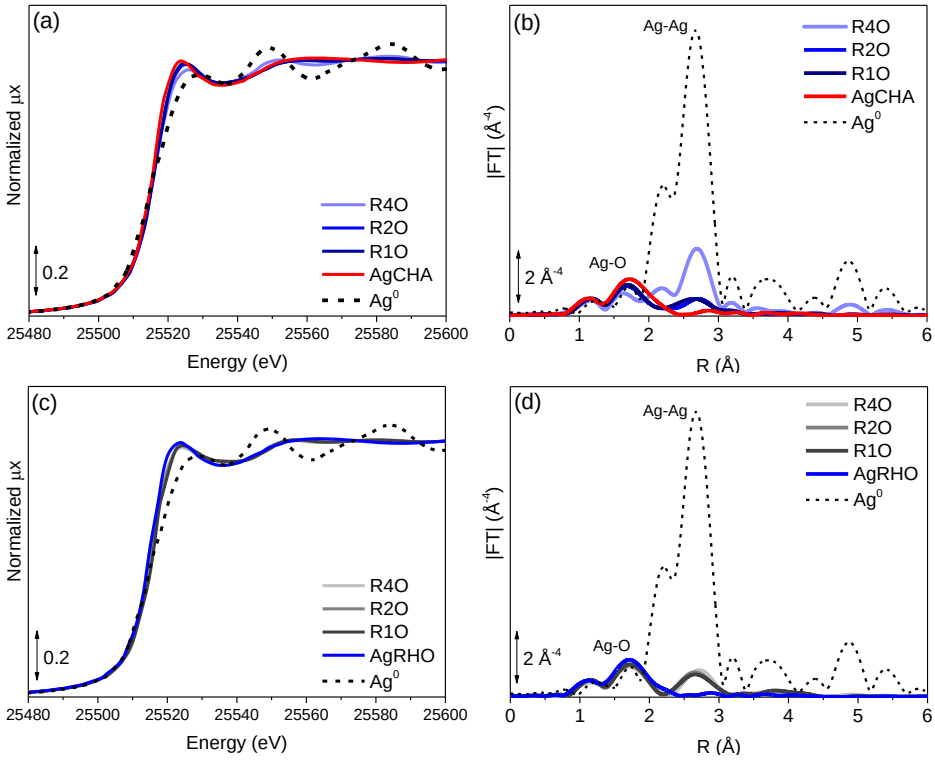

Figure 5.20. Normalized XANES spectra (left side) and |FT| of the k^3-weighted EXAFS spectra (right side) of AgCHA (a-b) and AgRHO (b) after subsequent reoxidation treatments.

In fact, the moduli of Fourier transform (see **Figure 5A.6** for data in k-space) of reoxidized samples (**Figure 5.20b-d**) show that, the first shell peak of Ag-O path is reestablished as for as-prepared samples. On the other hand, the contribution of the Ag-Ag distance in the |FT| strongly decreases (from 11.1 to 1.0 $Å^{-4}$) upon reoxidation but it is still present in most cases. As observed in XANES spectrum, AgCHA-R4O still displays the

metallic feature in a greater extent (in intensity terms) respect other samples (2.6 against 1.0 $Å^{-4}$), pointing out that bulk size species are harder to redisperse as Ag^+ cations. Interestingly, the position of Ag-Ag contribution peak for reoxidized spectra respect to that of reduced sample is shifted to higher R-values (R_{shift} = 0.08 Å). This indicates that small particles with shorter Ag-Ag bond distance are being oxidized while the remaining Ag species are those with large size (and consequent longer Ag-Ag bonds), which is in agreement with the idea that larger particles are harder to be transformed into cations. Although the determination of the amount of remaining Ag^0 particles cannot be estimated on the basis of these data, it is very likely that only a small amount (per total mass of silver) is present due to the discrete intensity of Ag-Ag contribution in the Fourier transform and the XANES profiles, which are mainly composed by features characteristic from Ag^+ in zeolites.

The samples after reoxidation were also characterized by XRD, ^{109}Ag MAS NMR and UV-Vis spectroscopies. The XRD patterns of reoxidized Ag-loaded samples (**Figure 5.21**) show that zeolite structures was maintained after two successive thermal treatments (1^{st} reduction → 2^{nd} reoxidation).

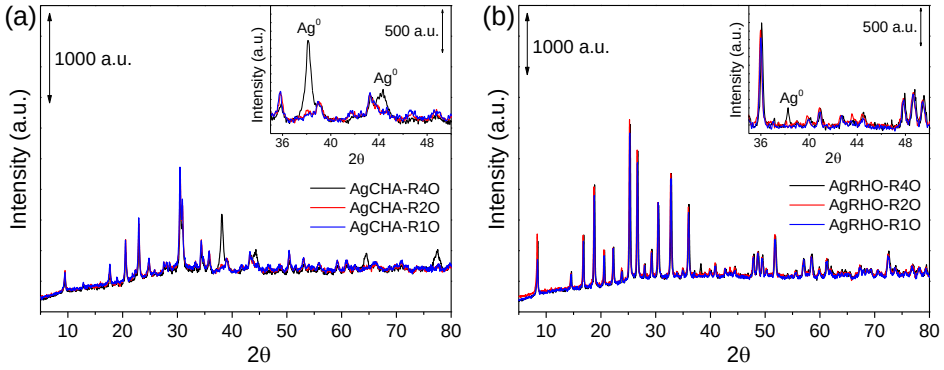

Figure 5.21. XRD patterns of AgCHA (a) and AgRHO (b) after reoxidation processes. Inset: selected 2θ range for better visualization of Ag^0 peaks.

The peaks related to Ag^0 were still present mainly in samples AgCHA-R4O and AgRHO-R4O, with emphasis on AgCHA where the peak at 38º is quite intense, confirming the permanence of large silver particles in this sample after reoxidation. This peak can be also seen in AgRHO-R4O but with much less intensity respect to AgCHA-R4O. A modest shoulder (almost imperceptible) is visible for AgCHA-R2O at 38º which indicates the presence of a small amount of metallic silver in this sample. The other samples did not show any visible peaks attributed to metallic silver or silver oxide: if present they are below the detection limit of the technique.

UV-Vis spectra of reoxidized samples are gathered in **Figure 5.22**.

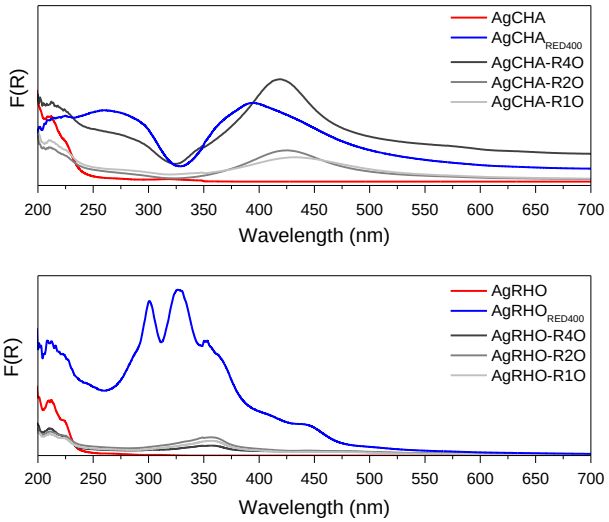

Figure 5.22. *Ex situ* UV-Vis spectra of reoxidized AgCHA (top) and AgRHO (bottom) zeolites.

The spectra of reduced AgCHA and AgRHO at 400 ºC are included for comparison purposes. For AgCHA-R1O and AgCHA-R2O samples, the first band of UV-Vis profile (I) (250-330 nm) is strongly consumed which can be attributed to the easy oxidation of clustered species while the second band (centered at 425 nm) is still present but much less intense respect that for $AgCHA_{RED400}$, which confirms the presence of metal silver particles after reoxidation treatment. Nonetheless, AgCHA-R4O show both bands typical from that profile attributed to bulk Ag^0 although with some differences in intensity for the first band (250-330 nm) due to clusters oxidation.[261] The band at 220 nm attributed to the charge transfer transition between $4d^{10}$ and $4d^9 5s^1$ levels of highly

dispersed Ag^+ cations[256] is reestablished and well visualized for AgCHA-R1O and AgCHA-R2O samples. On the other hand, for all RHO-based samples the typical band of Ag^+ species is shown while a quite similar band centered at 355 nm attributed as Ag^0 nanoparticles[261] can be seen. The observed differences in the position of bands related to silver nanoparticles (350 nm for RHO and 425 nm for CHA) can be attributed to different nanoparticle sizes between the two series of samples.

To support the hypothesis that smaller nanoparticles were being reduced leaving only those of large size present, ^{109}Ag MAS NMR analysis were carried out (**Figure 5.23**).

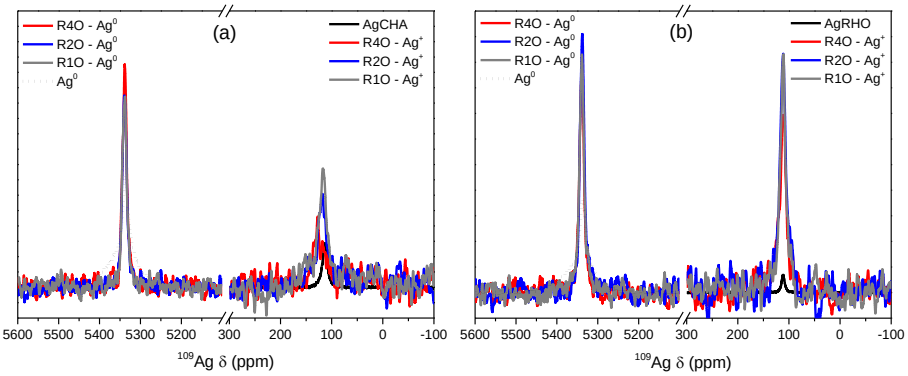

Figure 5.23. ^{109}Ag MAS NMR spectra of reduced and reoxidized AgCHA (a) and AgRHO (b) zeolites.

The spectra show chemical shifts in both regions of Ag^0 and Ag^+, with narrower peaks width in comparison with Ag metal, which once again confirm the above mentioned discussion about silver redispersion. RHO-based samples

possess roughly the same amount of species in each sample. However, the CHA-based samples displayed less Ag^+ in AgCHA-R4O sample among the samples, while AgCHA-R1O showed the higher amount of Ag^+, suggesting that the amount of cations after redispersion is dependent on the reduction temperature of AgCHA.

The observed color change of the samples upon oxidation is a strong support of the above phenomenon. **Figure 5A.7** demonstrates that different redox treatments give rise to different coloration in AgCHA, being darker for AgCHA-R4O and so on. On the other hand, AgRHO samples presented quite similar color regardless the reduction temperature.

The "consumption" of large particles after redox cycles can be confirmed by TEM in **Figure 5A.8** where AgCHA-R4O and AgRHO-R4O are shown. However, it was already commented that electron beam can affect significantly the state of Ag^+ so that showed histograms should be considered carefully.

Finally, after the whole characterization on Ag-loaded zeolites submitted to redox treatments it is important to comment some aspects about the influence of framework structure on the generated metallic silver species. It is clear that tuning the reduction temperature of these systems can lead to materials with different properties in terms of nuclearity, which can be posteriorly redispersed across the whole zeolite by

reodixation, with possibility to start a new reduction cycle and so on. However, a large part of the characterization techniques were performed with two samples of different Ag loading, which can generate different results due to their chemical composition. To support the assumptions of this chapter and try to prove that RHO can generate silver species with different properties (e.g. in terms of size) respect to CHA, some extra samples were prepared and submitted to the harsher treatment (reduction in H_2 at 400 ºC).

One of the samples was already mentioned in some previous sections, i.e. AgCHA(4.5), which has similar chemical composition of AgRHO. The second sample was prepared by exchanging all cesium cations of RHO by sodium cations, in order to evaluate the effect of a smaller co-cation in silver aggregation, which, in principle, would facilitate intraparticle diffusion. Both samples were submitted to reduction in H_2 flow at 400 ºC and were analyzed by *in situ* XAS and *ex situ* UV-Vis spectroscopies. The quantitative EXAFS results of reduced samples are summarized in **Table 5.4**.

Table 5.4. Summary of EXAFS fit of the additional reduced Ag-loaded zeolites.[a]

Sample	CN	R (Å)	σ^2 (Å^2)	ΔE_0 (eV)	C_3	r-factor
$AgCHA(4.5)_{RED400}$	11.3(6)	2.857(2)	0.0102(5)	1.5(2)	-	0.0029
$AgNaRHO_{RED400}$	9.3(5)	2.845(3)	0.0124(6)		-	0.0032

[a]The fits were performed on the first coordination shell (ΔR = 2.0-3.0 Å) over FT of the $k^1k^2k^3$-weighted $\chi(k)$ functions performed in the Δk = 2.3-11.8 Å^{-1} interval, resulting into a number of independent parameters of $2\Delta R\Delta k/\pi$ = 11.4 without C_3. S_0^2 = 0.80

The reduced CHA-based sample showed similar results as $AgCHA_{RED400}$, with average coordination number close to that typical of bulk silver (CN_{Ag-Ag} = 12) and R_{Ag-Ag} already observed for the Ag nanoparticles of this work. On the other hand, the $AgNaRHO_{RED400}$ sample displayed slightly higher average coordination number in comparison with AgRHO, but smaller N_{Ag-Ag} and also shorter R_{Ag-Ag} respect to silver metal (curve-fittings available in **Figure 5A.9**). All fits showed good r-factors which indicate a good fit of the experimental data. For these two samples the cumulant approach resulted in C_3 values close to 0 as expected by the high CN, indicating that regular least-squares fit is sufficient for a good estimation of R_{Ag-Ag}. The UV-Vis spectra of the additional Ag-containing zeolites are shown in **Figure 5.24**.

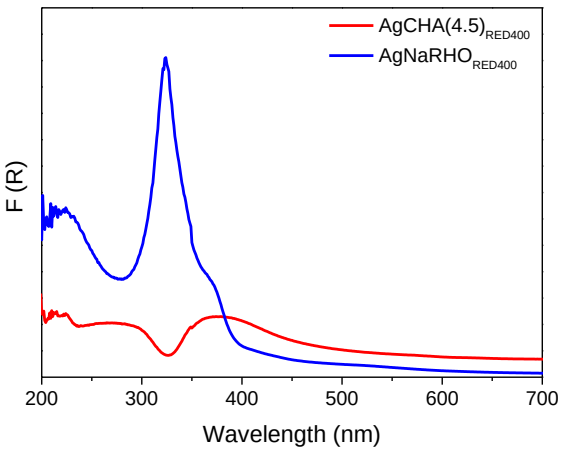

Figure 5.24. UV-Vis spectra of reduced AgCHA(4.5) and AgNaRHO zeolites.

As expected, the $AgCHA(4.5)_{RED400}$ presents UV-Vis profile (I) typical of large nanoparticles. Conversely, the $AgNaRHO_{RED400}$ displays the "RHO" profile, previously denominated as profile (II), which is attributed to the presence of silver clusters (Ag_8-type). These results clearly indicate that, under harsher conditions (400 ºC – H_2 flow) and regardless of the cation type (Cs^+ or Na^+), RHO structure drives the formation of Ag_8-type species. This behavior was further confirmed preparing some catalysts by incipient wetness impregnation rather than ion-exchange, which shown same UV-Vis profile than AgRHO-based materials reported in this thesis (data not shown).

The *in situ* reoxidation of $AgCHA(4.5)_{RED400}$ was studied by means of XAS (**Figure 5A.10**). As for AgCHA, similar results were observed for AgCHA(4.5). The reoxidation resulted in the maintenance of Ag-Ag contribution in larger quantity than for AgRHO. It is possible to underline that now the comparison between chemical composition can be straightforward in terms of silver loading once AgCHA(4.5) has a similar Ag/Al ratio in its composition. This points out that redispersion degree is more dependent on the size of the formed species than on the amount of metal.

In general, the only explanation that could elucidate the results found for the RHO zeolite lies on its framework structure. The RHO zeolite is known for its high flexibility and

can also display negative thermal expansion with heating, where the material suffers a contraction.[165, 239] If so, when RHO-based materials undergone silver reduction, a significant amount of cations remain trapped inside the zeolite, resulting in the species that have the UV-Vis profile (II) presented throughout this work. A smaller coordination number would be expected for AgRHO-based samples in the case of the presence of clusters in a whole. However, the formation of silver nanoparticles that migrate out of the zeolite causes the coordination number to be higher than that expected just for Ag clusters. In any case, these results will be interesting for the next section when the catalytic consequences will be addressed.

The following scheme (**Figure 5.25**) summarizes some results obtained during subsequent treatments of reduction/reoxidation.

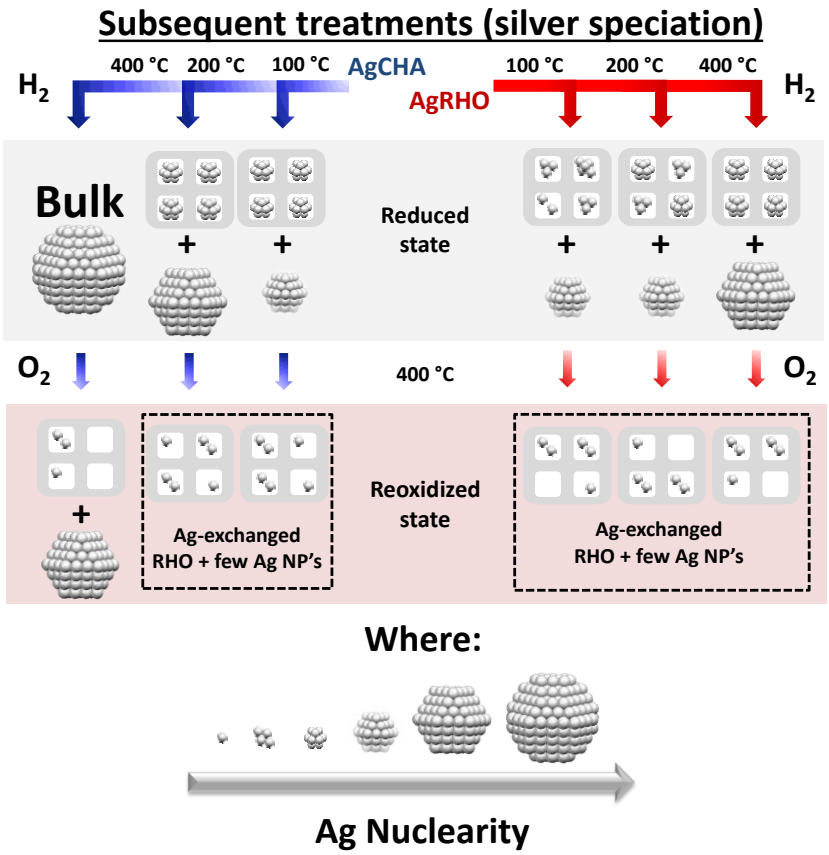

Figure 5.25. Summary of obtained results on silver speciation of AgCHA and AgRHO upon subsequent redox thermal treatments.

5.1.4 Catalytic implications of different activated Ag-loaded zeolites for SCO-NH_3

A preliminar study performed by our group suggested that catalysts composed essentially by silver cations or slightly clustered species are considerable inactive in SCO-NH_3 in

comparison with reduced silver species (data not shown). Taking this into account, the following results were obtained with catalysts containing silver nanoparticles in its composition, regardless of their extent or size.

Figure 5.26a shows the NH_3 conversion as a function of the reaction temperature in the NH_3-SCO reaction for $AgCHA_{RED400}$ and $AgRHO_{RED400}$ catalysts and the blank reaction without any catalyst.

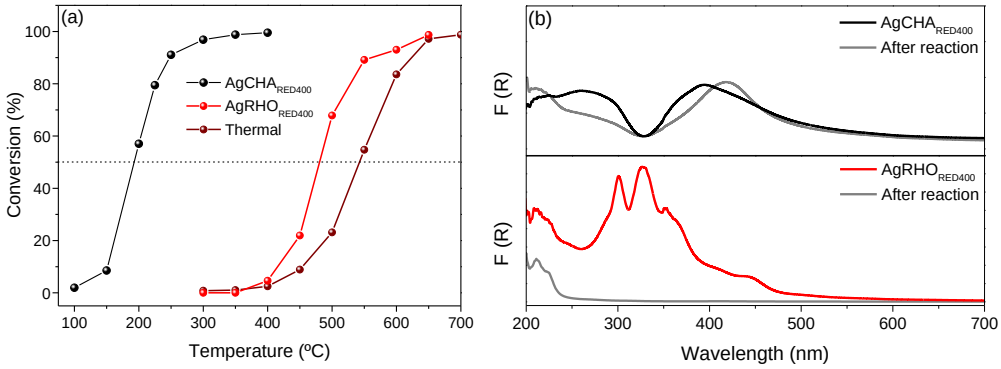

Figure 5.26. Catalytic activity for the SCO-NH_3 reaction of $AgCHA_{RED400}$ and $AgRHO_{RED400}$ (a) and respective UV-Vis spectra of the catalysts before and after reaction (b).

The catalytic activity of $AgCHA_{RED400}$ at lower temperatures is higher respect to $AgRHO_{RED400}$. The former reached 50 % of NH_3 conversion ($T_{50\%}$) at 200 while the latter at 475 ºC. Moreover, they reached 100 % of NH_3 conversion ($T_{100\%}$) at 300 and ~600 ºC, respectively. In fact, $AgRHO_{RED400}$ behaves similarly to the thermal decomposition of NH_3 without

catalyst. The results point out that the type or amount of silver in Ag-based catalysts are playing an important role in the catalytic conversion of ammonia. Importantly, after reaction there is a change in the color of AgRHO catalyst: $AgRHO_{RED400}$ turned from brown into white, which indicates that most likely silver species are being reoxidized to Ag^+ during catalytic conditions, while the color of $AgCHA_{RED400}$ remained almost unaltered. To test this hypothesis, the electronic properties of catalysts before and after reaction are investigated and the resultant spectra are shown in **Figure 5.26b**. The $AgCHA_{RED400}$ catalyst maintains roughly the same UV-Vis spectrum as in the reduced state after reduction, while the spectrum of $AgRHO_{RED400}$ was completely changed after reaction. The band present in reduced sample disappeared giving rise to the formation of typical band at 220 nm characteristic of Ag^+ in exchange positions within the zeolite.[256]

In order to understand the low activity of AgRHO, $AgCHA_{RED100}$ catalyst was evaluated in NH_3 conversion once this sample presented similar UV-Vis spectra as $AgRHO_{RED400}$ and same silver loading as $AgCHA_{RED400}$ so that both parameters can be then compared. Moreover, the catalytic activity of $AgCHA(4.5)_{RED400}$ was also compared since it has similar chemical composition in comparison with AgRHO although they have proven to have different silver species (Ag^0 bulk vs Ag_8 clusters). These results are shown in **Figure 5.27a**.

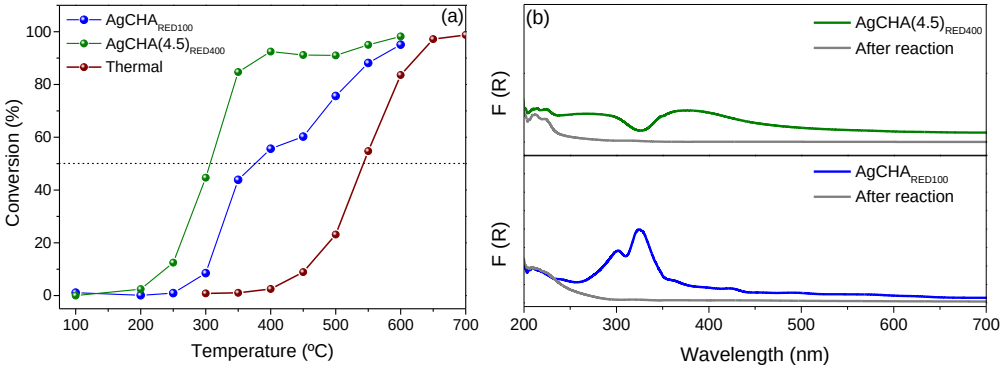

Figure 5.27. Catalytic activity for the SCO-NH_3 reaction of $AgCHA_{RED100}$ and $AgCHA(4.5)_{RED400}$ (a) and respective UV-Vis spectra of the catalysts before and after reaction (b).

NH_3 conversion in the NH_3-SCO reaction for $AgCHA_{RED100}$ and $AgCHA(4.5)_{RED400}$ catalysts demonstrated to be both higher than $AgRHO_{RED400}$. Furthermore, AgCHA(4.5) shows 50% of NH_3 conversion at 300 ºC while for $AgCHA_{RED100}$ it is shifted to higher temperatures (375 ºC). However, the change in solids coloration to white after reaction indicates that silver species were redispersed within the zeolite, which has been further confirmed through UV-Vis spectroscopy. **Figure 5.27b** shows the reestablishment of the band at 220 nm characteristic of silver in extraframework positions. These results suggest that the maintaining of silver species after SCO-NH_3 reaction is strongly dependent on the silver loading.

The Ag_8-type of species observed for all AgRHO-based samples and also seen in $AgCHA_{RED100}$ cannot be undoubtedly

defined as inactive for SCO-NH_3 once $AgCHA_{RED100}$ displays catalytic activity. At the same time, the NH_3 conversion for this catalyst can be explained by the simultaneous presence of silver nanoparticles together with the major part of silver forming clusters, so that the attribution of the active center is difficult in this case. The difference in NH_3 conversion between $AgRHO_{RED400}$ and $AgCHA_{RED100}$ can be ascribed to the silver loading (16 vs 28 wt.%), respectively.

Interestingly, the complete redispersion of silver species in $AgCHA(4.5)_{RED400}$ was not observed during *in situ* XAS experiments using only O_2/He mixture (**Figure 5A.3)**. However, during reaction conditions the reoxidation seems complete, which could be due to an cooperative effect between O_2 and some nitrogen oxides formed as side products, which are known to be efficient in metal redispersion.[270]

Pure Ag powder[271] and Ag^0 supported nanoparticles (Ag/Al_2O_3 and Ag/SiO_2 – 10 wt.% Ag)[272-275] have been used in literature as catalysts for NH_3-SCO leading to 100 % of NH_3 conversion in the same range of low temperature (200-300 ºC) as reported in this work for $AgCHA_{RED400}$. However, in those papers softer reaction conditions (5.5-16.6 mL $NH_3 \cdot s^{-1} \cdot g^{-1}$) were used in comparison to ours (53.3 mL $NH_3 \cdot s^{-1} \cdot g^{-1}$) in terms of GHSV. However, by expressing the space velocity per grams of silver instead of grams of catalyst, the difference is not as great as it looks like by considering the total amount of catalyst,

although it is still significant (ca. 194.4-380.5 mL $NH_3 \cdot s^{-1} \cdot g^{-1}$) in comparison with some reports for Ag/Al_2O_3 (ca. 61.1-166.6 mL $NH_3 \cdot s^{-1} \cdot g^{-1}$), for example. In this sense, our GSHV expressed per grams of Ag is 3-6 times higher than those reported in literature.

Figure 5.28 shows the product distribution (N_2, NO and N_2O) for the NH_3-SCO reaction on Ag-containing zeolites at $T_{50\%}$ and $T_{100\%}$ of NH_3 conversion. The product delivery at 50 % of NH_3 conversion depends on the temperature in which the catalyst reached such conversion. For low temperature conversion, as the case of $AgCHA_{RED400}$ ($T_{50\%}$ = 200 ºC), the N_2O is the main product with 60% of selectivity while the rest is composed by N_2. $AgCHA(4.5)_{RED400}$ also displayed a significant amount of N_2O as product output at $T_{50\%}$ but in less extent respect to $AgCHA_{RED400}$ (52 % of N_2 vs 48 % of N_2O). The difference in selectivity relies on the higher temperature ($T_{50\%}$ = ~300 ºC) required to achieve $T_{50\%}$ of $AgCHA(4.5)_{RED400}$ in comparison with $AgCHA_{RED400}$. The correlation between temperature of conversion with N_2O output was already stated in literature for Ag-based catalysts for SCO-NH_3 and it is explained in terms of thermodynamics of oxidation process.[250] On the other hand, the catalysts where the NH_3 conversion is achieved at much higher temperatures, i.e. $AgRHO_{RED400}$ ($T_{50\%}$ = ~460 ºC) and $AgCHA_{RED100}$ ($T_{50\%}$ = ~380 ºC), reached N_2 selectivities between 80-87 % with consequent formation of

N_2O and also NO, which was not observed in previous catalysts with $T_{50\%}$ lying at lower temperatures. As for N_2O, the formation of NO is also related to the temperature range where the catalyst is working, which, in this case, is favored at >350 ºC. Once $T_{50\%}$ in $AgRHO_{RED400}$ is 100 ºC higher in comparison with that of $AgCHA_{RED100}$, the selectivity to NO is higher in the former (9.8 % vs 3 %, respectively).

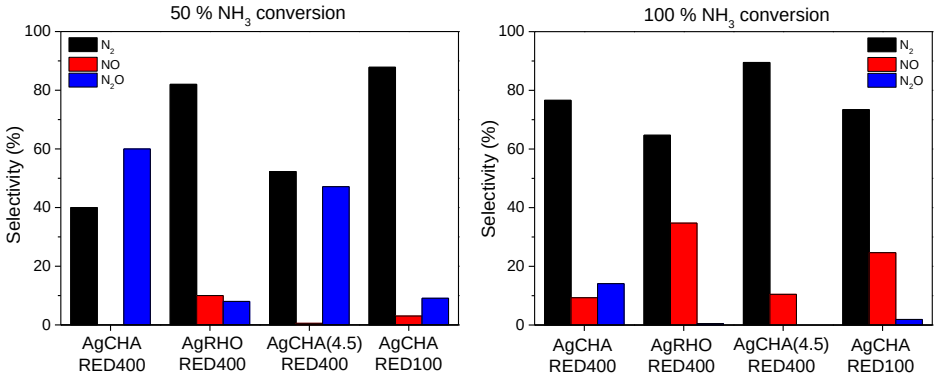

Figure 5.28. Product selectivities obtained at 50 and 100 % NH_3 conversion over Ag-based catalysts.

Furthermore, when NH_3 is fully converted ($T_{100\%}$), N_2 is the main output along with NO, which is present due to high working temperatures. Nevertheless, $AgCHA_{RED400}$ still displays a small amount of N_2O because $T_{100\%}$ is in the range where this product is still thermodynamically favored.

Further efforts are being carried out to design better catalysts (silver alloying with transition metal atoms known to catalyze N_2O reduction/decomposition) to disentangle the

selectivity problem at low temperatures regimes and consequently avoid N_2O formation.

5.2 Conclusions

In this chapter, silver species in different Ag-containing small-pore zeolites (CHA and RHO) were comprehensively followed by the combination of *in situ* XAS with a set of laboratory techniques.

It was shown that silver species with different nuclearity can be formed through thermal treatments under different reactive atmospheres (oxidant, inert and reductive), from cluster to bulk silver. Interestingly, it was demonstrated mainly by XAS and UV-Vis spectroscopies that RHO zeolite seems to play an important role on avoiding silver aggregation until bulk size (under our studied conditions). Moreover, by performed reduction/reoxidation experiments it was shown that the larger the Ag nanoparticles, the more difficult the redispersion of metallic silver to cation-exchange positions is, which is straightly related to the silver loading on Ag-based materials.

The different properties of the silver species of the catalysts are evidenced in their catalytic properties for SCO-NH_3. Our results indicate that at low temperatures, the large Ag^0 particles (AgCHA-based materials) show higher activity, despite the formation of N_2O as side product in this temperature regime. On the other hand, the AgRHO-based materials only show high

NH_3 conversion at high temperatures (~600 ºC) which is really close to the conversion obtained without catalyst (i.e. thermal test).

5.3 Appendix

Table 5A.1. Framework composition of AgCHA and AgRHO before and after *ex situ* activation treatments derived from ^{29}Si MAS NMR.

Sample	Si/Al_{EDS}
AgCHA	2.20
$AgCHA_{reduced}$	2.19
$AgCHA_{oxidized}$	2.10
AgRHO	4.51
$AgRHO_{reduced}$	4.43
$AgRHO_{oxidized}$	4.26

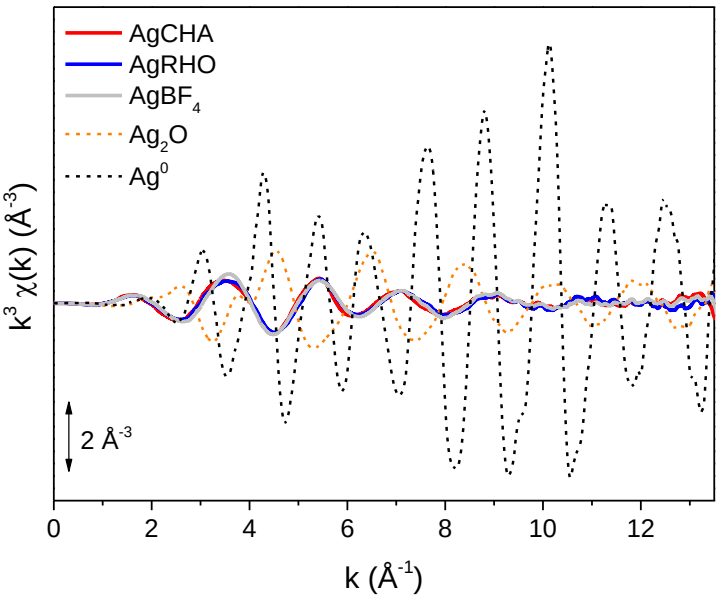

Figure 5A.1. k^3-weighted phase-uncorrected $\chi(k)$ functions of as-made AgCHA and AgRHO zeolites and Ag-based standards.

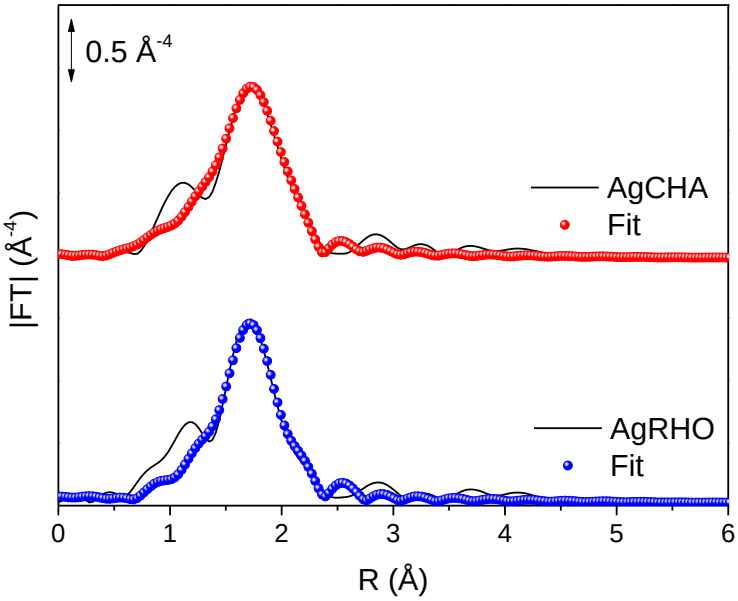

Figure 5A.2. Curve-fittings and |FT| of the k^3-weighted $\chi(k)$ functions of as-made AgCHA and AgRHO zeolites.

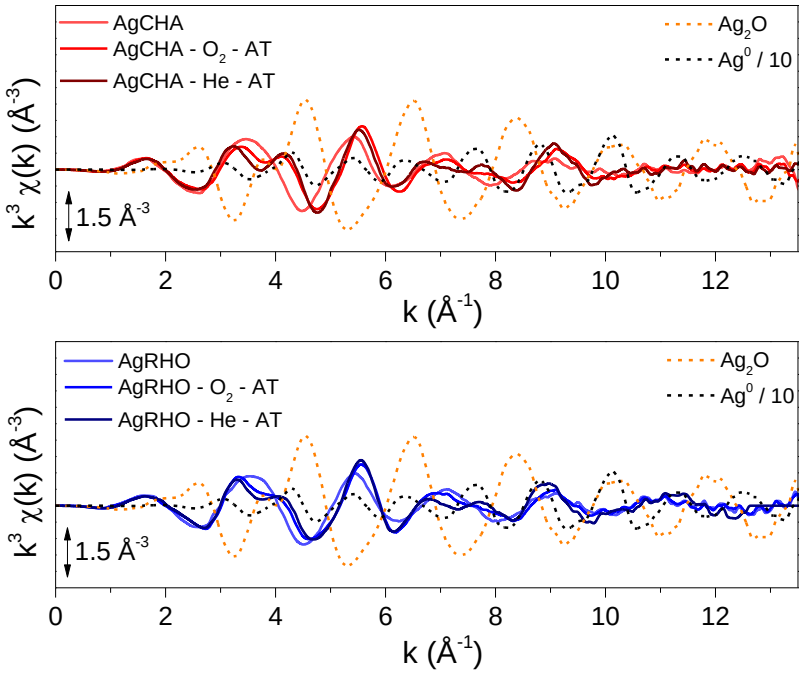

Figure 5A.3. k^3-weighted phase-uncorrected χ(k) functions of AgCHA (top) and AgRHO (bottom) zeolites before and after thermal treatments under oxidative and inert atmospheres.

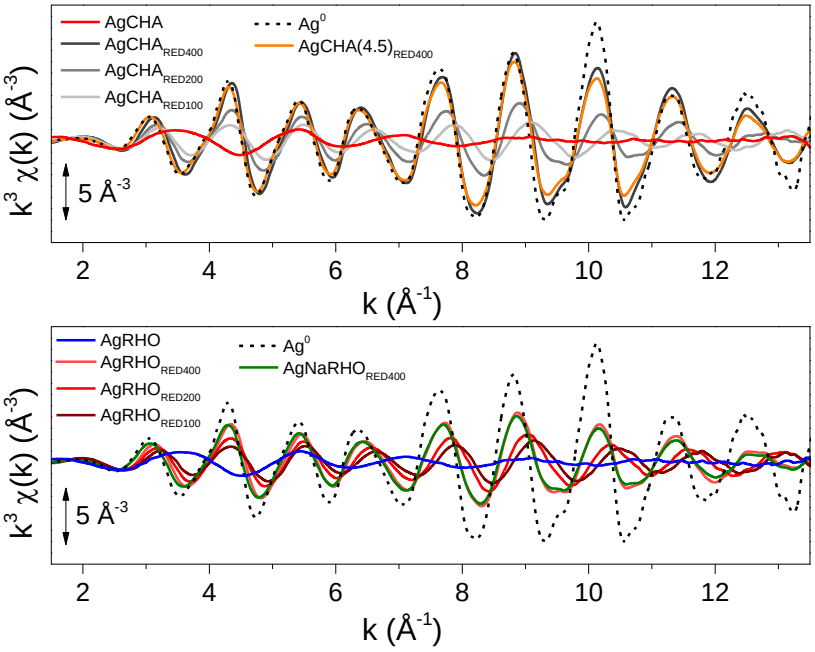

Figure 5A.4. k^3-weighted phase-uncorrected χ(k) functions of AgCHA (top) and AgRHO (bottom) samples after reduction treatments.

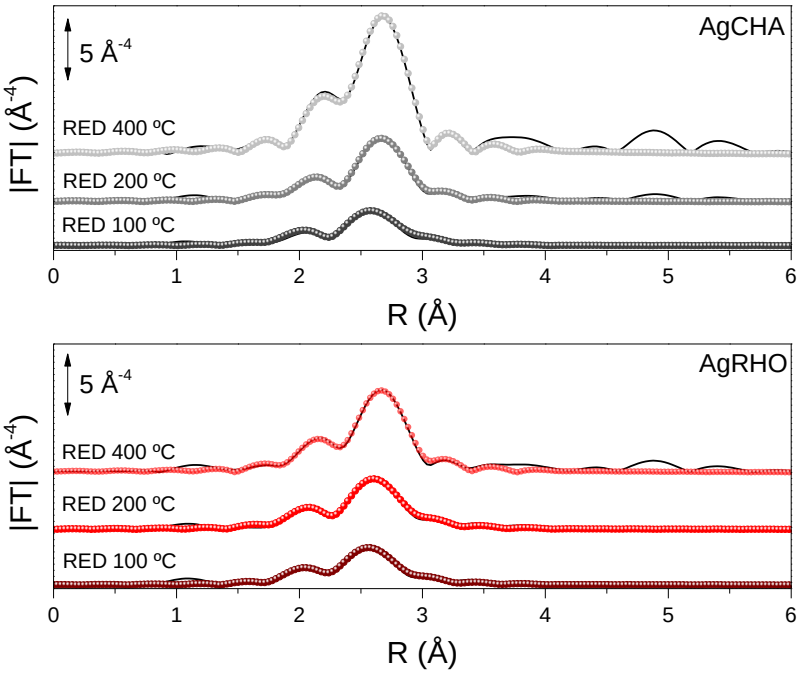

Figure 5A.5. Curve-fittings and |FT| of the k^3-weighted $\chi(k)$ functions of AgCHA (top) and AgRHO (bottom) zeolites reduced at 100, 200 and 400 ºC. Solid lines refer to experimental data while colored circles represent the fits.

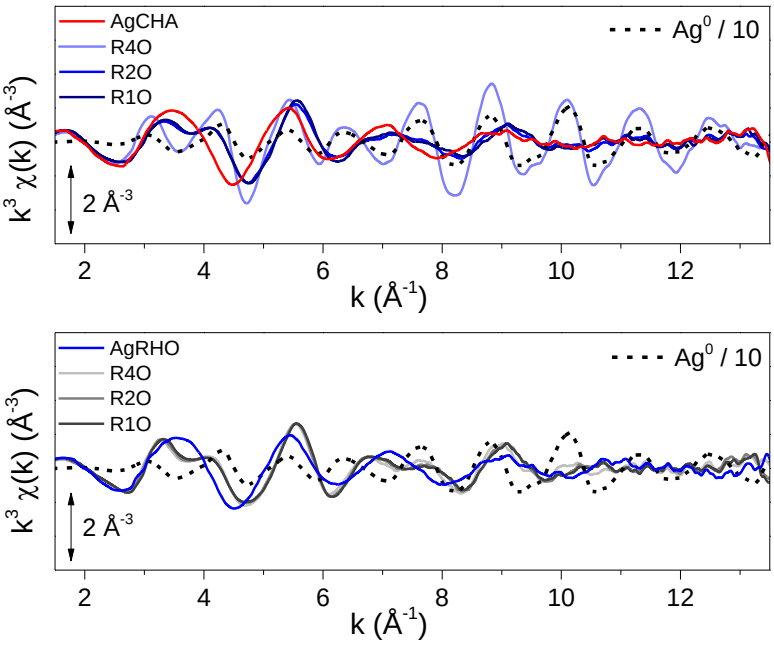

Figure 5A.6. k^3-weighted phase-uncorrected $\chi(k)$ functions of AgCHA (top) and AgRHO (bottom) after subsequent reoxidation treatments.

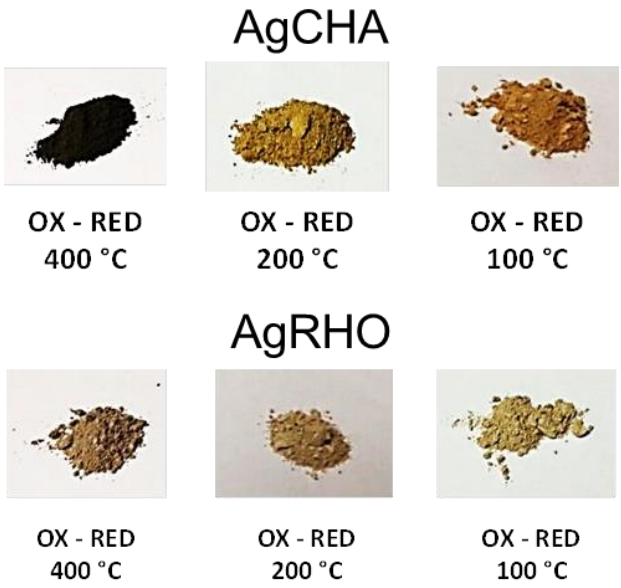

Figure 5A.7. Colors of AgCHA (top) and AgRHO (bottom) samples after reduction and posterior reoxidation process.

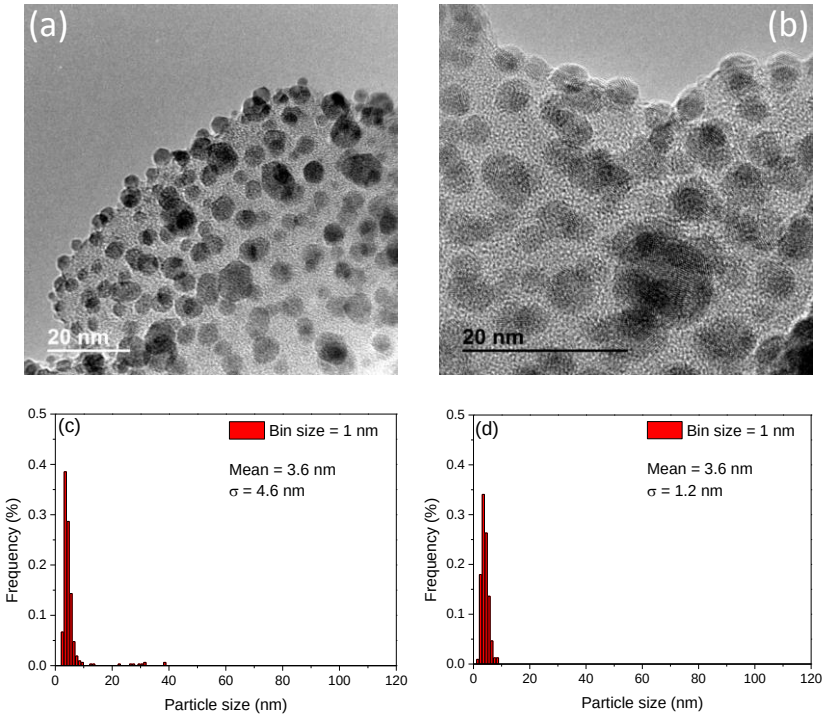

Figure 5A.8. Representative TEM images and particle size distribution of reoxidized (a,c) AgCHA-R4O and (b,d) AgRHO-R4O zeolites, respectively.

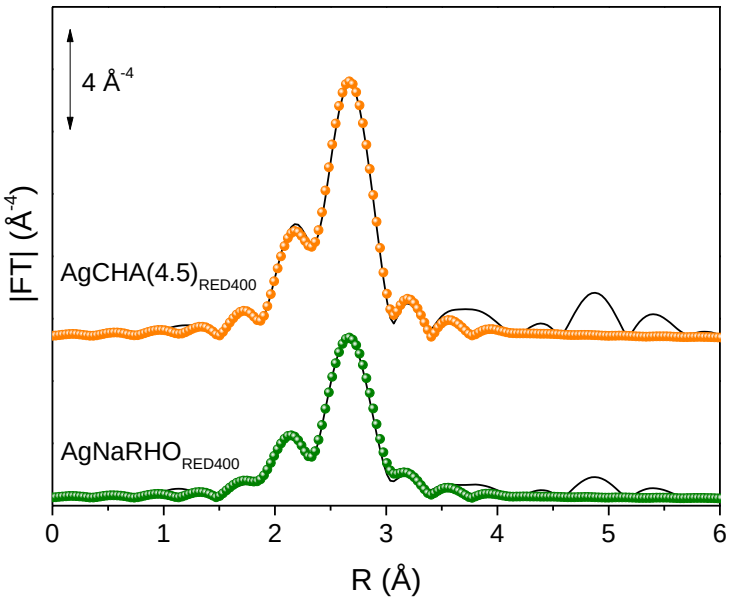

Figure 5A.9. Curve-fittings and |FT| of the k^3-weighted $\chi(k)$ functions of AgCHA(4.5) and AgNaRHO zeolites reduced at 400 ºC. Solid lines refer to experimental data while colored circles represent the fits.

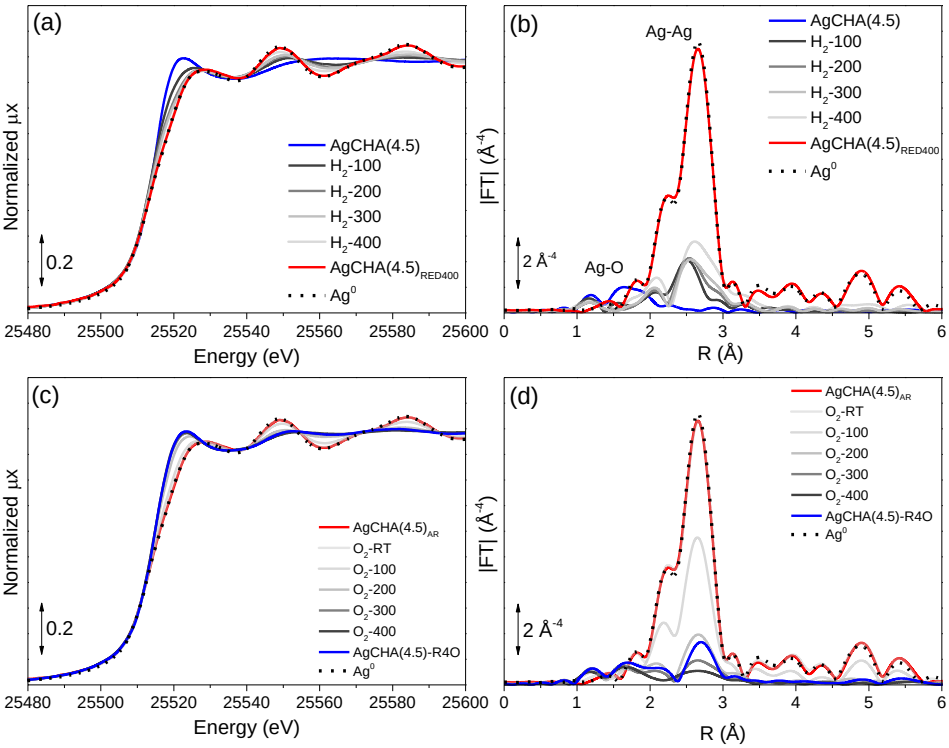

Figure 5A.10. Normalized XANES spectra (left side) and |FT| of the k^3-weighted EXAFS spectra (right side) of reduction (a-b) and reoxidation (b-d) treatments on AgCHA(4.5).

Chapter 6

References

1. Bordiga, S.; Groppo, E.; Agostini, G.; van Bokhoven, J. A.; Lamberti, C., *Chem. Rev.* **2013**, *113* (3), 1736-1850.
2. Gurlo, A.; Riedel, R., *Angew. Chem. Int. Ed.* **2007**, *46* (21), 3826-3848.
3. Abdala, P. M.; Safonova, O. V.; Wiker, G.; van Beek, W.; Emerich, H.; van Bokhoven, J. A.; Sá, J.; Szlachetko, J.; Nachtegaal, M., *CHIMIA International Journal for Chemistry* **2012**, *66* (9), 699-705.
4. Zimina, A.; Dardenne, K.; Denecke, M. A.; Doronkin, D. E.; Huttel, E.; Lichtenberg, H.; Mangold, S.; Pruessmann, T.; Rothe, J.; Spangenberg, T.; Steininger, R.; Vitova, T.; Geckeis, H.; Grunwaldt, J.-D.; A., D. M., *Rev. Sci. Instrum.* **2017**, *88* (11), 113113.
5. Newton, M. A.; Ferri, D.; Smolentsev, G.; Marchionni, V.; Nachtegaal, M., *J. Am. Chem. Soc.* **2016**, *138* (42), 13930-13940.
6. Pascarelli, S.; Mathon, O.; Mairs, T.; Kantor, I.; Agostini, G.; Strohm, C.; Pasternak, S.; Perrin, F.; Berruyer, G.; Chappelet, P.; Clavel, C.; Dominguez, M. C., *J. Synchrotron Radiat.* **2016**, *23* (1), 353-368.
7. Figueroa, S. J. A.; Prestipino, C., *J. Phys. Conf. Ser.* **2016**, *712* (1), 012012.
8. Cassinelli, W. H.; Martins, L.; Passos, A. R.; Pulcinelli, S. H.; Santilli, C. V.; Rochet, A.; Briois, V., *Catal. Today* **2014**, *229*, 114-122.
9. White, R. J.; Luque, R.; Budarin, V. L.; Clark, J. H.; Macquarrie, D. J., *Chem. Soc. Rev.* **2009**, *38* (2), 481-494.
10. Montejano-Carrizales, J. M.; Aguilera-Granja, F.; Morán-López, J. L., *Nanostruct. Mater.* **1997**, *8* (3), 269-287.
11. Agostini, G.; Piovano, A.; Bertinetti, L.; Pellegrini, R.; Leofanti, G.; Groppo, E.; Lamberti, C., *J. Phys. Chem. C* **2014**, *118* (8), 4085-4094.
12. Zhang, Q.; Deng, W.; Wang, Y., *Chem. Commun.* **2011**, *47* (33), 9275-9292.
13. Yang, X.-F.; Wang, A.; Qiao, B.; Li, J.; Liu, J.; Zhang, T., *Acc. Chem. Res.* **2013**, *46* (8), 1740-1748.
14. Tew, M. W.; Nachtegaal, M.; Janousch, M.; Huthwelker, T.; van Bokhoven, J. A., *Phys. Chem. Chem. Phys.* **2012**, *14* (16), 5761-5768.

15. Khodakov, A. Y.; Lynch, J.; Bazin, D.; Rebours, B.; Zanier, N.; Moisson, B.; Chaumette, P., *J. Catal.* **1997**, *168* (1), 16-25.
16. Martínez, A.; Prieto, G.; Rollán, J., *J. Catal.* **2009**, *263* (2), 292-305.
17. Pellegrini, R.; Leofanti, G.; Agostini, G.; Groppo, E.; Lamberti, C., Investigation of carbon and alumina supported Pd catalysts during catalyst preparation. In *Scientific Bases for the Preparation of Heterogeneous Catalysts - Proceedings of the 10th International Symposium, Louvain-la-Neuve, Belgium, July*, **2010**, 437-440.
18. Kang, J. H.; Menard, L. D.; Nuzzo, R. G.; Frenkel, A. I., *J. Am. Chem. Soc.* **2006**, *128* (37), 12068-12069.
19. Meira, D. M.; Ribeiro, R. U.; Mathon, O.; Pascarelli, S.; Bueno, J. M. C.; Zanchet, D., *Appl. Catal., B* **2016**, *197*, 73-85.
20. Bertella, F.; Concepción, P.; Martínez, A., *Catal. Today* **2017**, *289*, 181-191.
21. Bertella, F.; Concepción, P.; Martínez, A., *Catal. Today* **2017**, *296*, 170-180.
22. Shannon, I. J.; Rey, F.; Sankar, G.; Thomas, J. M.; Maschmeyer, T.; Waller, A. M.; Palomares, A. E.; Corma, A.; Dent, A. J.; Greaves, G. N., *J. Chem. Soc., Faraday Trans.* **1996**, *92* (21), 4331-4336.
23. Pellegrini, R.; Agostini, G.; Groppo, E.; Piovano, A.; Leofanti, G.; Lamberti, C., *J. Catal.* **2011**, *280* (2), 150-160.
24. Lazzarini, A.; Piovano, A.; Pellegrini, R.; Leofanti, G.; Agostini, G.; Rudić, S.; Chierotti, M. R.; Gobetto, R.; Battiato, A.; Spoto, G.; Zecchina, A.; Lamberti, C.; Groppo, E., *Catal. Sci. Technol.* **2016**, *6* (13), 4910-4922.
25. Yaseneva, P.; Marti, C. F.; Palomares, E.; Fan, X.; Morgan, T.; Perez, P. S.; Ronning, M.; Huang, F.; Yuranova, T.; Kiwi-Minsker, L.; Derrouiche, S.; Lapkin, A. A., *Chem. Eng. J.* **2014**, *248*, 230-241.
26. Vile, G.; Albani, D.; Nachtegaal, M.; Chen, Z.; Dontsova, D.; Antonietti, M.; Lopez, N.; Perez-Ramirez, J., *Angew. Chem. Int. Ed. Engl.* **2015**, *54* (38), 11265-11269.
27. Lazzarini, A.; Groppo, E.; Agostini, G.; Borfecchia, E.; Giannici, F.; Portale, G.; Longo, A.; Pellegrini, R.; Lamberti, C., *Catal. Today* **2017**, *283*, 144-150.

28. Groppo, E.; Liu, W.; Zavorotynska, O.; Agostini, G.; Spoto, G.; Bordiga, S.; Lamberti, C.; Zecchina, A., *Chem. Mater.* **2010**, *22* (7), 2297-2308.
29. Liu, L.; Diaz, U.; Arenal, R.; Agostini, G.; Concepcion, P.; Corma, A., *Nat. Mater.* **2017**, *16* (1), 132-138.
30. Agostini, G.; Usseglio, S.; Groppo, E.; Uddin, M. J.; Prestipino, C.; Bordiga, S.; Zecchina, A.; Solari, P. L.; Lamberti, C., *Chem. Mater.* **2009**, *21* (7), 1343-1353.
31. Braglia, L.; Borfecchia, E.; Martini, A.; Bugaev, A. L.; Soldatov, A. V.; Oien-Odegaard, S.; Lonstad-Bleken, B. T.; Olsbye, U.; Lillerud, K. P.; Lomachenko, K. A.; Agostini, G.; Manzoli, M.; Lamberti, C., *Phys. Chem. Chem. Phys.* **2017**, *19* (40), 27489-27507.
32. Meilikhov, M.; Yusenko, K.; Esken, D.; Turner, S.; Van Tendeloo, G.; Fischer, R. A., *Eur. J. Inorg. Chem.* **2010**, *2010* (24), 3701-3714.
33. Prieto, G.; Martínez, A.; Murciano, R.; Arribas, M. A., *Appl. Catal., A* **2009**, *367* (1-2), 146-156.
34. Shimizu, K.; Koizumi, S.; Hatamachi, T.; Yoshida, H.; Komai, S.; Kodama, T.; Kitayama, Y., *J. Catal.* **2004**, *228* (1), 141-151.
35. Detoni, C.; Bertella, F.; Souza, M. M. V. M.; Pergher, S. B. C.; Aranda, D. A. G., *Appl. Clay Sci.* **2014**, *95*, 388-395.
36. Liu, X.; Liu, M. H.; Luo, Y. C.; Mou, C. Y.; Lin, S. D.; Cheng, H.; Chen, J. M.; Lee, J. F.; Lin, T. S., *J. Am. Chem. Soc.* **2012**, *134* (24), 10251-10258.
37. Munnik, P.; de Jongh, P. E.; de Jong, K. P., *Chem. Rev.* **2015**, *115* (14), 6687-6718.
38. Toebes, M. L.; van Dillen, J. A.; de Jong, K. P., *J. Mol. Catal. A: Chem.* **2001**, *173* (1-2), 75-98.
39. Lopes, C. W.; Cerrillo, J. L.; Palomares, A. E.; Rey, F.; Agostini, G., *Phys. Chem. Chem. Phys.* **2018**, *20* (18), 12700-12709.
40. Lamberti, C.; Zecchina, A.; Groppo, E.; Bordiga, S., *Chem. Soc. Rev.* **2010**, *39* (12), 4951-5001.
41. Frenkel, A. I., *Chem. Soc. Rev.* **2012**, *41* (24), 8163-8178.

42. Bus, E.; Miller, J. T.; Kropf, A. J.; Prins, R.; van Bokhoven, J. A., *Phys. Chem. Chem. Phys.* **2006**, *8* (27), 3248-3258.
43. Nashner, M. S.; Frenkel, A. I.; Adler, D. L.; Shapley, J. R.; Nuzzo, R. G., *J. Am. Chem. Soc.* **1997**, *119* (33), 7760-7771.
44. de Graaf, J.; van Dillen, A. J.; de Jong, K. P.; Koningsberger, D. C., *J. Catal.* **2001**, *203* (2), 307-321.
45. Matos, J.; Ono, L. K.; Behafarid, F.; Croy, J. R.; Mostafa, S.; DeLaRiva, A. T.; Datye, A. K.; Frenkel, A. I.; Roldan Cuenya, B., *Phys. Chem. Chem. Phys.* **2012**, *14* (32), 11457-11467.
46. Wang, J.; Wang, Q.; Jiang, X.; Liu, Z.; Yang, W.; Frenkel, A. I., *J. Phys. Chem. C* **2015**, *119* (1), 854-861.
47. Frenkel, A. I.; Hills, C. W.; Nuzzo, R. G., *J. Phys. Chem. B* **2001**, *105* (51), 12689-12703.
48. Zhang, H.; Liu, G.; Shi, L.; Ye, J., *ADV Energy Mater.* **2018**, *8* (1), 1701343.
49. Zhu, Y.; An, Z.; He, J., *J. Catal.* **2016**, *341*, 44-54.
50. Zhang, Z.; Zhu, Y.; Asakura, H.; Zhang, B.; Zhang, J.; Zhou, M.; Han, Y.; Tanaka, T.; Wang, A.; Zhang, T.; Yan, N., *Nat. Commun.* **2017**, *8*, 16100.
51. Zhang, S.; Tang, Y.; Nguyen, L.; Zhao, Y.-F.; Wu, Z.; Goh, T.-W.; Liu, J. J.; Li, Y.; Zhu, T.; Huang, W.; Frenkel, A. I.; Li, J.; Tao, F. F., *ACS Catal.* **2018**, *8* (1), 110-121.
52. Zhang, M.; Wang, Y.-G.; Chen, W.; Dong, J.; Zheng, L.; Luo, J.; Wan, J.; Tian, S.; Cheong, W.-C.; Wang, D.; Li, Y., *J. Am. Chem. Soc.* **2017**, *139* (32), 10976-10979.
53. Yang, S.; Tak, Y. J.; Kim, J.; Soon, A.; Lee, H., *ACS Catal.* **2017**, *7* (2), 1301-1307.
54. Yan, H.; Lin, Y.; Wu, H.; Zhang, W.; Sun, Z.; Cheng, H.; Liu, W.; Wang, C.; Li, J.; Huang, X.; Yao, T.; Yang, J.; Wei, S.; Lu, J., *Nat. Commun.* **2017**, *8* (1), 1070.
55. Wei, H.; Liu, X.; Wang, A.; Zhang, L.; Qiao, B.; Yang, X.; Huang, Y.; Miao, S.; Liu, J.; Zhang, T., *Nat. Commun.* **2014**, *5*, 5634.
56. Qiao, B.; Wang, A.; Yang, X.; Allard, L. F.; Jiang, Z.; Cui, Y.; Liu, J.; Li, J.; Zhang, T., *Nat. Chem.* **2011**, *3*, 634-641.

57. Lin, J.; Wang, A.; Qiao, B.; Liu, X.; Yang, X.; Wang, X.; Liang, J.; Li, J.; Liu, J.; Zhang, T., *J. Am. Chem. Soc.* **2013**, *135* (41), 15314-15317.
58. Huang, Z.; Gu, X.; Cao, Q.; Hu, P.; Hao, J.; Li, J.; Tang, X., *Angew. Chem. Int. Ed.* **2012**, *51* (17), 4198-4203.
59. Fei, H.; Dong, J.; Feng, Y.; Allen, C. S.; Wan, C.; Volosskiy, B.; Li, M.; Zhao, Z.; Wang, Y.; Sun, H.; An, P.; Chen, W.; Guo, Z.; Lee, C.; Chen, D.; Shakir, I.; Liu, M.; Hu, T.; Li, Y.; Kirkland, A. I.; Duan, X.; Huang, Y., *Nat. Catal.* **2018**, *1* (1), 63-72.
60. Ahn, H. S.; Yano, J.; Tilley, T. D., *ACS Catal.* **2015**, *5* (4), 2573-2576.
61. Li, X.; Bi, W.; Zhang, L.; Tao, S.; Chu, W.; Zhang, Q.; Luo, Y.; Wu, C.; Xie, Y., *Adv. Mater.* **2016**, *28* (12), 2427-2431.
62. Yang, S.; Kim, J.; Tak, Y. J.; Soon, A.; Lee, H., *Angew. Chem. Int. Ed.* **2016**, *55* (6), 2058-2062.
63. Nie, L.; Mei, D.; Xiong, H.; Peng, B.; Ren, Z.; Hernandez, X. I. P.; DeLaRiva, A.; Wang, M.; Engelhard, M. H.; Kovarik, L.; Datye, A. K.; Wang, Y., *Science* **2017**, *358* (6369), 1419-1423.
64. Yin, P.; Yao, T.; Wu, Y.; Zheng, L.; Lin, Y.; Liu, W.; Ju, H.; Zhu, J.; Hong, X.; Deng, Z.; Zhou, G.; Wei, S.; Li, Y., *Angew. Chem. Int. Ed.* **2016**, *55* (36), 10800-10805.
65. Morgan, K.; Goguet, A.; Hardacre, C., *ACS Catal.* **2015**, *5* (6), 3430-3445.
66. Berndt, H.; Richter, M.; Gerlach, T.; Baerns, M., *J. Chem. Soc., Faraday Trans.* **1998**, *94* (14), 2043-2046.
67. Shimizu, K.-i.; Sugino, K.; Kato, K.; Yokota, S.; Okumura, K.; Satsuma, A., *J. Phys. Chem. C* **2007**, *111* (4), 1683-1688.
68. Mathisen, K.; Nilsen, M. H.; Nordhei, C.; Nicholson, D. G., *J. Phys. Chem. C* **2012**, *116* (1), 171-184.
69. Moliner, M.; Gabay, J. E.; Kliewer, C. E.; Carr, R. T.; Guzman, J.; Casty, G. L.; Serna, P.; Corma, A., *J. Am. Chem. Soc.* **2016**, *138* (48), 15743-15750.
70. An, K.; Somorjai, G. A., *ChemCatChem* **2012**, *4* (10), 1512-1524.
71. Ye, R.; Hurlburt, T. J.; Sabyrov, K.; Alayoglu, S.; Somorjai, G. A., *P. Natl. Acad. Sci.* **2016**, *113* (19), 5159-5166.

72. Peng, Z.; Yang, H., *Nano Today* **2009**, *4* (2), 143-164.
73. Ghosh Chaudhuri, R.; Paria, S., *Chem. Rev.* **2012**, *112* (4), 2373-433.
74. Kobayashi, H.; Kusada, K.; Kitagawa, H., *Acc. Chem. Res.* **2015**, *48* (6), 1551-1559.
75. Kusada, K.; Kobayashi, H.; Ikeda, R.; Kubota, Y.; Takata, M.; Toh, S.; Yamamoto, T.; Matsumura, S.; Sumi, N.; Sato, K.; Nagaoka, K.; Kitagawa, H., *J. Am. Chem. Soc.* **2014**, *136* (5), 1864-1871.
76. Kusada, K.; Yamauchi, M.; Kobayashi, H.; Kitagawa, H.; Kubota, Y., *J. Am. Chem. Soc.* **2010**, *132* (45), 15896-15898.
77. Frenkel, A. I.; Stern, E. A.; Voronel, A.; Heald, S. M., *Solid State Commun.* **1996**, *99* (2), 67-71.
78. Alayoglu, S.; Zavalij, P.; Eichhorn, B.; Wang, Q.; Frenkel, A. I.; Chupas, P., *ACS Nano* **2009**, *3* (10), 3127-3137.
79. Frenkel, A., *Z. Krist-Cryst Mater.* **2007**, *222* (11/2007), 605–611.
80. Hwang, B.-J.; Sarma, L. S.; Chen, J.-M.; Chen, C.-H.; Shih, S.-C.; Wang, G.-R.; Liu, D.-G.; Lee, J.-F.; Tang, M.-T., *J. Am. Chem. Soc.* **2005**, *127* (31), 11140-11145.
81. Nashner, M. S.; Frenkel, A. I.; Somerville, D.; Hills, C. W.; Shapley, J. R.; Nuzzo, R. G., *J. Am. Chem. Soc.* **1998**, *120* (32), 8093-8101.
82. Goel, S.; Wu, Z.; Zones, S. I.; Iglesia, E., *J. Am. Chem. Soc.* **2012**, *134* (42), 17688-17695.
83. Goel, S.; Zones, S. I.; Iglesia, E., *J. Am. Chem. Soc.* **2014**, *136* (43), 15280-15290.
84. Otto, T.; Zones, S. I.; Iglesia, E., *J. Catal.* **2016**, *339*, 195-208.
85. Wu, Z.; Goel, S.; Choi, M.; Iglesia, E., *J. Catal.* **2014**, *311*, 458-468.
86. Otto, T.; Ramallo-López, J. M.; Giovanetti, L. J.; Requejo, F. G.; Zones, S. I.; Iglesia, E., *J. Catal.* **2016**, *342*, 125-137.
87. Colella, C.; Gualtieri, A. F., *Microporous Mesoporous Mater.* **2007**, *105* (3), 213-221.
88. Davis, M. E., *Ind. Eng. Chem. Res.* **1991**, *30* (8), 1675-1683.

89. Baerlocher, C.; McCusker, L. B.; Olson, D. H., Introduction and explanatory notes. In *Atlas of Zeolite Framework Types (Sixth Edition)*, Elsevier Science B.V.: Amsterdam, **2007**, 3-11.
90. Szostak, R., *Molecular Sieves: Principles of Synthesis and Identification*. Springer Netherlands: **2013**.
91. Dann, S. E.; Mead, P. J.; Weller, M. T., *Inorg. Chem.* **1996**, *35* (6), 1427-1428.
92. Pace, G. G., *Zeolitas: características, propiedades y aplicaciones industriales*. Editorial Innovacín Tecnológica, Facultad de Ingeniería, UCV: **2000**.
93. Weitkamp, J., *Solid State Ionics* **2000**, *131* (1-2), 175-188.
94. International Zeolite Association (IZA) webpage. http://www.iza-structure.org/databases/ (accessed 03/06/2018).
95. Taramasso, M. P., G.; Notari, B. U.S. Patent 4410501. **1983**.
96. Notari, B., *Catal. Today* **1993**, *18* (2), 163-172.
97. Moliner, M.; Corma, A., *Microporous Mesoporous Mater.* **2014**, *189* (Supplement C), 31-40.
98. Moliner, M.; Rey, F.; Corma, A., *Angew. Chem. Int. Ed. Engl.* **2013**, *52* (52), 13880-13889.
99. Moliner, M., *Dalton Trans.* **2014**, *43* (11), 4197-4208.
100. Luo, H. Y.; Lewis, J. D.; Roman-Leshkov, Y., *Annu. Rev. Chem. Biomol.* **2016**, *7*, 663-692.
101. Bordiga, S.; Coluccia, S.; Lamberti, C.; Marchese, L.; Zecchina, A.; Boscherini, F.; Buffa, F.; Genoni, F.; Leofanti, G.; Petrini, G.; Vlaic, G., *J. Phys. Chem.* **1994**, *98*, 4125-4132.
102. Bordiga, S.; Boscherini, F.; Coluccia, S.; Genonic, F.; Lamberti, C.; Leofanti, G.; Marchese, L.; Petrini, G.; Vlaic, G.; Zecchina, A., *Catal. Lett.* **1994**, *26* (1), 195-208.
103. Huybrechts, D. R. C.; Bruycker, L. D.; Jacobs, P. A., *Nature* **1990**, *345*, 240-242.
104. Huybrechts, D. R. C.; Vaesen, I.; Li, H. X.; Jacobs, P. A., *Catal. Lett.* **1991**, *8* (2), 237-244.
105. Behrens, P.; Felsche, J.; Vetter, S.; Schulz-Ekloff, G.; Jaeger, N. I.; Niemann, W., *J. Chem. Soc., Chem. Commun.* **1991**, (10), 678-680.

106. Trong On, D.; Bittar, A.; Sayari, A.; Kaliaguine, S.; Bonneviot, L., *Catal. Lett.* **1992**, *16* (1), 85-95.
107. Ito, T.; Kanai, H.; Nakai, T.; Imamura, S., *React. Kinet. Catal. Lett.* **1994**, *52* (2), 421-428.
108. Davis, R. J.; Liu, Z.; Tabora, J. E.; Wieland, W. S., *Catal. Lett.* **1995**, *34* (1), 101-113.
109. Sankar, G.; Bell, R. G.; Thomas, J. M.; Anderson, M. W.; Wright, P. A.; Rocha, J., *J. Phys. Chem.* **1996**, *100* (2), 449-452.
110. Prestipino, C.; Solari, P. L.; Lamberti, C., *J. Phys. Chem. B* **2005**, *109* (27), 13132-13137.
111. Lamberti, C.; Palomino, G. T.; Bordiga, S.; Arduino, D.; Zecchina, A.; Vlaic, G., *Jpn. J. Appl. Phys.* **1999**, *38* (S1), 55-58.
112. Lamberti, C.; Bordiga, S.; Arduino, D.; Zecchina, A.; Geobaldo, F.; Spano, G.; Genoni, F.; Petrini, G.; Carati, A.; Villain, F.; Vlaic, G., *J. Phys. Chem. B* **1998**, *102*, 6382-6390.
113. Bordiga, S.; Bonino, F.; Damin, A.; Lamberti, C., *Phys. Chem. Chem. Phys.* **2007**, *9* (35), 4854-4878.
114. Berlier, G.; Spoto, G.; Fisicaro, P.; Bordiga, S.; Zecchina, A.; Giamello, E.; Lamberti, C., *Microchem. J.* **2002**, *71* (2), 101-116.
115. Lamberti, C.; Turnes Palomino, G.; Bordiga, S.; Zecchina, A.; Spanò, G.; Otero Areán, C., *Catal. Lett.* **1999**, *63* (3), 213-216.
116. Corma, A.; Nemeth, L. T.; Renz, M.; Valencia, S., *Nature* **2001**, *412* (6845), 423-425.
117. Bare, S. R.; Kelly, S. D.; Sinkler, W.; Low, J. J.; Modica, F. S.; Valencia, S.; Corma, A.; Nemeth, L. T., *J. Am. Chem. Soc.* **2005**, *127* (37), 12924-12932.
118. Dijkmans, J.; Dusselier, M.; Janssens, W.; Trekels, M.; Vantomme, A.; Breynaert, E.; Kirschhock, C.; Sels, B. F., *ACS Catal.* **2016**, *6* (1), 31-46.
119. Al-Nayili, A.; Yakabi, K.; Hammond, C., *J. Mater. Chem. A* **2016**, *4* (4), 1373-1382.
120. Hammond, C.; Padovan, D.; Al-Nayili, A.; Wells, P. P.; Gibson, E. K.; Dimitratos, N., *ChemCatChem* **2015**, *7* (20), 3322-3331.

121. Corma, A.; Llabrés i Xamena, F. X.; Prestipino, C.; Renz, M.; Valencia, S., *J. Phys. Chem. C* **2009**, *113* (26), 11306-11315.
122. Mafra, L.; Vidal-Moya, J. A.; Blasco, T., Structural Characterization of Zeolites by Advanced Solid State NMR Spectroscopic Methods. In *Annual Reports on NMR Spectroscopy Volume 77*, **2012**, 259-351.
123. van Bokhoven, J. A.; Lamberti, C., *Coord. Chem. Rev.* **2014**, *277-278*, 275-290.
124. Agostini, G.; Lamberti, C.; Palin, L.; Milanesio, M.; Danilina, N.; Xu, B.; Janousch, M.; van Bokhoven, J. A., *J. Am. Chem. Soc.* **2010**, *132* (2), 667-678.
125. Pappas, D. K.; Borfecchia, E.; Dyballa, M.; Pankin, I. A.; Lomachenko, K. A.; Martini, A.; Signorile, M.; Teketel, S.; Arstad, B.; Berlier, G.; Lamberti, C.; Bordiga, S.; Olsbye, U.; Lillerud, K. P.; Svelle, S.; Beato, P., *J. Am. Chem. Soc.* **2017**, *139* (42), 14961-14975.
126. Ono, Y.; Baba, T., *Phys. Chem. Chem. Phys.* **2015**, *17* (24), 15637-15654.
127. Farrusseng, D.; Tuel, A., *New J. Chem.* **2016**, *40* (5), 3933-3949.
128. Baba, T.; Akinaka, N.; Nomura, M.; Ono, Y., *J. Chem. Soc., Faraday Trans.* **1993**, *89* (3), 595-599.
129. Baldansuren, A.; Dilger, H.; Eichel, R. d.-A.; van Bokhoven, J. A.; Roduner, E., *J. Phys. Chem. C* **2009**, *113* (45), 19623-19632.
130. Coutino-Gonzalez, E.; Baekelant, W.; Steele, J. A.; Kim, C. W.; Roeffaers, M. B. J.; Hofkens, J., *Acc. Chem. Res.* **2017**, *50* (9), 2353-2361.
131. Martínez-Franco, R.; Moliner, M.; Corma, A., *J. Catal.* **2014**, *319*, 36-43.
132. Moliner, M.; Franch, C.; Palomares, E.; Grill, M.; Corma, A., *Chem. Commun.* **2012**, *48* (66), 8264-8266.
133. Beale, A. M.; Gao, F.; Lezcano-Gonzalez, I.; Peden, C. H.; Szanyi, J., *Chem. Soc. Rev.* **2015**, *44* (20), 7371-7405.
134. Franch-Martí, C.; Alonso-Escobar, C.; Jorda, J. L.; Peral, I.; Hernández-Fenollosa, J.; Corma, A.; Palomares, A. E.; Rey, F.; Guilera, G., *J. Catal.* **2012**, *295*, 22-30.

135. Gunter, T.; Carvalho, H. W.; Doronkin, D. E.; Sheppard, T.; Glatzel, P.; Atkins, A. J.; Rudolph, J.; Jacob, C. R.; Casapu, M.; Grunwaldt, J. D., *Chem. Commun.* **2015**, *51* (44), 9227-9230.
136. Martín, N.; Vennestrøm, P. N. R.; Thøgersen, J. R.; Moliner, M.; Corma, A., *Chemistry – A European Journal* **2017**, *23* (54), 13404-13414.
137. Martín, N.; Vennestrøm, P. N. R.; Thøgersen, J. R.; Moliner, M.; Corma, A., *ChemCatChem* **2017**, *9* (10), 1754-1757.
138. van Bokhoven, J. A.; Lamberti, C., XAS Techniques to Determine Catalytically Active Sites in Zeolites: The Case of Cu-Zeolites. In *XAFS Techniques for Catalysts, Nanomaterials, and Surfaces*, **2017**, 299-316.
139. Martínez-Franco, R.; Moliner, M.; Concepcion, P.; Thogersen, J. R.; Corma, A., *J. Catal.* **2014**, *314*, 73-82.
140. Martínez-Franco, R.; Moliner, M.; Franch, C.; Kustov, A.; Corma, A., *Appl. Catal., B* **2012**, *127*, 273-280.
141. Martínez-Franco, R.; Moliner, M.; Thogersen, J. R.; Corma, A., *ChemCatChem* **2013**, *5* (11), 3316-3323.
142. Fickel, D. W.; Lobo, R. F., *J. Phys. Chem. C* **2010**, *114* (3), 1633-1640.
143. Korhonen, S. T.; Fickel, D. W.; Lobo, R. F.; Weckhuysen, B. M.; Beale, A. M., *Chem. Commun.* **2011**, *47* (2), 800-802.
144. Deka, U.; Juhin, A.; Eilertsen, E. A.; Emerich, H.; Green, M. A.; Korhonen, S. T.; Weckhuysen, B. M.; Beale, A. M., *J. Phys. Chem. C* **2012**, *116* (7), 4809-4818.
145. McEwen, J. S.; Anggara, T.; Schneider, W. F.; Kispersky, V. F.; Miller, J. T.; Delgass, W. N.; Ribeiro, F. H., *Catal. Today* **2012**, *184* (1), 129-144.
146. Borfecchia, E.; Lomachenko, K. A.; Giordanino, F.; Falsig, H.; Beato, P.; Soldatov, A. V.; Bordiga, S.; Lamberti, C., *Chem. Sci.* **2015**, *6* (1), 548-563.
147. Turnes Palomino, G.; Fisicaro, P.; Bordiga, S.; Zecchina, A.; Giamello, E.; Lamberti, C., *J. Phys. Chem. B* **2000**, *104* (17), 4064-4073.

148. Giordanino, F.; Vennestrom, P. N. R.; Lundegaard, L. F.; Stappen, F. N.; Mossin, S.; Beato, P.; Bordiga, S.; Lamberti, C., *Dalton Trans.* **2013**, *42* (35), 12741-12761.
149. Janssens, T. V. W.; Falsig, H.; Lundegaard, L. F.; Vennestrøm, P. N. R.; Rasmussen, S. B.; Moses, P. G.; Giordanino, F.; Borfecchia, E.; Lomachenko, K. A.; Lamberti, C.; Bordiga, S.; Godiksen, A.; Mossin, S.; Beato, P., *ACS Catal.* **2015**, *5* (5), 2832-2845.
150. Paolucci, C.; Khurana, I.; Parekh, A. A.; Li, S.; Shih, A. J.; Li, H.; Di Iorio, J. R.; Albarracin-Caballero, J. D.; Yezerets, A.; Miller, J. T.; Delgass, W. N.; Ribeiro, F. H.; Schneider, W. F.; Gounder, R., *Science* **2017**, *357* (6354), 898-903.
151. Yamamoto, T.; Takenaka, S.; Tanaka, T.; Baba, T., *J. Phys. Conf. Ser.* **2009**, *190*.
152. Baba, T.; Sawada, H.; Takahashi, T.; Abe, M., *Appl. Catal., A* **2002**, *231* (1-2), 55-63.
153. Baba, T.; Sawada, H., *Phys. Chem. Chem. Phys.* **2002**, *4* (15), 3919-3923.
154. Baba, T.; Komatsu, N.; Sawada, H.; Yamaguchi, Y.; Takahashi, T.; Sugisawa, H.; Ono, Y., *Langmuir* **1999**, *15* (23), 7894-7896.
155. Baba, T.; Akinaka, N.; Nomura, M.; Ono, Y., *J. Chem. Soc., Chem. Commun.* **1992**, (4), 339-340.
156. Baba, T.; Abe, Y., *Appl. Catal., A* **2003**, *250* (2), 265-270.
157. Lamberti, C.; Prestipino, C.; Bordiga, S.; Fitch, A. N.; Marra, G. L., *Nucl. Instrum. Meth. B* **2003**, *200*, 155-159.
158. Shibata, J.; Takada, Y.; Shichi, A.; Satokawa, S.; Satsuma, A.; Hattori, T., *J. Catal.* **2004**, *222* (2), 368-376.
159. Gellens, L. R.; Mortier, W. J.; Uytterhoeven, J. B., *Zeolites* **1981**, *1* (1), 11-18.
160. Kim, Y.; Seff, K., *J. Am. Chem. Soc.* **1978**, *100* (22), 6989-6997.
161. Miyanaga, T.; Hoshino, H.; Endo, H.; Sakane, H., *J. Synchrotron Radiat.* **1999**, *6*, 442-444.
162. Shimizu, K.; Sawabe, K.; Satsuma, A., *Catal. Sci. Technol.* **2011**, *1* (3), 331–341.

163. Shibata, J.; Shimizu, K.-i.; Takada, Y.; Shichi, A.; Yoshida, H.; Satokawa, S.; Satsuma, A.; Hattori, T., *J. Catal.* **2004**, *227* (2), 367-374.
164. Suzuki, Y.; Matsumoto, N.; Ainai, T.; Miyanaga, T.; Hoshino, H., *Polyhedron* **2005**, *24* (5), 685-691.
165. Lozinska, M. M.; Mowat, J. P. S.; Wright, P. A.; Thompson, S. P.; Jorda, J. L.; Palomino, M.; Valencia, S.; Rey, F., *Chem. Mater.* **2014**, *26* (6), 2052-2061.
166. Chatelain, T.; Patarin, J.; Fousson, E.; Soulard, M.; Guth, J. L.; Schulz, P., *Microporous Mater.* **1995**, *4* (2-3), 231-238.
167. Fischer, M., *Phys. Chem. Chem. Phys.* **2016**, *18* (23), 15738-15750.
168. Shang, J.; Li, G.; Singh, R.; Gu, Q.; Nairn, K. M.; Bastow, T. J.; Medhekar, N.; Doherty, C. M.; Hill, A. J.; Liu, J. Z.; Webley, P. A., *J. Am. Chem. Soc.* **2012**, *134* (46), 19246-19253.
169. Shang, J.; Li, G.; Singh, R.; Xiao, P.; Liu, J. Z.; Webley, P. A., *J. Phys. Chem. C* **2013**, *117* (24), 12841-12847.
170. Li, Z.; Martínez-Triguero, J.; Yu, J.; Corma, A., *J. Catal.* **2015**, *329*, 379-388.
171. Moliner, M.; Martínez, C.; Corma, A., *Chem. Mater.* **2014**, *26* (1), 246-258.
172. Ridha, F. N.; Yang, Y.; Webley, P. A., *Microporous Mesoporous Mater.* **2009**, *117* (1-2), 497-507.
173. Zones, S. I., *J. Chem. Soc., Faraday Trans.* **1991**, *87* (22), 3709-3716.
174. Brunauer, S.; Emmett, P. H.; Teller, E., *J. Am. Chem. Soc.* **1938**, *60* (2), 309-319.
175. Sing, K. S. W.; Rouquerol, F.; Llewellyn, P.; Rouquerol, J., Assessment of Microporosity. In *Adsorption by Powders and Porous Solids*, **2014**, 303-320.
176. Sing, K. S. W.; Rouquerol, F.; Rouquerol, J.; Llewellyn, P., Assessment of Mesoporosity. In *Adsorption by Powders and Porous Solids*, **2014**, 269-302.
177. Anderson, J. R.; Pratt, K. C., *Introduction to characterization and testing of catalysts*. Academic Press: **1985**.
178. Weckhuysen, B. M., *In-situ Spectroscopy of Catalysts*. American Scientific Publishers: **2004**.
179. Calvin, S., *XAFS for Everyone*. Taylor & Francis: **2013**.

180. Diamond Light Source. http://www.diamond.ac.uk/Science/Machine/Components.html (accessed 13/12/2017).
181. Garino, C.; Borfecchia, E.; Gobetto, R.; van Bokhoven, J. A.; Lamberti, C., *Coord. Chem. Rev.* **2014**, *277-278*, 130-186.
182. Willmott, P., The Interaction of X-rays with Matter. In *An Introduction to Synchrotron Radiation*, John Wiley & Sons, Ltd: **2011**, 15-37.
183. Balerna, A.; Mobilio, S., Introduction to Synchrotron Radiation. In *Synchrotron Radiation: Basics, Methods and Applications*, Mobilio, S.; Boscherini, F.; Meneghini, C., Eds. Springer Berlin Heidelberg: Berlin, Heidelberg, **2015**, 3-28.
184. Bunker, G., *Introduction to XAFS: A Practical Guide to X-ray Absorption Fine Structure Spectroscopy*. Cambridge University Press: **2010**.
185. Bergmann, U.; Glatzel, P., *Photosynth. Res.* **2009**, *102* (2-3), 255-266.
186. Gates, W. P., Chapter 12.3 X-ray Absorption Spectroscopy. In *Developments in Clay Science*, Bergaya, F.; Theng, B. K. G.; Lagaly, G., Eds. Elsevier: **2006**, Vol. 1, 789-864.
187. Newville, M., *Rev. Mineral Geochem.* **2014**, *78* (1), 33-74.
188. Orear, J.; Fermi, E., *Nuclear Physics: A Course Given by Enrico Fermi at the University of Chicago*. University of Chicago Press: **1950**.
189. Penner-Hahn, J. E., X-ray Absorption Spectroscopy. In *eLS*, John Wiley & Sons, Ltd: **2001**.
190. Hahn, J. E.; Scott, R. A.; Hodgson, K. O.; Doniach, S.; Desjardins, S. R.; Solomon, E. I., *Chem. Phys. Lett.* **1982**, *88* (6), 595-598.
191. Frank de, G.; György, V.; Pieter, G., *J. Phys.: Condens. Matter* **2009**, *21* (10), 104207.
192. Fernández-García, M., *Catal. Rev.* **2002**, *44* (1), 59-121.
193. Vankó, G.; Glatzel, P.; Pham, V.-T.; Abela, R.; Grolimund, D.; Borca, C. N.; Johnson, S. L.; Milne, C. J.; Bressler, C., *Angew. Chem. Int. Ed.* **2010**, *49* (34), 5910-5912.
194. Hayes, T. M.; Boyce, J. B., Extended X-Ray Absorption Fine Structure Spectroscopy. In *Solid State Physics*, Ehrenreich,

H.; Seitz, F.; Turnbull, D., Eds. Academic Press: **1983**, Vol. 37, 173-351.
195. Koningsberger, D. C.; Prins, R., *X-Ray Absorption: Principles, Applications, Techniques of EXAFS, SEXAFS and XANES*. Wiley: **1988**.
196. Koch, E. E., *Handbook on Synchrotron Radiation: Vol. 1B*. North-Holland: **1983**.
197. Yano, J.; Yachandra, V. K., *Photosynth. Res.* **2009**, *102* (2-3), 241-254.
198. Simonelli, L.; Marini, C.; Olszewski, W.; Ávila Pérez, M.; Ramanan, N.; Guilera, G.; Cuartero, V.; Klementiev, K.; Saini, N. L., *Cogent Physics* **2016**, *3* (1), 1231987.
199. Guilera, G.; Rey, F.; Hernández-Fenollosa, J.; Cortés-Vergaz, J. J., *J. Phys. Conf. Ser.* **2013**, *430*, 012057.
200. Ravel, B.; Newville, M., *J Synchrotron Radiat* **2005**, *12* (Pt 4), 537-541.
201. Fornasini, P.; Monti, F.; Sanson, A., *J. Synchrotron Radiat.* **2001**, *8* (6), 1214-1220.
202. Dalba, G.; Fornasini, P., *J. Synchrotron Radiat.* **1997**, *4* (Pt 4), 243-255.
203. Price, S. W. T.; Zonias, N.; Skylaris, C.-K.; Hyde, T. I.; Ravel, B.; Russell, A. E., *Phys. Rev. B* **2012**, *85* (7), 075439.
204. Chen, X.; Huo, X.; Liu, J.; Wang, Y.; Werth, C. J.; Strathmann, T. J., *Chem. Eng. J.* **2017**, *313*, 745-752.
205. Lu, C.; Wang, M.; Feng, Z.; Qi, Y.; Feng, F.; Ma, L.; Zhang, Q.; Li, X., *Catal. Sci. Technol.* **2017**, *7* (7), 1581-1589.
206. Soares, O. S. G. P.; Freitas, C. M. A. S.; Fonseca, A. M.; Órfão, J. J. M.; Pereira, M. F. R.; Neves, I. C., *Chem. Eng. J.* **2016**, *291*, 199-205.
207. Kalmykov, P. A.; Klyuev, M. V., *Petrol. Chem.* **2016**, *56* (1), 27-32.
208. Gaspar, A. B.; Dieguez, L. C., *Appl. Catal., A* **2000**, *201* (2), 241-251.
209. Khudorozhkov, A. K.; Chetyrin, I. A.; Bukhtiyarov, A. V.; Prosvirin, I. P.; Bukhtiyarov, V. I., *Top. Catal.* **2017**, *60* (1-2), 190-197.
210. Vedyagin, A. A.; Volodin, A. M.; Kenzhin, R. M.; Stoyanovskii, V. O.; Rogov, V. A.; Medvedev, D. A.;

Mishakov, I. V., *J. Therm. Anal. Calorim.* **2017**, *130* (3), 1865-1874.
211. Di Natale, F.; Orefice, M.; La Motta, F.; Erto, A.; Lancia, A., *Sep. Purif. Technol.* **2017**, *174*, 183-193.
212. Moulijn, J. A.; van Diepen, A. E.; Kapteijn, F., *Appl. Catal., A* **2001**, *212* (1-2), 3-16.
213. Corma, A.; Garcia, H., *Chem. Soc. Rev.* **2008**, *37* (9), 2096-2126.
214. Agostini, G.; Lamberti, C.; Pellegrini, R.; Leofanti, G.; Giannici, F.; Longo, A.; Groppo, E., *ACS Catal.* **2013**, *4* (1), 187-194.
215. Cho, S. J.; Kang, S. K., *J. Phys. Chem. B* **2000**, *104* (34), 8124-8128.
216. Harada, M.; Inada, Y., *Langmuir* **2009**, *25* (11), 6049-6061.
217. Singh, J.; Lamberti, C.; van Bokhoven, J. A., *Chem. Soc. Rev.* **2010**, *39* (12), 4754-4766.
218. Agostini, G.; Pellegrini, R.; Leofanti, G.; Bertinetti, L.; Bertarione, S.; Groppo, E.; Zecchina, A.; Lamberti, C., *J. Phys. Chem. C* **2009**, *113* (24), 10485-10492.
219. Frenkel, A. I., *J Synchrotron Radiat* **1999**, *6* (Pt 3), 293-295.
220. Thommes, M.; Kaneko, K.; Neimark, A. V.; Olivier, J. P.; Rodriguez-Reinoso, F.; Rouquerol, J.; Sing, K. S. W., *Pure Appl. Chem.* **2015**, *87* (9-10).
221. Agostini, G.; Groppo, E.; Piovano, A.; Pellegrini, R.; Leofanti, G.; Lamberti, C., *Langmuir* **2010**, *26* (13), 11204-11211.
222. Groppo, E.; Agostini, G.; Borfecchia, E.; Wei, L.; Giannici, F.; Portale, G.; Longo, A.; Lamberti, C., *J. Phys. Chem. C* **2014**, *118* (16), 8406-8415.
223. Giordanino, F.; Borfecchia, E.; Lomachenko, K. A.; Lazzarini, A.; Agostini, G.; Gallo, E.; Soldatov, A. V.; Beato, P.; Bordiga, S.; Lamberti, C., *J. Phys. Chem. Lett.* **2014**, *5* (9), 1552-1559.
224. Groppo, E.; Agostini, G.; Piovano, A.; Muddada, N. B.; Leofanti, G.; Pellegrini, R.; Portale, G.; Longo, A.; Lamberti, C., *J. Catal.* **2012**, *287*, 44-54.

225. Hong, J.; Marceau, E.; Khodakov, A. Y.; Gaberová, L.; Griboval-Constant, A.; Girardon, J.-S.; Fontaine, C. L.; Briois, V., *ACS Catal.* **2015**, *5* (2), 1273-1282.
226. Lomachenko, K. A.; Borfecchia, E.; Negri, C.; Berlier, G.; Lamberti, C.; Beato, P.; Falsig, H.; Bordiga, S., *J. Am. Chem. Soc.* **2016**, *138* (37), 12025-12028.
227. Paolucci, C.; Parekh, A. A.; Khurana, I.; Di Iorio, J. R.; Li, H.; Albarracin Caballero, J. D.; Shih, A. J.; Anggara, T.; Delgass, W. N.; Miller, J. T.; Ribeiro, F. H.; Gounder, R.; Schneider, W. F., *J. Am. Chem. Soc.* **2016**, *138* (18), 6028-6048.
228. Lin, C.-M.; Hung, T.-L.; Huang, Y.-H.; Wu, K.-T.; Tang, M.-T.; Lee, C.-H.; Chen, C. T.; Chen, Y. Y., *Phys. Rev. B* **2007**, *75* (12), 125426.
229. Kim, S.-J.; Lemaux, S.; Demazeau, G.; Kim, J.-Y.; Choy, J.-H., *J. Mater. Chem.* **2002**, *12* (4), 995-1000.
230. Shen, W.-J.; Ichihashi, Y.; Ando, H.; Okumura, M.; Haruta, M.; Matsumura, Y., *Appl. Catal., A* **2001**, *217* (1-2), 165-172.
231. Bugaev, A. L.; Guda, A. A.; Lazzarini, A.; Lomachenko, K. A.; Groppo, E.; Pellegrini, R.; Piovano, A.; Emerich, H.; Soldatov, A. V.; Bugaev, L. A.; Dmitriev, V. P.; van Bokhoven, J. A.; Lamberti, C., *Catal. Today* **2017**, *283*, 119-126.
232. Srabionyan, V. V.; Bugaev, A. L.; Pryadchenko, V. V.; Avakyan, L. A.; van Bokhoven, J. A.; Bugaev, L. A., *J. Phys. Chem. Solids* **2014**, *75* (4), 470-476.
233. Góralski, J.; Szczepaniak, B.; Grams, J.; Maniukiewicz, W.; Paryjczak, T., *Pol. J. Chem. Technol.* **2007**, *9* (3), 77-80.
234. Giraudon, J. M.; Elhachimi, A.; Leclercq, G., *Appl. Catal., B* **2008**, *84* (1-2), 251-261.
235. Lin, Q.; Ji, Y.; Jiang, Z.-D.; Xiao, W.-D., *Ind. Eng. Chem. Res.* **2007**, *46* (24), 7950-7954.
236. Agostini, G.; Groppo, E.; Bordiga, S.; Zecchina, A.; Prestipino, C.; D'Acapito, F.; van Kimmenade, E.; Thüne, P. C.; Niemantsverdriet, J. W.; Lamberti, C., *J. Phys. Chem. C* **2007**, *111* (44), 16437-16444.
237. Moliner, M.; Corma, A., General Aspects on Structure and Reactivity of Framework and Extra-framework Metals in Zeolite Materials. **2018**.

238. Cerrillo, J. L.; Palomares, A. E.; Rey, F.; Valencia, S.; Palou, L.; Pérez-Gago, M. B., *Microporous Mesoporous Mater.* **2017**, *254*, 69-76.
239. Pavlovskaya, G. E.; Horton-Garcia, C. F.; Dybowski, C.; Corbin, D. R.; Meersmann, T., *J. Phys. Chem. B* **2004**, *108* (5), 1584-1589.
240. Sun, T.; Seff, K., *Chem. Rev.* **1994**, *94* (4), 857-870.
241. Baldansuren, A.; Eichel, R.-A.; Roduner, E., *Phys. Chem. Chem. Phys.* **2009**, *11* (31), 6664-6675.
242. Fenwick, O.; Coutino-Gonzalez, E.; Grandjean, D.; Baekelant, W.; Richard, F.; Bonacchi, S.; De Vos, D.; Lievens, P.; Roeffaers, M.; Hofkens, J.; Samori, P., *Nat. Mater.* **2016**, *15* (9), 1017-1022.
243. Coutino-Gonzalez, E.; Baekelant, W.; Grandjean, D.; Roeffaers, M. B. J.; Fron, E.; Aghakhani, M. S.; Bovet, N.; Van der Auweraer, M.; Lievens, P.; Vosch, T.; Sels, B.; Hofkens, J., *J. Mater. Chem. C* **2015**, *3* (45), 11857-11867.
244. Miyanaga, T.; Suzuki, Y.; Matsumoto, N.; Narita, S.; Ainai, T.; Hoshino, H., *Microporous Mesoporous Mater.* **2013**, *168*, 213-220.
245. Nakamura, A.; Narita, M.; Narita, S.; Suzuki, Y.; Miyanaga, T., *J. Phys. Conf. Ser.* **2014**, *502*, 012033.
246. Lin, C. C. H.; Danaie, M.; Liu, Y.; Mitlin, D.; Kuznicki, S. M.; Eyring, E. M., *J. Nanosci. Nanotechno.* **2009**, *9* (8), 4985-4987.
247. Golubeva, O. Y.; Ul'yanova, N. Y., *Glass Phys. Chem* **2015**, *41* (5), 537-544.
248. Flores-López, N. S.; Castro-Rosas, J.; Ramírez-Bon, R.; Mendoza-Córdova, A.; Larios-Rodríguez, E.; Flores-Acosta, M., *J. Mol. Struct.* **2012**, *1028*, 110-115.
249. Chen, F.; Liu, Y.; Wasylishen, R. E.; Xu, Z.; Kuznicki, S. M., *J. Nanosci. Nanotechno.* **2012**, *12* (3), 1988-1993.
250. Chmielarz, L.; Jablonska, M., *RSC Adv.* **2015**, *5* (54), 43408-43431.
251. Wang, F.; Ma, J.; He, G.; Chen, M.; Zhang, C.; He, H., *ACS Catal.* **2018**, 2670-2682.
252. Zhang, L.; Zhang, C.; He, H., *J. Catal.* **2009**, *261* (1), 101-109.
253. Kielland, J., *J. Am. Chem. Soc.* **1937**, *59* (9), 1675-1678.

254. Chebbi, M.; Azambre, B.; Cantrel, L.; Koch, A., *J. Phys. Chem. C* **2016**, *120* (33), 18694-18706.
255. Kuroda, Y.; Mori, T.; Sugiyama, H.; Uozumi, Y.; Ikeda, K.; Itadani, A.; Nagao, M., *J. Colloid Interface Sci.* **2009**, *333* (1), 294-299.
256. Yumura, T.; Oda, A.; Torigoe, H.; Itadani, A.; Kuroda, Y.; Wakasugi, T.; Kobayashi, H., *J. Phys. Chem. C* **2014**, *118* (41), 23874-23887.
257. Alonso-Escobar, C. Estudio de materiales zeolíticos como estructuras anfitrionas de nanopartículas: aplicaciones catalíticas y medioambientales. Universitat Politècnica de València, **2017**.
258. Seifert, R.; Rytz, R.; Calzaferri, G., *J. Phys. Chem. A* **2000**, *104* (32), 7473-7483.
259. Jacobs, P. A.; Uytterhoeven, J. B.; Beyer, H. K., *J. Chem. Soc. Farad. T 1* **1979**, *75* (0), 56-64.
260. Kim, S. Y.; Kim, Y.; Seff, K., *J. Phys. Chem. B* **2003**, *107* (29), 6938-6945.
261. Sayah, E.; Brouri, D.; Massiani, P., *Catal. Today* **2013**, *218-219*, 10-17.
262. Link, S.; El-Sayed, M. A., *J. Phys. Chem. B* **1999**, *103* (21), 4212-4217.
263. Gurin, V. S.; Bogdanchikova, N. E.; Petranovskii, V. P., *J. Phys. Chem. B* **2000**, *104* (51), 12105-12110.
264. Ogden, J. S.; Bogdanchikova, N. E.; Corker, J. M.; Petranovskii, V. P., *Eur. Phys. J. D* **1999**, *9* (1), 605-608.
265. Fiddy, S. G.; Bogdanchikova, N. E.; Petranovskii, V. P.; Ogden, J. S.; Avalos-Borja, M., EXAFS and optical spectroscopy characterisation of silver within zeolite matrices. In *Stud. Surf. Sci. Catal.*, Aiello, R.; Giordano, G.; Testa, F., Eds. Elsevier: **2002**, Vol. 142, 1939-1946.
266. Michalik, J.; Sadło, J.; Yu, J.-S.; Kevan, L., *Colloid Surface A* **1996**, *115*, 239-247.
267. Sadlo, J.; Danilczuk, M.; Michalik, J., *Phys. Chem. Chem. Phys.* **2001**, *3* (9), 1717-1720.
268. Xu, B.; Kevan, L., *J. Phys. Chem.* **1991**, *95* (3), 1147-1151.

269. Mastikhin, V. M.; Goncharova, S. N.; Tapilin, V. M.; Terskikh, V. V.; Balzhinimaev, B. S., *J. Mol. Catal. A: Chem.* **1995**, *96* (2), 175-179.
270. Liu, L.; Zakharov, D. N.; Arenal, R.; Concepcion, P.; Stach, E. A.; Corma, A., *Nat. Commun.* **2018**, *9* (1), 574.
271. Gang, L.; Anderson, B. G.; van Grondelle, J.; van Santen, R. A., *J. Catal.* **2001**, *199* (1), 107-114.
272. Gang, L.; Anderson, B. G.; van Grondelle, J.; van Santen, R. A.; van Gennip, W. J. H.; Niemantsverdriet, J. W.; Kooyman, P. J.; Knoester, A.; Brongersma, H. H., *J. Catal.* **2002**, *206* (1), 60-70.
273. Gang, L.; Anderson, B. G.; van Grondelle, J.; van Santen, R. A., *Appl. Catal., B* **2003**, *40* (2), 101-110.
274. Zhang, L.; He, H., *J. Catal.* **2009**, *268* (1), 18-25.
275. Yang, M.; Wu, C.; Zhang, C.; He, H., *Catal. Today* **2004**, *90* (3), 263-267.

Chapter 7

General conclusions

The following are the most relevant conclusions derived from the results obtained during this doctoral thesis:

X-ray absorption spectroscopy demonstrated to be an extremely important tool to following the pathways of metal nanoparticles formation and subsequent tuning during activation treatments under different atmospheres.

In chapter 4, it was demonstrated that the thermal stability of the metal precursor dictates the size and speciation of the Pd species during and after the activation process. XAS was able to track different features during the study of Pd nanoparticles formation such as the speciation of PdO_xCl_y, PdO ordering and its transformation to Pd^0 after immediate contact with reductive atmosphere, formation/decomposition of PdH_x and the different metallic sizes discussed in terms of average coordination numbers. Summing up, $PdCl_2$ generates smaller nanoparticles than $Pd(OAc)_2$, which in turn generates smaller nanoparticles than $Pd(NO_3)_2$, regardless of the support used for catalyst preparation.

In chapter 5, silver species in different Ag-containing small-pore zeolites were comprehensively followed by the combination of *in situ* XAS with a set of laboratory techniques. By selecting the reduction temperature, different silver species can be formed which can be partially redispersed as Ag^+ within extraframework positions of the zeolites upon a subsequent treatment under oxidative conditions. It was demonstrated that

bulk silver species present in AgCHA-based samples were harder to be reoxidized while the reoxidation in AgRHO reaches always the same extent.

Interestingly, it was shown that zeolite framework can play an important role on silver clustering, preventing that silver species were fully aggregated to bulk size under the studied conditions. More specifically, RHO zeolite tends to confine Ag_8-type clusters while CHA allows the formation of bulk metallic species, regardless of Si/Al ratio or type of co-cation present in the sample. These results point out to an influence of RHO zeolite structure on formed silver species.

At the same time, the cumulant approach was used to correctly estimate the Ag-Ag bond distances in silver nanoparticles with CN < 8, which were underestimated when only least-squares fittings were taken into account. Moreover, an interesting correlation between CN and R_{Ag-Ag} were shown for both differently reduced AgCHA and AgRHO.

Last but not least, the tuned Ag-based materials were tested as catalysts for SCO-NH_3, showing interesting results for AgCHA-based materials which possess bulk-type of species with high selectivity to N_2 within the range of interest. Conversely, the AgRHO-based materials only showed high NH_3 conversion at high temperatures (~600 ºC) which is close to the conversion obtained without catalyst (i.e. thermal test).

Chapter 8

Other works

During the activities of my PhD I collaborated with other researchers in the collecting and analysis/interpretation of XAS data. A brief description of each project and my respective participation are reported below:

1) Nonoxidative methane dehydroaromatization using Mo/zeolite catalysts (Prof. Jose Manuel Serra and Prof. Agustín Martínez)

Nonoxidative methane dehydroaromatization (MDA: $6CH_4 \leftrightarrow C_6H_6 + 9H_2$) using shape-selective Mo/zeolite catalysts is a key technology for exploitation of stranded natural gas reserves by direct conversion into transportable liquids. One of main problems about this process is that catalyst deactivates quickly through kinetically favored formation of coke. In this study, the electronic properties of fresh and spent Mo/ZSM-5 catalyst were investigated by XANES on Mo K-edge. By performing linear combinations of spectra in comparison with the standards the oxidation state of Mo in the samples were characterized. I helped with XANES data analysis and interpretation.

Results published at:

Morejudo et al.; Science, 353 (2016) 563-566.

2) Structural information of isolated copper species stabilized in chabazite like zeolites. Stability and evolution under DeNO$_x$ reaction conditions (Prof. Avelino Corma)

Selective catalytic reduction (SCR) of NO_x with ammonia is an important technology that enables the reduction of environmentally harmful NO_x in the exhaust gases of vehicles, ships, and power plants to the low emission levels required by legislation in many places. Metal substituted zeolites, in particular with Cu and Fe, are well known catalysts for SCR of NO_x with NH_3 and are currently used in automotive applications. In the automotive sector, besides high activity and selectivity, high hydrothermal stability is an important issue. In this sense, Cu-zeolite structures containing small pores, such the CHA or AEI topologies, have shown a high hydrothermal stability being recently commercialized on diesel vehicles. The enhanced stability of Cu-chabazite materials is rationalized in terms of the unique small-pore structure of this zeolite. On the other hand, fundamental knowledge about the nature of the catalytically active site is still under discussion, being an important issue in the design of new efficient catalytic materials. The aim of this project was to obtain structural information of the copper environment in distinct Cu-zeotype systems (Cu-SAPO-34, Cu-SSZ-13, Cu-SAPO-18) in order to determine the coordination degree and clustering degree of the copper ions and their bonding environment as isolated or Cu-Cu aggregates at

different reaction conditions. In this project I participated in the data collection and treatment of whole data set, performing mainly linear combinations analysis to determine the fraction of Cu^{+}/Cu^{2+} present during reaction conditions.

3) Analysis of the active site on CuZnGa catalysts with enhanced catalytic performance in the low temperature Methanol Steam Reforming (Dra. Patricia Concepción)

Methanol, as a H_2 storage material, has significant advantage in terms of energy density over other means of H_2 storage such as hydrides and compressed or liquefied hydrogen, and therefore is an attractive source of H_2 for fuel cell powered portable devices. In order to avoid poisoning of the Pt anode of the PEM fuel cell, CO formation in the MSR process must be strongly minimized. While the low temperature MSR (LT-MSR) is an attractive source of nearly CO-free H_2, the design of the catalyst is crucial in order to achieve large amounts of H_2 at low temperature with low CO formation. Cu-based catalysts have been commercially produced and successfully used in industry for many years, however, they are quite sensitive to the process conditions. Therefore, in the last years many efforts have been devoted to the development of more efficient Cu-MSR catalysts as alternative to the conventional CuZnAl systems. In this sense CuZnGa systems has been shown as promising alternatives to the MSR catalysts. In this project, highly active and selective $Cu/ZnO/Ga_2O_3$ catalytic systems for LT-MSR were developed,

whose promising results, particularly at very low temperatures (180-200 °C). The properties of all the $Cu/ZnO/Ga_2O_3$ catalysts are similar to industrial catalytic formulations (high Cu loading, 5-20 nm Cu particle sizes and exposed Cu surface areas of 10 m^2/g or greater). MSR activity results obtained in the laboratory have shown remarkable differences in the activity and selectivity of the various CuZnGa catalysts tested. The conventional physicochemical characterization techniques did not provide satisfactory experimental evidence for explaining the huge differences in the performance of the distinct CuZnGa samples. The local environment and electronic properties of the metallic catalysts were investigated in this project measuring XAS in the respective Cu, Zn and Ga K-edges during catalysts activation step and under MSR reactions conditions. My role in this project was to participate in the data collection and data analysis. In one of the studied samples was possible to observe the formation of a Ga-containing wurtzite (possibly Ga substituting ZnO framework), while the Cu and Zn were present as Cu metal nanoparticles and ZnO, respectively, during the whole activation and catalytic processes. Conversely, the Ga local environment for the second sample seems to be composed by different phases, while the Cu and Zn are present as Cu and ZnO as well.

4) *In situ* characterization of Co-Ru/TiO_2 catalysts by X-ray Absorption Spectroscopy during activation conditions (Prof. Agustín Martínez)

The Fischer-Tropsch synthesis (FTS) is a well-established process that produces high-quality fuels from carbon sources alternative to oil via syngas (mixture of CO and H_2). Cobalt supported on SiO_2, Al_2O_3, or TiO_2 are preferred catalyst for this process. Usually, small amounts of noble metals (Ru, for example) as promoters are used in catalyst formulation aiming to improve the reduction degree and/or the density of Co^0 active sites, which result in higher activity and selectivity to C_{5+} products. A synergic effect between Co and Ru in bimetallic Co-Ru nanoparticles or a higher concentration of accessible Co^0 as a consequence of a higher Co reduction degree in presence of Ru have been proposed as the origin of Ru promoting effects. Despite the reported results, the role of Ru on metal-promoted Co-based catalysts remains unclear. To disentangle this issue, XAS measurements on Ru K-edge were performed to investigate samples with variable Ru loading (0.2, 0.7 and 1.2 wt.%) as promoter in cobalt catalysts supported on TiO_2-anatase. It was demonstrated by a corefinement fit of EXAFS data that ruthenium at low concentrations is in the form of a metal alloy with cobalt, with ruthenium being mostly on the surface of the bimetallic nanoparticle. With the increase in the promoter content the segregation of Ru in monometallic

nanoparticles is favored; being the catalysts composed by a mixture of Co-Ru metal alloy and small isolated Ru nanoparticles. In this work I participated in the data collection and whole process of data analysis.

5) Structural evolution of bimetallic PtSn clusters in zeolites (Prof. Avelino Corma)

Propylene is an important bulk chemical with wide application for polymer and raw material for production of other intermediates in chemical industry. In recent years, the production of shale gas has been increasing rapidly and it is becoming highly interesting to production of propylene by direct dehydrogenation of propane since a large amount of propane can be extracted from shale gas. So far, the industrial catalyst for propane dehydrogenation mainly includes two types of catalysts, $PtSn/Al_2O_3$ for Oleflex process and $CrOx/Al_2O_3$ for CATOFIN process. For the bimetallic $PtSn/Al_2O_3$ catalysts, the catalyst will deactivate quickly under the propane dehydrogenation conditions due to the formation of coke. Therefore, a regeneration process (usually by calcination treatment in air at high temperature >600 $^{\circ}$C) is required to recover the activity. However, such regeneration treatment will cause the sintering of Pt, leading to loss of activity. Nevertheless, considering the dehydrogenation of light alkanes is a structure-sensitive reaction, it can be a promising way to obtain highly active catalyst for dehydrogenation of propane by preparing ultra-small

Pt-based particles, especially subnanometric Pt clusters. With this in mind, a series of Pt and PtSn-based catalysts with significant small particle sizes were prepared and the results shown that the presence of Sn (apart from small Pt particle size) improves significantly the catalytic performance. XAS was used in this project to figure out what is the relationship between Pt and Sn atoms in the bimetallic clusters. In this project I participated in both data collection and interpretation of XAS results. After studying the catalysts at both Pt L_{III}-edge and Sn K-edge, the results pointed out to the presence of small metallic Pt clusters and highly dispersed SnO_x species without intimate contact between Pt and Sn.

6) XAS study on As environment in tetraalkylarsonium cations for zeolite synthesis and their derivatives (Prof. Fernando Rey)

Obtaining the distinct zeolitic structures closely depends on the organic structure-directing agent (OSDA) used during the synthesis. Among different classes of OSDA's described in literature, the alkylammonium group is by far the most frequently used. In the last few years our group have rationalized the use of tetraalkylphosphonium cations (PR_4^+) as OSDA, which allow the synthesis of zeolites under more severe conditions compared to those of ammonium-type and enable the synthesis of new zeolites, such as ITQ-27, ITQ-34, ITQ-49, ITQ-53, etc. Unfortunately, the X-ray absorption edges of N or

P atoms appear at very low energies and therefore, their XAS spectra cannot be measured easily. Recently, we succeeded have used in the synthesis of MFI and BEA zeolites using tetrapropylarsonium (Pr_4As^+) and tetraethylarsonium (Et_4As^+), respectively. The presence of atoms heavier than phosphorous, nitrogen and carbon in these OSDAs (As atoms) could help to characterize the species filling in the zeolitic voids, which could be of interest for assessing the relation between the size and shape of the organic used and its location in the obtained material, providing new insights for understanding zeolite crystallization processes. In addition to understanding the use of R_4As^+ as OSDA, different subnanometric metallic arsenides or arsenites (e.g. GaAs, $GaAsO_4$, etc) could be formed inside zeolite cavities and channels through elimination of OSDA by calcination/reduction treatments in a gallium-containing zeolite. In this case, we expect that gallium atoms migrate from outside zeolite framework through calcination and interact with arsenic atoms provided by OSDA burnt. Therefore, studying by XAS the As local environment in AsR_4^+ cations, as well as entrapped in zeolite voids and their evolution under thermal treatment under oxidative atmosphere was proposed. Also, the changes of Ga local environment in these zeolites upon thermal treatment were studied. In this project I participated in the XAS data collection and analysis of whole data set.